

THESIS

MICHIGAN STATE UNIVERSITY LIBRARIES
3 1293 01399 2155

This is to certify that the

thesis entitled

HIGH RESOLUTION ELECTRON MICROSCOPY EXAMINATION OF DISLOCATION CORE STRUCTURES IN B2 Fe-A1 ALLOYS

presented by

Doug Sharrott

has been accepted towards fulfillment of the requirements for

Masters degree in Materials Science

Major professor

Date 17/21/94

**O**-7639

MSU is an Affirmative Action/Equal Opportunity Institution

# LIBRARY Michigan State University

PLACE IN RETURN BOX to remove this checkout from your record.
TO AVOID FINES return on or before date due.

DATE DUE	DATE DUE	DATE DUE

MSU Is An Affirmative Action/Equal Opportunity Institution chairclasses.pm3-p.

# HIGH RESOLUTION ELECTRON MICROSCOPY EXAMINATION OF DISLOCATION CORE STRUCTURES IN B2 Fe-Al ALLOYS

Ву

**Doug Sharrott** 

### **A THESIS**

Submitted to

Michigan State University

in partial fulfillment of the requirements

for the degree of:

#### **MASTER OF SCIENCE**

Department of Material Science and Mechanics

1995

#### **ABSTRACT**

# HIGH RESOLUTION ELECTRON MICROSCOPY EXAMINATION OF DISLOCATION CORE STRUCTURES IN B2 Fe-AI ALLOYS

By

#### Doug Sharrott

Stoichiometric Fe-50at%Al and iron rich Fe-40at%Al B2 ordered intermetallic single crystals (oriented near [001]) have been deformed in compression to approximately 5% plastic strain at 873K. Optical slip trace and conventional phase contrast electron microscopy has been used to characterize slip and the dislocation structure in these materials. The observed dislocations (for both alloys) were predominantly <100>(001) prismatic edge dislocations. Very limited observations of <111> screw dislocations were observed in Fe-50Al as well. Following substructural characterization, high resolution electron microscopy (HREM) was used to image core structures of the dislocations observed. HREM studies revealed predominately <100>{001} dislocation cores. Surprisingly, a <110> core was observed as well. Fe-40Al edge dislocation cores were found to be compact with little or no evidence of

dislocation str

spreading.

found in Fe-

Comparison

modeled and

properties of

their core stru

and CoAl as v

spreading. A number of differently arranged <100>(001) edge dislocation cores were found in Fe-50Al. These structures contained varying elements of glide and climb. Comparison with theoretical structures revealed significant differences between the modeled and experimentally observed structures. Differences in the mechanical properties of the two FeAl alloys are discussed with respect to the differences observed in their core structures. These core structures are compared to similar cores found in NiAl and CoAl as well. The effect of thermal history on the mechanical properties and dislocation structure of FeAl is also discussed.

### **DEDICATION**

To my Mom and Dad
for being the best parents
anyone could hope to have!

George contract

people:

single cr

State Un

(director

use of th

help of h

Martin A

parents f

following

Jason Pa

Wilson, !

and Ziew

#### **ACKNOWLEDGMENTS**

I would like to acknowledge and thank the office of Naval Research and Dr. George Yoder (scientific officer) for the funding and support of this project under contract number N00014-90-J-1910. I would also like to thank the following groups of people: Dr. R. Neobe of NASA LRC and Dr. S. Hartfield for providing the Fe-40Al single crystals; Mr. C. Vailhe and Dr. D. Farkas of Virginia Polytechnic Institute and State University for providing the results of their EAM calculations; Dr. John Mansfield (director of the University of Michigan Electron Microbeam Analysis Laboratory) for the use of the JOEL 4000EX; Dr. Dave Grummon for the use of his lab equipment and the help of his assistants; Yu Zhang and Scott Tonn for their invaluable assistance; Dr. Martin A. Crimp for his guidance, assistance and tolerance and last but not least, my parents for their moral and financial support. In addition I would like to thank the following people for technical assistance and/or just being good people; Randy Beals, Jason Paluczyk, Jinkyu Choi, Dr. Dave Mace, Dr. John Martilla, Julian Ambriz, Brett Wilson, Michael Wood, Alan Gibson, Pat Sneary, Ojars, Nam, Chris Showerman, Vish and Ziewei.

List of Ta

List of Fi

Introduct

1.1 Ba

1.2 B2

1.3 Di

1.

1.

1.

1 1

1.5 \

1.6 (

2. E<sub>X</sub>p

2.1 1

2.2

2.3

2.4

2.5

2.6

2.7

2.8

3. E<sub>X</sub>

3.1

3.2

# Table of Contents

<u>Page</u>
List of Tables
List of Figures
Introduction
1.1 Background
1.2 B2 vs. bcc Dislocation Behavior
1.3 Dislocation Behavior of B2 Aluminides With Respect to Temperature
1.4 Properties of B2 FeAl
1.4.1 Effects of Temperature, Test Environment and Alloying Additons
1.4.2 Mechanical Properties With Respect to Stiochiometry and Thermal History
1.4.3 Thermal History and Vacancy Concentration Effects
1.4.4 Combined Effects of Thermal History and Testing Environment
1.5 Vacancy Behavior in B2 FeAl
1.6 Objective
2. Experimental Procedure
2.1 Material
2.2 Compression Sample Preparation
2.3 Heat Treatment
2.4 Crystallographic Orientation.
2.5 Sample Compression
2.6 Slip Trace Analysis
2.7 Thin Foil Preparation.
2.8 Transmission and High Resolution Electron Microscopy
3. Experimental Results
3.1 Slip Characterization
3.2 Burgers Vector Determination

.

. 1

4

4.6

5. Co

Apper

3.3 High Resolution Electron Microscopy	66
3.3.1 Fe-40Al	66
3.3.2 Fe-50Al	68
4. Discussion	74
4.1 Rationalization of Slip Trace and Diffraction Contrast Analyses	74
4.2 <110> Core Observed in Fe-40Al	74
4.3 Dissociated Core in Fe-50Al	77
4.4 An Apparent Dipole in Fe-50Al	<b>7</b> 9
4.5 Comparison of A Model Core With Observed Cores	79
4.5.1Dislocation Observations and Cooling Rate Effects	83
4.5.2 Other Factors Which May Affect Core Structure	86
4.6 Comparison Between Fe-40Al and Fe-50Al Cores	87
5. Conclusions	91
Appendix	93

## <u>Table</u>

- 1. Elast empi
- 2. Value 48.8.5
- 3. Displ.
- 4. Effect Prope
- 5. Mech tempe
- 6. Chem

## List of Tables

Table		Page
1.	Elastic (room temperature) constants of B2 Fe-50Al as determined empirically and experimentally	7
2.	Values for the Critical Resolved Shear Stress of Fe-39.2Al and Fe-48.8Al as a function of cooling rate following heat treatment	10
3.	Display of the possible dislocation configurations in B2 FeAl	. 19
4.	Effect of testing environment on the Room Temperature Tensile Properties of Fe-40Al with and without boron	. 32
5.	Mechanical Properties of Fe-36Al after various annealing temperatures and times	40
6.	Chemical compositions of the materials used in this study	. 49

<u>Figure</u>

1.

2.

3.

4.

5.

6.

7.

8.

9.

10.

11.

12.

13.

14.

15.

16.

S ((

(á (È

17.

# List of Figures

<u>Figure</u>		<u>Page</u>
1.	B2 unit cell with directions <100>, <110> and (closed packed direction <111> labeled	
2.	FeAl phase diagram, illustrating crystal structure as a function of temperature and composition	. 4
3.	Thermal conductivities of B2 FeAl, NiAl, CoAl, common nickel based superalloys and other common alloys	
4.	Vacancy concentration vs. at% Al for FeAl	. 9
5.	Stress-Strain curves for extruded polycrystalline Fe-40Al which has been quenched at different rates	. 11
6.	Plot of B2 FeAl, NiAl, CoAl, several common alloys and alumina	. 12
7.	Approximate creep strengths of several intermetallics in comparison to superalloys, iron and nickel	. 14
8.	(a) and (b) Computer models of two possible <111> screw dislocation cores predicted for bcc metals. (c) orientations of relaxation planes for the cores	. 16
9.	B2 superdislocation schematic displaying two partials separated by an APB.	. 18
10.	Experimental image of cross slip from {110} to {112} for Fe-47.2Al deformed near the [011]-[111] border at 673K	. 21
11.	Change in slip direction for polycrystalline and single crystal B2 FeAl as a function of at% Al vs. temperature	. 23
12.	Atomic percent Al vs. slip transition temperature for FeAl single	
	crystals oriented near the [111] portion of the unit triangle	. 24
13.	Slip transition temperature dependence on orientation for Fe-49.2Al	. 26
14.	Slip transition orientation and temperature dependence for Fe-47.2Al	. 27
15.	Indication that the <111>-<100> slip transition occurs somewhere around 773K-873K for an Fe-49.2Al alloy	. 28
16.	Slip lines corresponding to (a) [001](110) (b) [010](001) and (c) [010] (001) in combination with [001](110) slip	29
17.	(a) Yield strength vs. temperature for directionally solidified Fe-40Al (b) Percent elongation vs. temperature for the same alloy	31

Figure

18. Perc

Perce addit 19.

20. Hard

21. Stres

Pero test 22.

23. Yie

24. Ha

25. Str po!

26. Re

co 27. St

28.

D

Cr tr (a s)

II

Z

**2**9. O fa (a (t

30.

31.

32.

33.

Co an an Co

n

<u>Figure</u>	<u>Page</u>
18.	Percent elongation of Fe-35Al in oxygen and Fe-33Al in argon
19.	Percent elongation vs. temperature for FeAl and FeAl with ternary additions of C, Zr, Hf and B
20.	Hardness vs. at% Al isotherns for FeAl at (a) 25°C (b) 500°C
21.	Stress vs. strain for polycrystalline Fe-40Al subjected to different cooling rates, with and without the addition of 0.2 wt% boron
22.	Percent elongation vs. annealing temperature for Fe-36Al samples tested in oxygen and air
23.	Yield strength vs. annealing temperature for polycrystalline Fe-36Al
24.	Hardness vs. annealing temperature for polycrystalline Fe-36Al
25.	Strain hardening coefficient vs. annealing temperature for polycrystalline Fe-36Al
26.	Rectangular compression specimen showing the orientation convention used throughout the analyses
27.	Standard stereographic triangles showing single crystal compression axes for (a) Fe-40Al and (b) Fe-50Al
28.	Disk thinning Jig used to prepare TEM and HREM foils
29.	Optical micrographs showing {110} slip plane traces on two faces of an Fe-40Al single crystal deformed at 873K.  (a) Slip lines on the front face of the specimen.  (b) Slip lines on the right face of the same specimen.
30.	Optical micrographs showing duplex {110} and {111} slip plane traces on two faces of an Fe-50Al single crystal deformed at 873K.  (a) Duplex slip lines on the left face of an Fe-50Al compression specimen.  (b) Slip lines on the front face of the same specimen
31.	Illustration of a standard two face slip trace analyses
32.	Zone map illustrating the g-vectors used in the $\mathbf{g} \cdot \mathbf{b} = 0$ analysis of an Fe-40Al compression sample
33.	Conventional diffraction contrast images illustrating a Burgers vector analysis in deformed Fe-40Al. The dislocation labeled (a) has b=[001] and line directions of [100] and [010]. Thereby, indicating a prismatic configuration for the dislocation. Figures (a), (c) and (d) were taken
	near the (011) zone, while (b) and (e) were taken near (001)

35. (a) F core imaginates (d)

36. Exp in I im: par

37. HF Cl are the

38. H

39.

H co

**4**0.

41.

42.

43.

44,

. E fi

Figure	<u>Page</u>	
34.	Conventional TEM images of the deformation structure of Fe-50Al deformed at 873K. the substructure is dominated by <100> dislocations. The long straight dislocation is a <111> dislocation. Fig. (a) was taken near the (010) zone, figs. (b) and (c) were taken near (111) and fig. (d) was taken near (001)	65
35.	(a) Experimental HREM image of a b = [001](100) edge dislocation core found in Fe-40Al. (b-e) Digitally scanned and compressed images of (a) representing views down the (b) [202] (c) [200] (d) [202] and (e) [002] directions	67
36.	Experimental HREM images of a climb dissociated dislocation core in Fe-40Al with a $b_e = [101]$ edge component. (a) The core as initially imaged (b). The same core following beam induced dissociation of the partials.	69
37.	HREM image of a compact [001](100) dislocation core in Fe-50Al. Close examination of the {220} extra half planes reveals that they are climb dissociated perpendicular to the plane containing the burgers vector.	70
38.	HREM image of a dissociated [001](100) dislocation core in Fe-50Al. The burgers circuits around the partials, implying that positive climb might have been involved	72
39.	HREM image of two <001> edge dislocations in an apparent dipole configuration in Fe-50Al. The two dislocations lie approximately 10 atomic positions apart in the [200] direction	73
40.	Schematic representations of possible glide and climb mechanisms which could result in 1/2<111> partials being separated along a {100} plane. The dashed lines represent an APB ribbon and the arrows denote the direction of the dislocation's motion. Note, only the glide dissociation or negative climb dissociation could result in a configuration consistent with figure 38	78
41.	<ul> <li>(a) Schematic cross section of a vacancy-formed prismatic dipole.</li> <li>(b) Schematic cross section of an interstitial dipole.</li> <li>Note the sense of the burgers vector of the vacancy formed dipole is consistent with the image observed in figure 39.</li> </ul>	80
42.	(a) Atom positions for a <001>{100} edge dislocation as determined by EAM. (b)-(g) Simulated HREM images based on the atom positions shown in (a)	81
43.	Scheme for the formation of dislocation helix pairs	84
44.	Experimental HREM image of a $\mathbf{b} = [010]$ edge dislocation core found in Ni-50Al. Note the greater planar distortions parallel and perpendicular to the burgers vector.	88

Figure

45. Ex fou arc

45. Experimental HREM image of a b = [010] edge dislocation core found in Co-50Al. Again, note the greater planar distortions around the core, compared to Fe-50Al.	89

propertion
moderate
advantage
remaining
density;
However,
physical a
overcome
The main
using convenience

will be discomentioned mechanical be expanded stoichiomet

(FeAl only

 $A_{S}$ 

concentration

on the review

Inter

between the intermetallic

#### 1. Introduction

B2 intermetallic aluminides, such as FeAI, NiAI and CoAI, possess many properties which make them potentially competitive with ceramics and superalloys in moderate to high temperature structural applications. These materials have several advantages including: maintaining crystal order over a wide composition range; remaining ordered up to their melting points; having excellent oxidation resistance; low density; high strength and consist of low cost; composed of readily available materials. However, due to the structure of B2 FeAI (directional bonding and thermally influenced physical and mechanical properties) this alloy poses several barriers which must be overcome in order to make it competitive with currently used high temperature materials. The main disadvantages include: generally poor ductility at low temperatures (when using conventional fabrication processes); low toughness at ambient temperatures; highly anisotropic moduli; high vacancy concentrations; high thermal expansion coefficient (FeAI only) and low creep strength (FeAI only).

As an introduction to this investigation, the basic information concerning FeAl will be discussed and compared with the B2 alloys NiAl and CoAl. The previously mentioned advantages and disadvantages will be covered. Then, a review of the mechanical behavior of bcc materials will be presented. Following this, the review will be expanded to include the B2 structure. In addition, influences of temperature, stoichiometry, orientation (single crystals), thermal history (annealing/vacancy concentration) and testing environment will be discussed with respect to the mechanical properties of B2 FeAl. Finally, the objectives of this work will be elaborated on, based on the review and current work on B2 materials.

Intermetallic B2 aluminides consist of an ordered lattice that has strong bonding between the constituent atoms. The B2 (CsCl) structure is the simplest of the intermetallic structures, consisting of two interpenetrating simple cubic cells (see

figure (Fe-34

alloyin

melting tempera

themsel engines for Fe-5 centrifus 40% to 5 in weigh it is know alloys (see blades carefficiency favorable performa.

has the ad materials.

and high

calculation

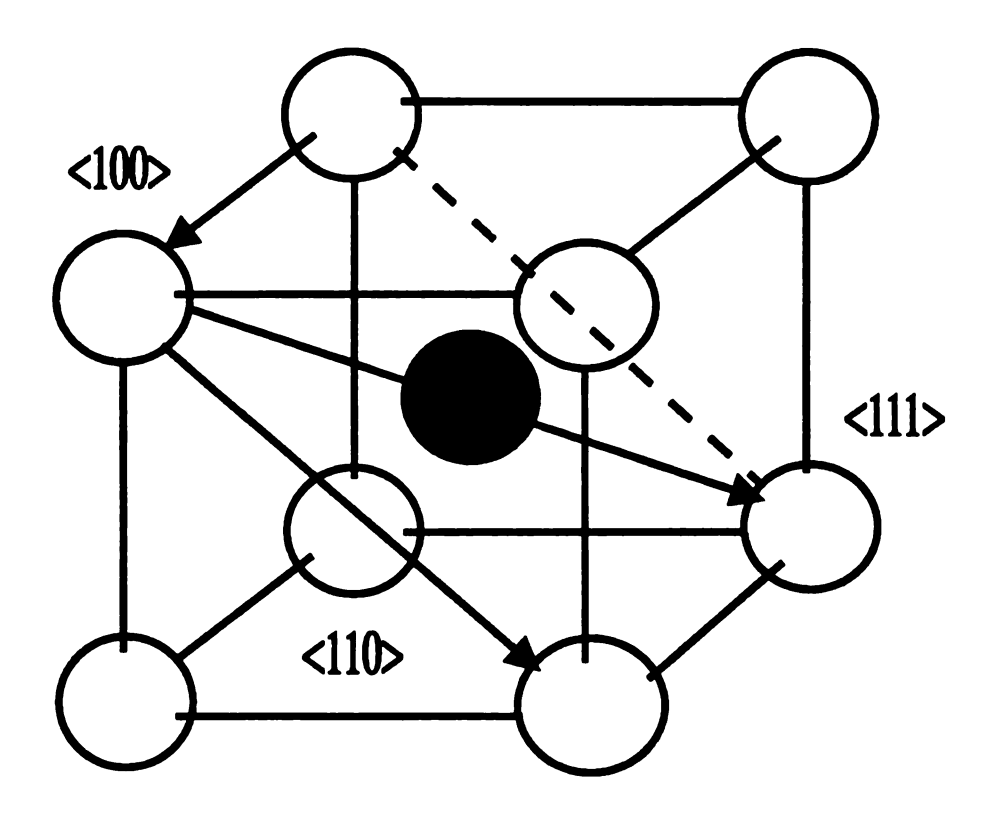
Experimen

figure 1). An advantage of B2 FeAl is that it can exist over a wide range of composition (Fe-34 to 51 at% Al). This implies large solubilities for third element substitutional alloying additions [1]. Figure 2 displays the binary phase diagram for FeAl [2].

In addition, the B2 aluminides, CoAl, NiAl and FeAl remain ordered up to their melting points (~ 1900K for NiAl and CoAl and 1500K for FeAl). Current service temperatures for superalloys top out at around 1300K [3].

Excellent oxidation resistance is expected, due to the large amount of aluminum contained in these alloys. In fact, protective "aluminide" coatings have already proven themselves on a large number of high pressure turbine blades and vanes of aircraft engines [4]. Another advantage is the fact that these alloys are 1/3 less dense (5.59 g/cm<sup>3</sup>) for Fe-50Al) than their nickel based superalloy counterparts (6-7 g/cm<sup>3</sup>). When centrifugal forces are taken into consideration, a potential weight savings on the order of 40% to 50% would be seen for a jet aircraft. The savings would be due to the reduction in weight of the jet engine components and the external engine housing [5]. Additionally, it is known that B2 NiAl possesses higher thermal conductivity than nickel based super alloys (see figure 3). Due to the higher thermal conductivity of B2 NiAl, jet engine blades can reduce their hot spot temperature by as much as 50K [4]. This implies greater efficiency, due to the ability to operate engines at higher temperatures. All of these favorable properties combine to create a potential for a longer lasting, higher performance, lighter (higher thrust to weight ratio) jet engines for future military aircraft and high speed civil transports. Additionally, the large aluminum content of these alloys has the added advantage of creating a high strength alloy with readily available low cost materials. The theoretical room temperature moduli (determined by first principles calculations) for FeAl, NiAl and CoAl are 347GPa, 247GPa and 296GPa respectively [6]. Experimental values determined by the piezoelectric ultrasonic composite oscillator

B2 unit o



CsCl (B2) Structure (FeAl, NiAl, CoAl)

Possible Slip Vectors: <100>, <110>, <111>

Figure 1

B2 unit cell with directions <100>,<110> and (closed packed direction) <111> labeled.

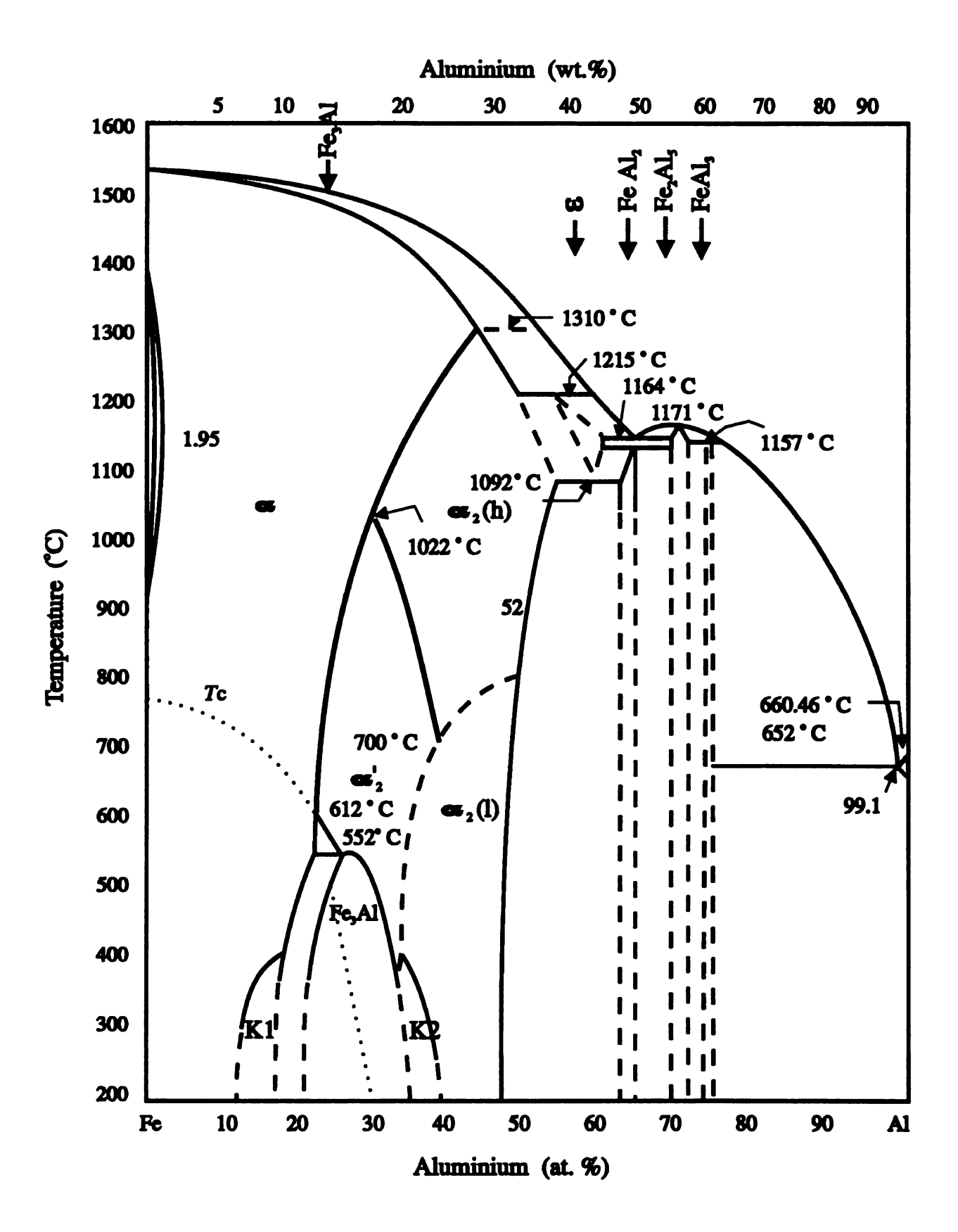


Figure 2
FeAl phase diagram, illustrating crystal structure as a function of temperature and composition. Adapted from [2].

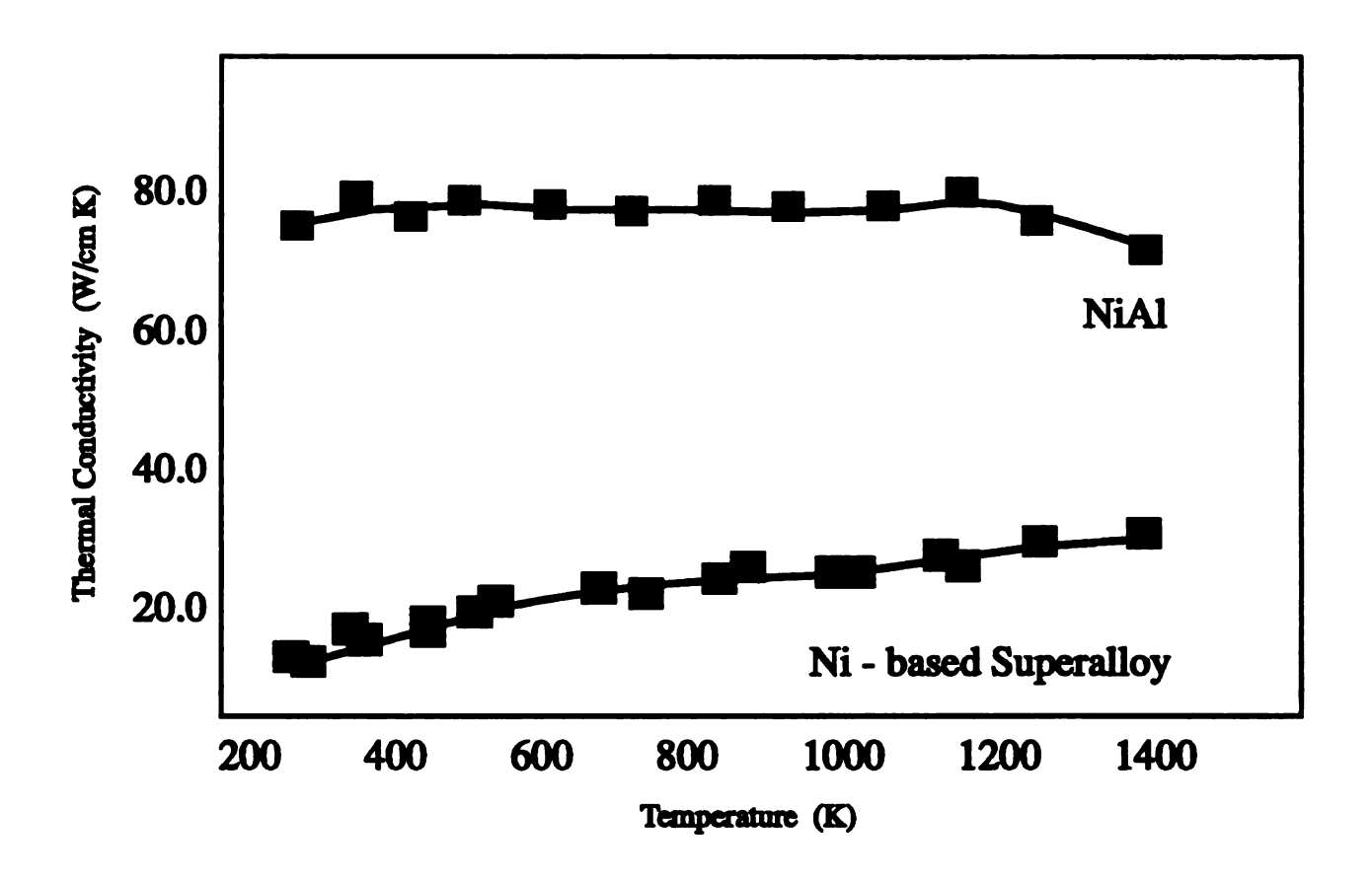


Figure 3

Thermal conductivities of B2 FeAl, NiAl, CoAl, common nickel based superalloys and other common alloys. Adapted from [4]

6

technique for 50 at%Al FeAl, NiAl and CoAl are 163-256GPa, 232GPa and 296GPa respectively [7,8]. These values are comparable to the upper value of 206.8GPa for nickel based superalloys [9].

Although the advantages of B2 FeAl are numerous, this material generally lacks extensive ductility and toughness at ambient temperatures, especially for the stoichiometric (Fe-50Al) composition. First, the binding force, (ordering energy) between the different atomic species in the B2 alloys has a directional character and is stronger than regular metallic bonding [6]. It is believed that this type of bonding decreases ductility by making dislocation motion more difficult. In addition, this bonding causes this class of materials to have very anisotropic moduli [6]. Table 1 shows the first principles calculations of the elastic constants for Fe-50 at.% Al (hereafter referred to as Fe-xx.xAl) [6] and experimentally observed values for Fe-40Al at 298K [8].  $(C_{11} - C_{12})$ corresponds to the [110] shear on the (110) plane, and  $C_{44}$  corresponds to the [110] shear on the (001) plane. E is Young's modulus, G is the shear modulus and R represents the shear elastic anisotropy factor. When designing single crystal structural components that would use this type of material, elastic anisotropy may be a hindrance. The stresses on the part would have to be analyzed and the part would then have to be crystallographically oriented in order to provide the best response to the applied load/loads. Low ductility, low toughness and elastic anisotropy are complications that make fabrication of these materials difficult with respect to conventional methods, such as casting and machining. However, methods such as powder processing, extrusion and directional solidification have been successfully employed to varying degrees [4].

A very important factor which should not be forgotten, is the propensity for these alloys to have high vacancy concentrations. High vacancy concentrations have been observed following both quenching and less severe cooling rates. The first studies of quenched in vacancies in FeAl were carried out using resistivity,



Table 1. Elastic Constants of FeAl at room temperature (in units of GPa)[6,8].

Type of data		C <sub>11</sub>	C <sub>12</sub>	C44	E	G	R
First Principles	[6] Fe-	290	130	165	347	123	104
50A1							
Experimental values [8] Fe-40Al		181	114	127			

concentration for the seen that was stoichiometric increasing vacancy occurrent.

hardness to recently, t with corre illustrates which have 1273K [1]

Rie

nickel-ba these allo several co also be re

rates [18]

F

et al. [21] Fe-39.8A1 dilatometry and field ion microscopy [10-13]. These studies revealed vacancy concentrations as high as 1.4 x 10<sup>-2</sup> and 2.2 x 10<sup>-2</sup> (as quenched from 1323K (.86T<sub>m</sub>)) for Fe-46Al and Fe-51Al respectively. Typical metals have vacancy concentrations on the order of 10<sup>-3</sup> to 10<sup>-4</sup> near their melting points [14]. From the vacancy studies, it can be seen that vacancy concentration decreases with increasing iron rich deviations from stoichiometry. This decrease in vacancy concentration may be a direct result of increasing melting temperature with decreasing aluminum content. Figure 4 illustrates vacancy concentration as function of aluminum concentration [15].

Rieu and Goux [10] and Weber et. al. [16] were the first to attribute increases in hardness to increases in the number of retained vacancies following quenching. More recently, this phenomenon has been attributed to large increases in yield strength (along with corresponding decreases in ductility) as a function of cooling rate [17,18]. Table 2 illustrates the change in critical resolved shear stress (CRSS) for B2 FeAl single crystals which have been slow cooled and oil quenched, following a 24 hour anneal in argon at 1273K [19]. Figure 5 illustrates engineering stress-strain curves for extruded polycrystalline Fe-40Al samples subjected to various post-homogenization quenching rates [18].

FeAl has a larger thermal expansion coefficient than NiAl, CoAl, nickel and nickel-based alloys. This may be related to the large thermal vacancy concentrations in these alloys. Figure 6 displays plots of Δl/l versus temperature for FeAl, NiAl,CoAl, several common alloys and alumina [1]. The large thermal vacancy concentrations may also be related to the relatively poor creep strength reported for FeAl [20]. Whittenberger et al. [21] determined the work hardening coefficient to be 0.0015E for polycrystalline Fe-39.8Al compression tested at 1200K.

2 x 10<sup>-3</sup>

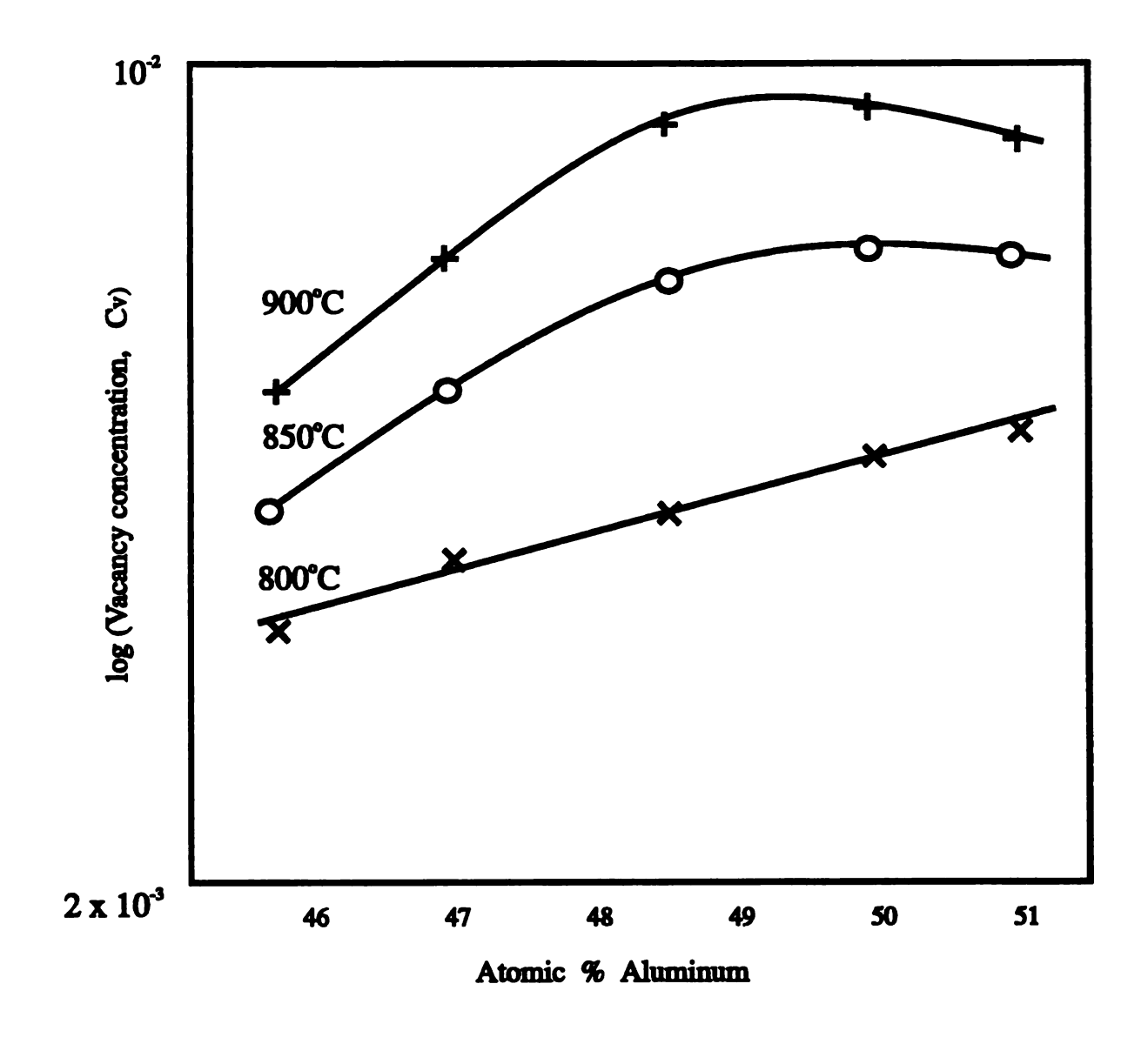


Figure 4

Vacancy concentration vs. at. % Al for FeAl. Adapted from [15]

Fo Fo

Table 2. Values of critical resolved shear stress[20].

Alloy	Heat treatment	CRSS (MPa)
Fe-39.2 at%Al	Slowly cooled	97 +/- 13
Fe-39.2 at%Al	Oil quenched	304 +/- 16
Fe-48.8 at%Al	Slowly cooled	202 +/- 17
Fe-48.8 at%Al	Oil quenched	318 +/- 16

600 GWL93)

0

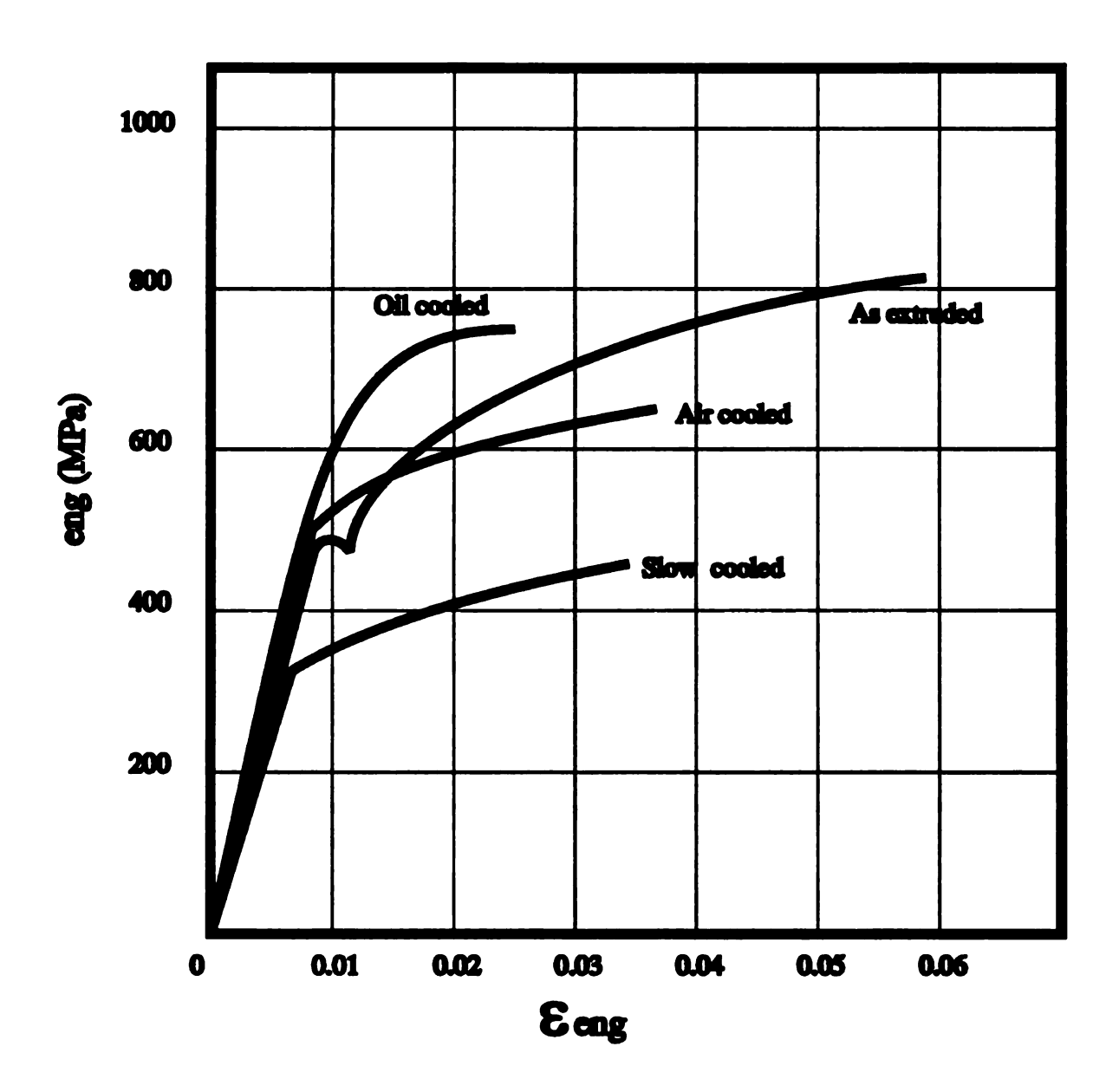


Figure 5
Engineering stress-strain curves for extruded polycrystalline
Fe-40Al which has been quenched at different rates. Adapted
from [18]

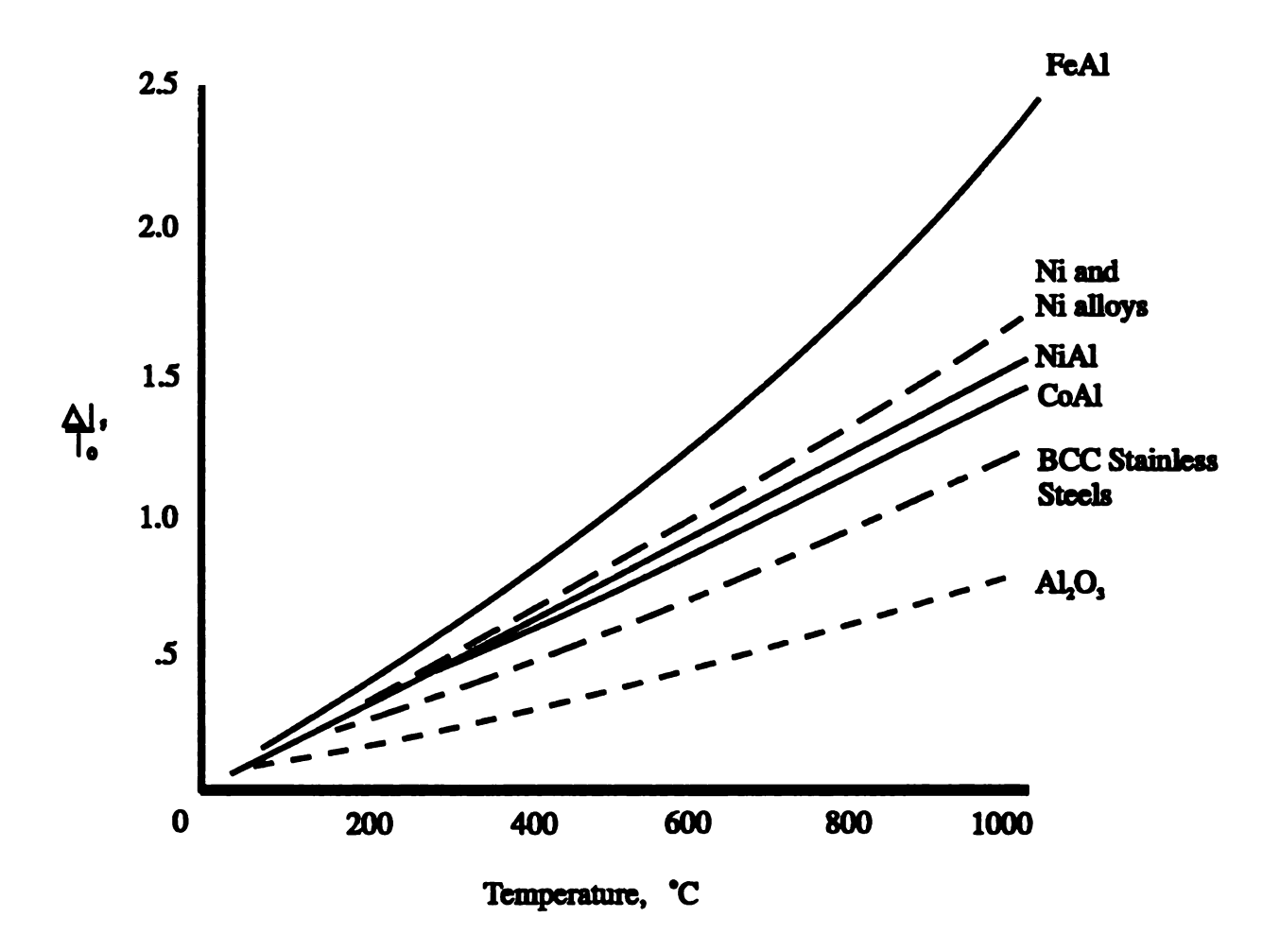


Figure 6
Thermal expansion plots of B2 FeAl, NiAl, CoAl, several common alloys and alumina. Adapted from [1]

13

In addition, they determined the elastic modulus to be 93GPa for the alloy at 1200K. Recall that the room temperature modulus for Fe50-Al ranged from 163 to 265GPa. Figure 7 illustrates the approximate creep strengths of Ni, Fe, FeAl, NiAl, CoAl and nickel-based superalloys.

The potential benefits for using FeAl are numerous. However, more information is needed before this material can be made commercially useful. Hopefully, further study of this material will benefit attempts to improve the properties of all B2 aluminides.

#### 1.1 Background

In order to gain a better understanding of B2 FeAl (a bcc based intermetallic alloy), it is helpful to compare the mechanical behavior and deformation mechanisms of this alloy to that of standard bcc metals. The information gathered from this avenue of investigation is believed to be beneficial in understanding and hopefully in finding new ways to improve the flow and fracture behavior of this material.

The deformation of bcc metal is controlled primarily by the motion of <111> screw dislocations. It is known that the core structure of the screw dislocation produces an intrinsic lattice friction mechanism, thereby controling dislocation motion [22]. For example, depending on the direction and sense of an applied stress on a single crystal (see figure 1), screw dislocations may move on different glide planes and in different directions in the bcc unit cell. This type of deformation behavior allows the material to satisfy Von Mise's criterion for 5 independent slip systems. Yamaguchi [22] conducted atomistic studies of the core structures of 1/2 <111> screw dislocations, 1/2<111> non-screw dislocations on {110} and {100} planes, and twinning dislocations on {112} twin boundaries in the bcc structure. These studies revealed that the Peierls stress for screw dislocations are at least three times higher

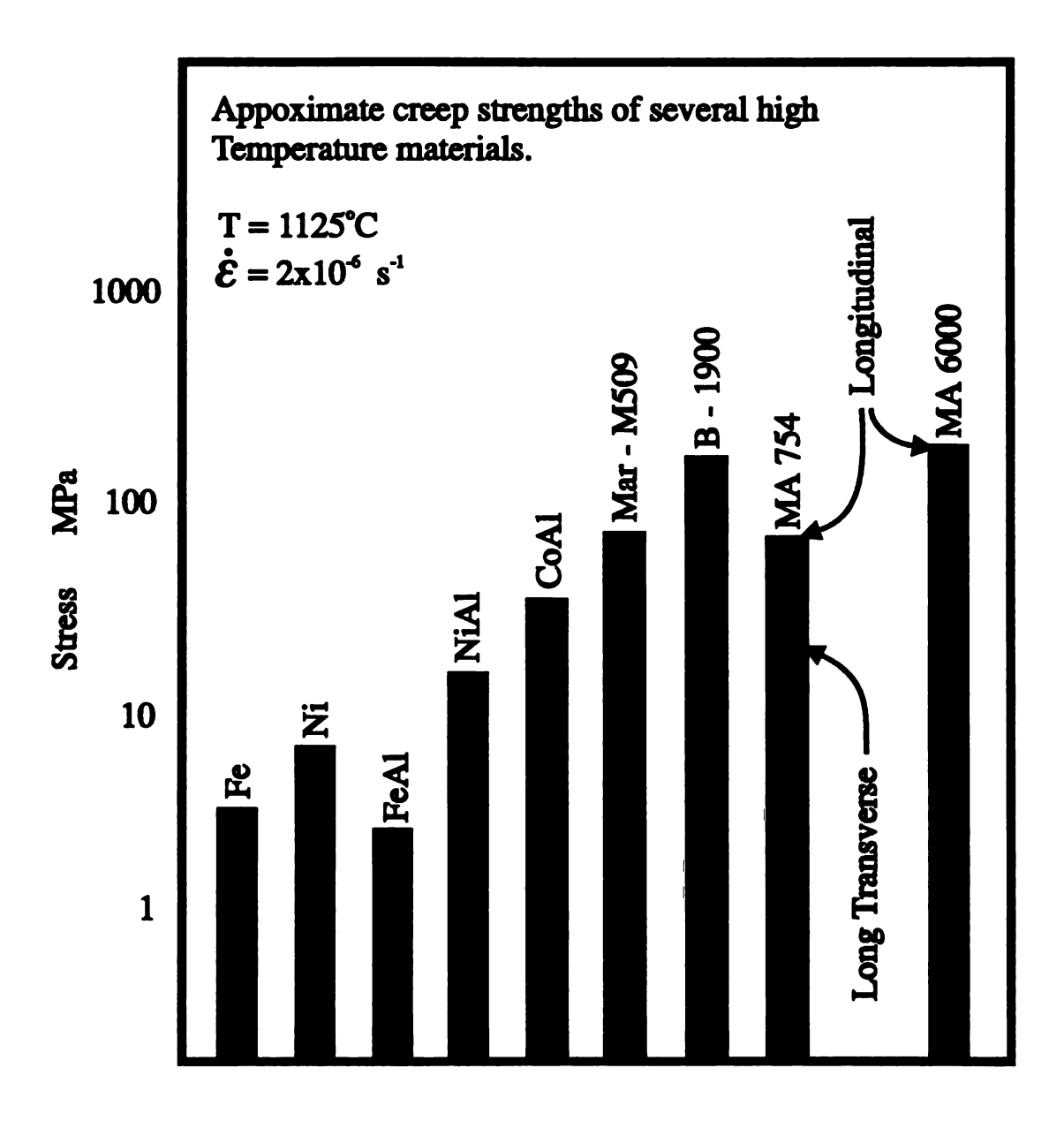


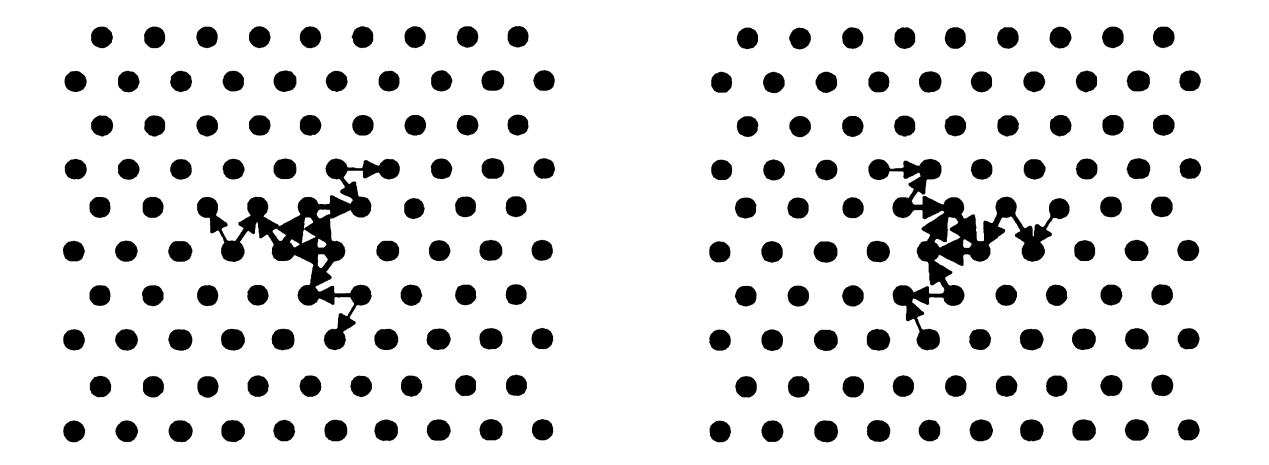
Figure 7

Approximate creep strengths of several intermettalics in comparison to superalloys, iron and nickel. Adapted from [20]

than that of non-screw dislocations, implying that the screw dislocation is of primary importance for understanding the plastic behavior of bcc metals and alloys.

The increase in the resistance that the crystal line lattice offers to the movement of a <111> screw dislocation is a direct result of the difference in the structure of the screw's core when compared to that of edge-type dislocations. The core structure of the <111> screw dislocation is non planar and possesses a 3-fold symmetry, which is illustrated in figure 8. These images correspond to viewing the core end-on (down the line direction). Figures 8(a) and (b) display computer models of relaxed 1/2<111> screw dislocation cores. The small circles represent atom positions projected on the (111) plane. The arrows represent the [111] disregistry of pairs of atoms in the core and display the relative displacement in the direction of the Burgers vector (i.e. into the plane of the paper). The relative magnitude of the displacements are represented by the relative magnitudes of the arrows. Figure 8(c) provides an illustration of the orientations of the traces for the planes of relaxation in the [111] zone [23]. For the isotropically elastic models shown, the displacements are concentrated on the three intersecting {110} planes. Each {110} plane contains an unstable fault caused by a 1/6[111] partial dislocation which (unlike Schockley partials) does not bound a stable stacking fault [23]. These fractional cores are also spread asymmetrically on three {112} planes in a given twinning sense.

The screw dislocation core is immobile in the relaxed configuration and must become planar prior to motion. This can be described as a widening and flattening of the core, which enables the atomic displacements to be constricted onto a single glide plane. This in turn causes the critical resolved shear stress (CRSS) to be dependent on stress orientation. In fact, the glide plane may vary with the orientation and sense of the applied stress. In contrast, non-screw (i.e. edge) dislocations are planar and their cores do not have to be compressed onto their slip plane prior to motion.



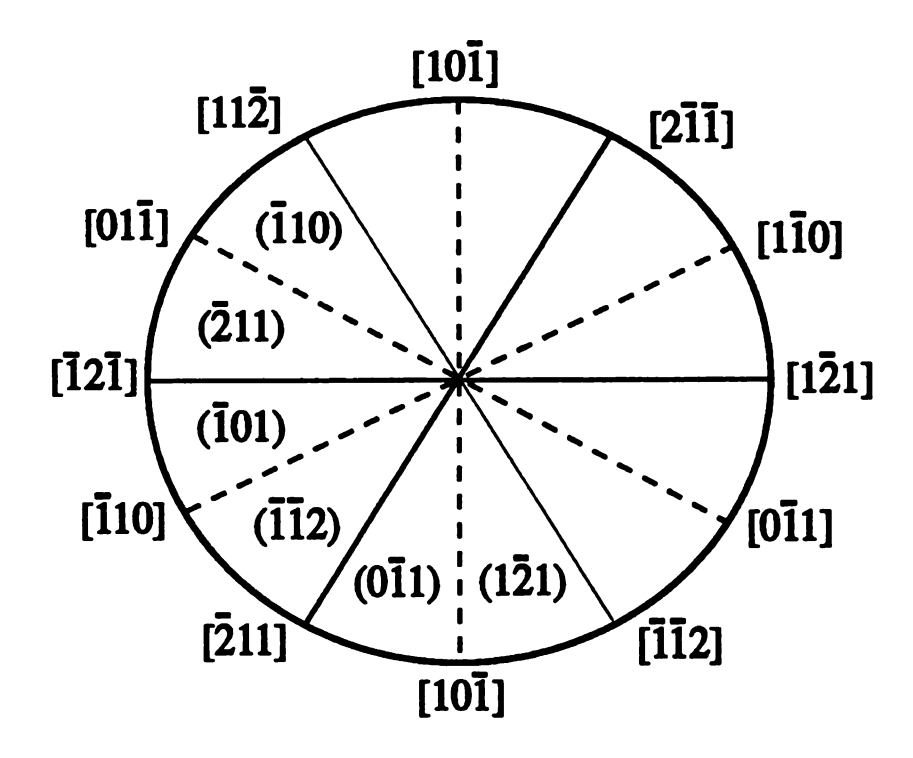


Figure 8

(a) and (b) Computer models of two possible <111> screw dislocation cores predicted for bcc metals. (c) Orientations of relaxation planes for the cores. Adapted from [23]

## 1.2 B2 vs. bcc Dislocation Behavior

Considering a binary system with type A and B atoms, an ordered lattice is formed when A-B type bonds are energetically preferred. Since the B2 structure is simply an ordered version of the bcc structure, it is believed that the mechanical behavior of this material is governed by 1/2<111> screw dislocations as well. Takeuchi [24] has performed atomistic studies showing that the core structure and core transformations of an  $a_0/2<111>$  screw dislocation in a "model" B2 lattice are analogous to those of a 1/2<111> screw dislocation in the bcc structure. However, there is an important distinction between bcc and B2 alloys which must be discussed.

The ordered arrangement of atoms in the B2 lattice is affected by dislocation movement. For instance, when a 1/2<111> dislocation passes through an ordered lattice on certain planes it alters the structure, causing like atoms (which want to repel one another), to be nearest neighbors. This mismatching of atoms is described as an antiphase boundary (APB). In order to reorder the crystal lattice, a second dislocation must follow the path of the first dislocation. The arrangement of two dislocations (each referred to as a partial or superpartial) separated by an APB in this way, is called a superdislocation. A superdislocation exists as a balance between the repulsive force of the partials and the formation energy of the APB lying between them (see figure 9 for an illustration).

It is important to note that the superpartial dislocations need not move together as closely spaced pairs. In ordered metals, the spacing of the partial dislocations is inversely proportional to the formation energy of the APB. The restriction on the arrangement of the superpartials is analogous to that for the spacing of Schockley partials in fcc metals. In other words, if the APB energy is low enough (weak repulsive force between like atoms) the partials may move separately, leaving APB trails in their wake. Table 3 illustrates the dislocation configurations possible for B2 FeAl [25].

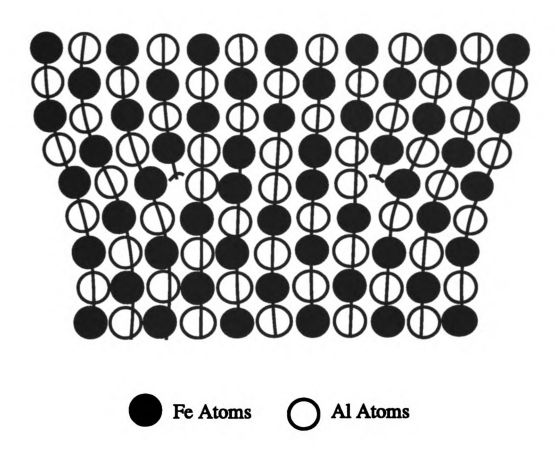


Figure 9

B2 superdislocation schematic displaying two super patials seperated by an APB. Adapted from [48]

<u>Table 3 Possible B2 Dislocation configurations [25].</u>

Dislocation type	Burgers vector	<u>Illustration</u>
Superdislocation	2x a/2<111>	⊥ xxxxxx⊥ nnajb
Ordinary with ABP	a/2<111>	XXXXXXX T
Ordinary	a<100>	1

Yamaguchi [22] and Fu and Yoo [6] have used pair potential models and first principles calculations to empirically determine that the a<sub>0</sub>/2<111> type APBs are most energetically favorable on the {110} and {112} planes in the B2 structure. Yamaguchi [22] calculated that <111> dislocations with higher APB energies should slip on {110} planes, while <111> dislocations with lower APB energies should slip on {112} planes. It should be noted that pair potential modeling is based strictly on unlike nearest neighbor bonds having lower energy than like nearest neighbor bonds. This type of modeling does not take into account the differences in bond energies and APB energies of specific B2 alloys [5].

# 1.3 Dislocation Behavior of B2 Aluminides With Respect to Temperature

Experimental studies of single and polycrystalline B2 FeAl have shown that the predominant slip mode (at ambient temperatures) is <111>{110} [26-30]. Yamagata and Yoshida [26] found that FeAl single crystals, deformed in compression, typically had slip systems of <111>{112} at low temperatures (77K) and slip systems of <111>{110} at higher temperatures (300-473K). In addition, at higher temperatures, more cross slip from {112} to {110} was found to occur. These results were observed to be strongly dependent on orientation and temperature. Similarly, a small amount of cross slip from {110} to {112} was observed by Yamaguchi et. al. [28] near 623K for an Fe-47.2Al sample deformed in compression and oriented close to the [011]-[111] border of the unit triangle (see figure 10).

Although room temperature compressive deformation of FeAl is found to be controlled primairly by <111> screw dislocations with <111>{110} as the dominant slip mode, NiAl and CoAl deform primairly by <100> edge dislocations. The predominant slip modes in NiAl are <100> {001} and <100>{011} [5, 31-36]. However, <111> slip has been activated in B2 NiAl at low temperatures [37,41] (from 4.2K to 100K) and by orienting single crystals to hard orientations (near <001>) [36-41]. In addition, <111> dislocations have been activated in NiAl by



Figure 10

Experimental image of cross slip from {110} to {112} for Fe-47.2Al deformed near the [011]-[111] border at 673K. Adapted from [28]

alloying additions [42,43]. It is interesting to note that the activation of <111> slip in NiAl has not been observed to improve the mechanical properties of this particular alloy.

In a manner similar to NiAl, CoAl deforms primairly by <100> edge dislocations (over a wide temperature range) on {001} and {011} planes [20,44-46]. However, some <111> and <110> dislocations have also been observed [45]. Although CoAl has the highest modulus of the three B2 aluminides discussed, attempts to improve its ductility have failed and it is extremely brittle, even at relatively high temperatures.

At elevated temperatures, NiAl and CoAl tend to show little deviation in their slip direction or slip systems. However, FeAl exhibits a transition temperature range in which the slip direction changes from <111> to <100>. This behavior has been shown to be influenced by orientation and stoichiometry [28-30]. Interestingly, [001](100) dislocations have been observed in single crystal FeAl compressed within 15° of [001] at 873K [47]. This is surprising, due to the low Schmid factor expected for <001>{100} dislocation slip in this orientation and the fact that optical slip trace analysis revealed {110} to be the active slip planes [47].

A study on polycrystalline samples by Mendiratta et al. [30] found that the transition temperature was around .4 -.5T<sub>m</sub>. They found the transition temperature increased with increasing iron content. Figure 11 illustrates the change in slip direction for atomic percent aluminum versus tempreature [30].

Studies by Umakoshi and Yamaguchi [28,29] found the transition in slip direction occured near .4-.5T<sub>m</sub> for single crystal B2 FeAl specimens. Contrary to Mendiratta et al. [30], they observed that the transition temperature increased with increasing aluminum content. Figure 12 shows at.% Al versus transition temperature for single crystals oriented near the [111] portion of the unit triangle [29]. The lower ends of the error bars in figure 12 correspond to the temperature up

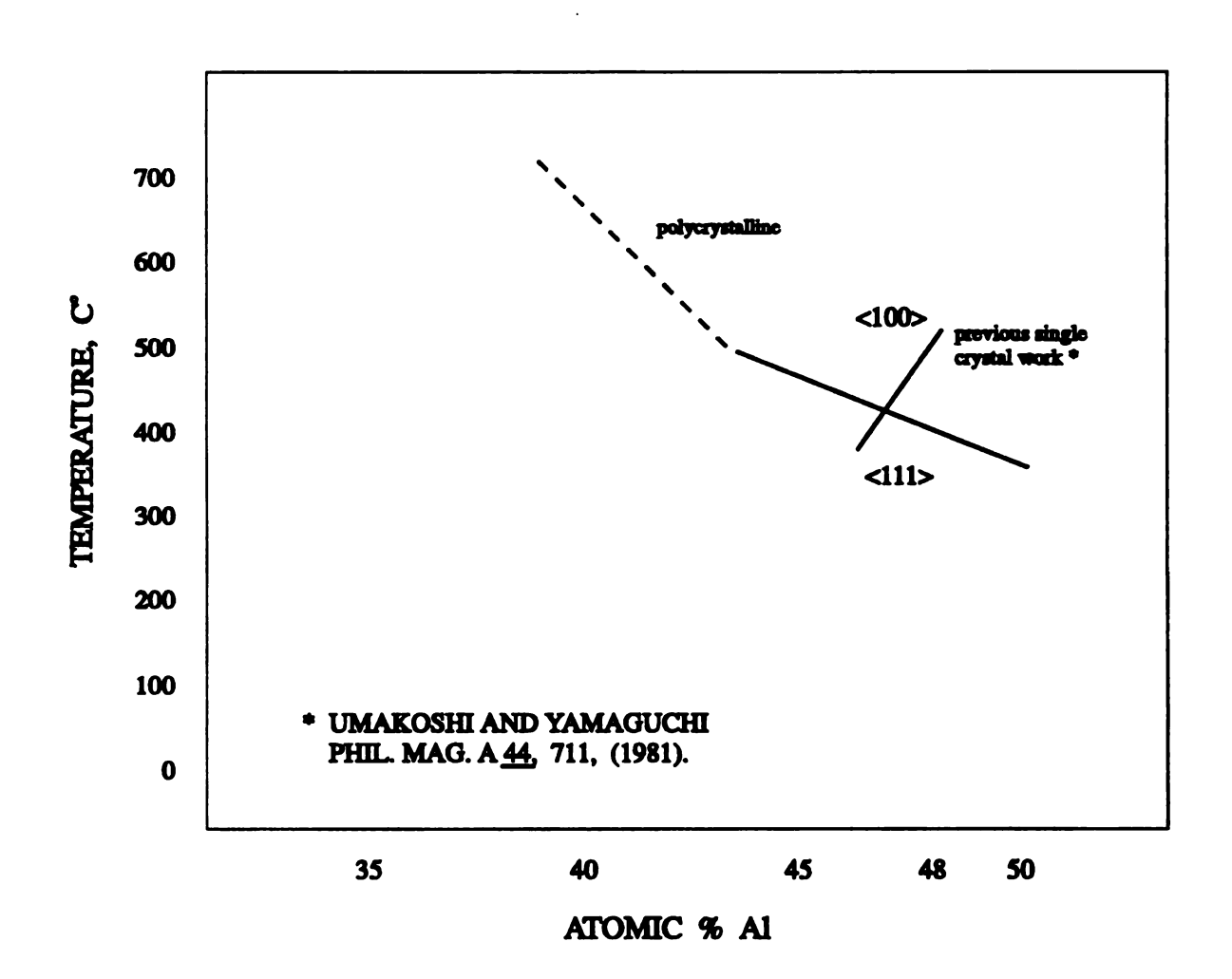
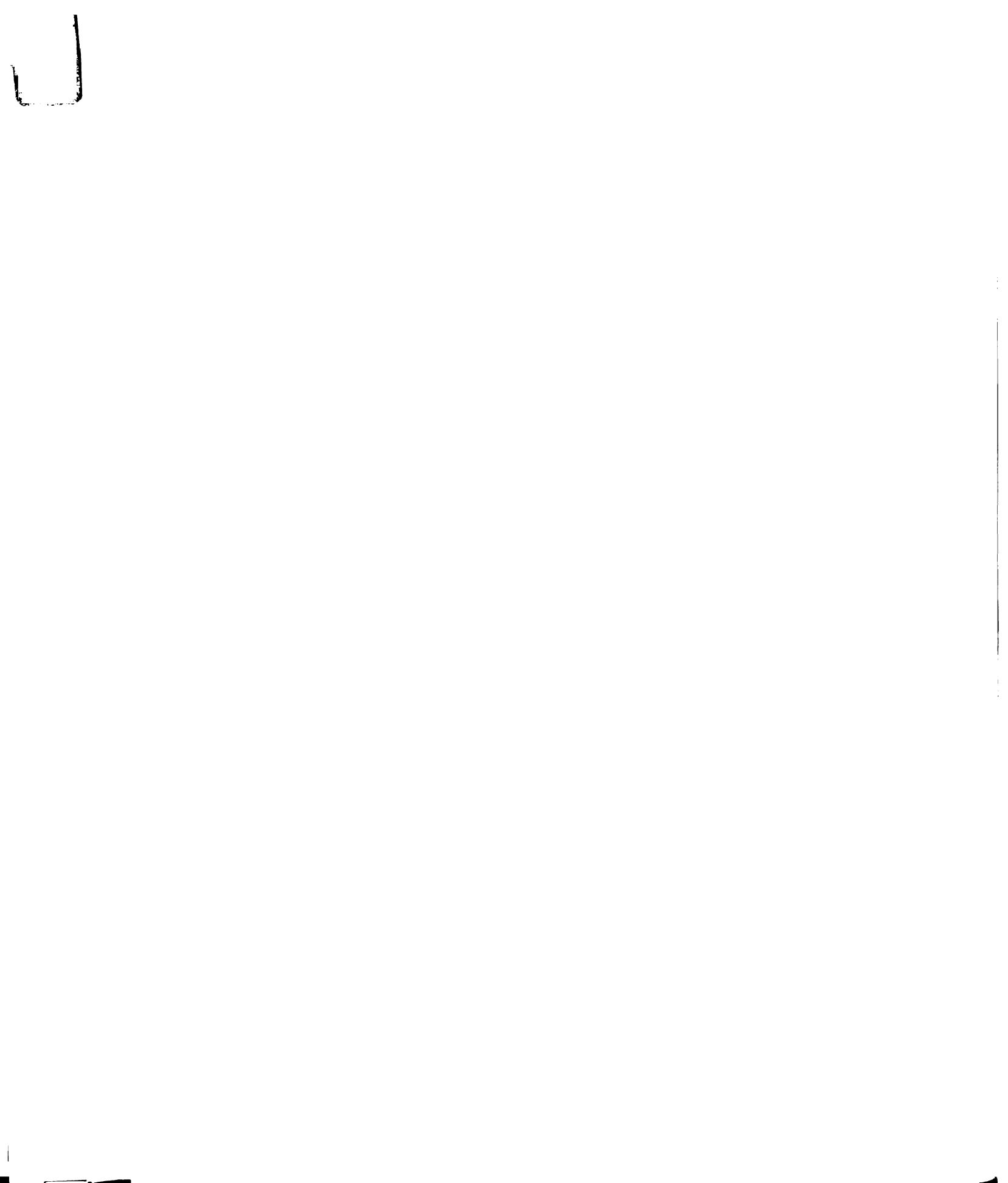


Figure 11

Change in slip direction for polycrystalline and single crystal B2 FeAl as a function of at.% Al vs. temperature. Adapted from [30]



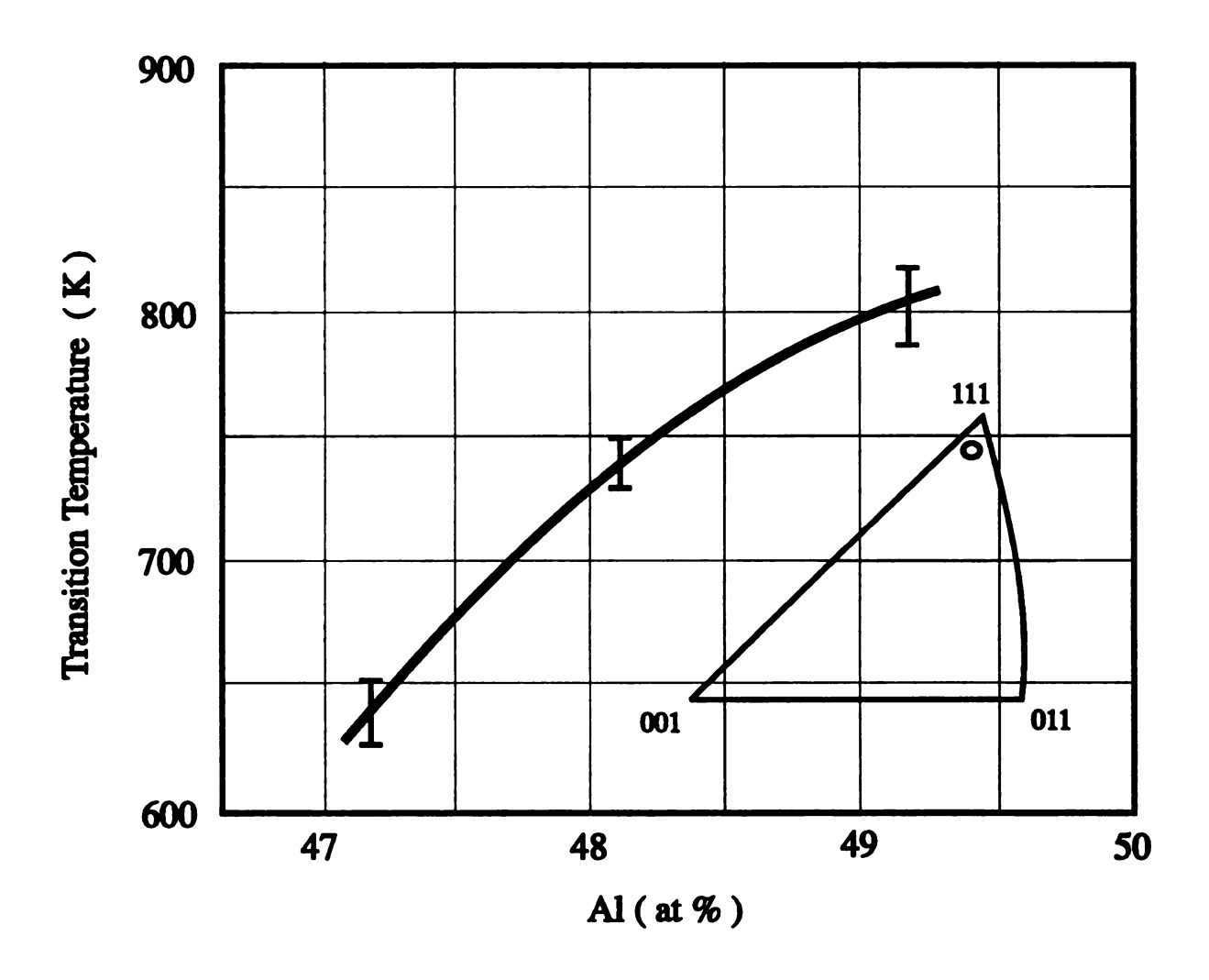
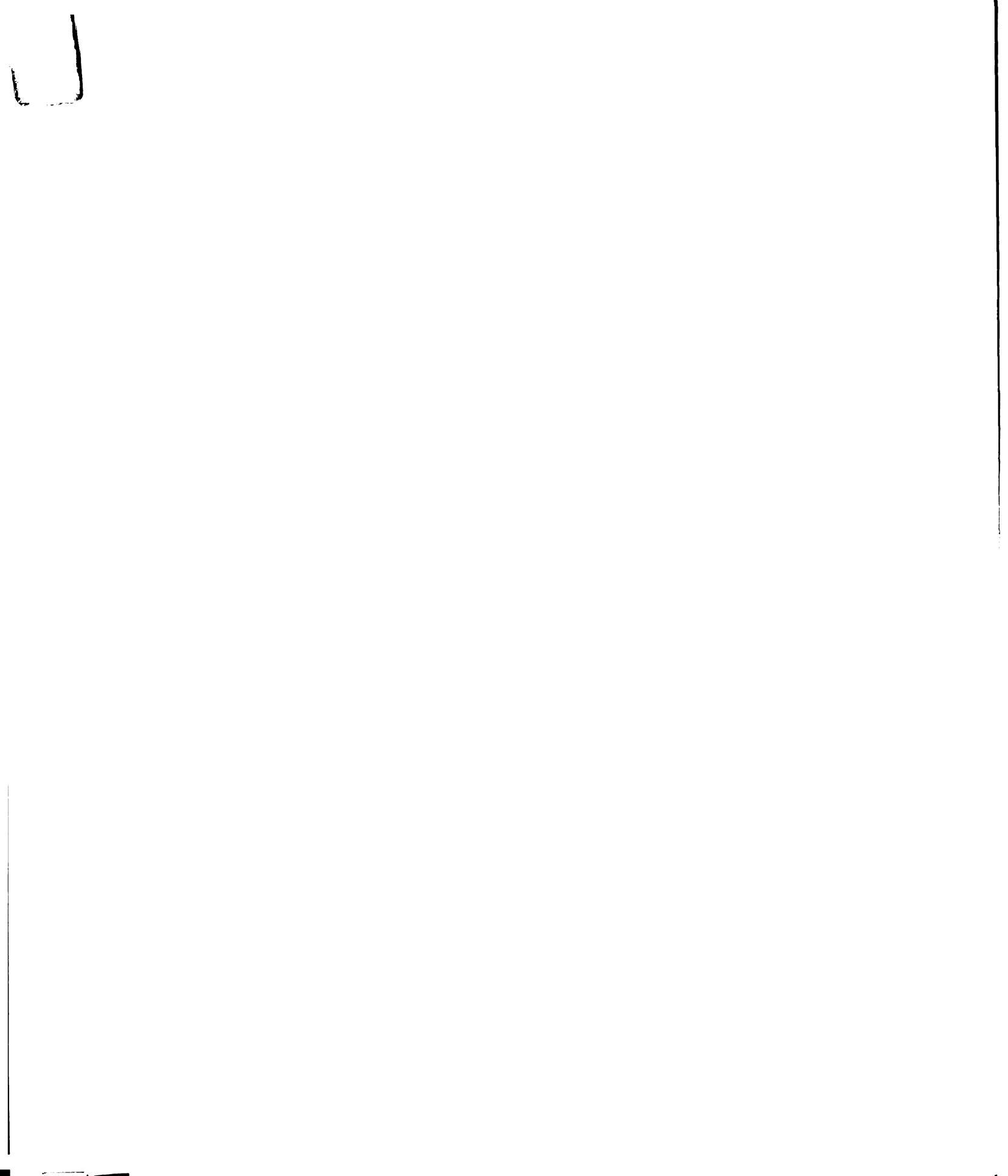


Figure 12

Atomic percent Al vs. slip transition temperature for FeAl single crystals oriented near the [111] portion of the unit triangle. Adapted from [29]

to which <111> slip is dominant and the upper ends correspond to the temperature above which <001> slip is preferred. Figure 13 shows the dependence of the transiton temperature with respect to orientation for Fe-49.2Al single crystals [29]. Figure 14 shows the results of the orientation and temperature dependence for the Fe-47.2Al alloy. The main features of the results in the figure are: The transition in slip occurs at around 670K (~ .44T<sub>m</sub>) for crystals oriented near the right hand portion of the unit triangle. As the deformation temperature is increased, the area in the unit triangle showing the <100> type slip becomes larger. There is a tendency for the <100>-type slip to be along the [010] for crystals having stress axes located near the center of the unit triangle. However, for crystals with stress axes located in the upper right area of the unit triangle, the primary slip direction for the <001>-type slip is [001]. Single slip along the primary [001] direction is limited to crystals having orientations in the [111]-side of a narrow band in the unit triangle (dashed line) along the [001]-[111] boundary. However, for most orientations in the region showing the <001>-type slip, except for those in the narrow band, either duplex slip of [001] and [010] or single slip along [010] takes place [28]. Figure 15 indicates that the transition in slip occurs somewhere between 773K and 873K for an Fe-49.2Al alloy [29]. This data verifies the increase in the <111> to <100> transition temperature with increasing aluminum content in single crystals (670K for Fe-47.2Al versus 773-873K for Fe-49.2Al).

Optical slip line examinations of single crystal Fe-47.2Al samples (deformed in different crystallographic orientations at 773K) are displayed in figure 16 [28]. Figure 16 (a) illustrates [001] (110) slip, (refer to figure 14(c) for the corresponding deformation axes). Figures 16(b) and (c) illustrate [010](001) and duplex [010](001)-[001](110) respectively. Inspection of the figures, shows that [010](001) slip and duplex slip of [010](001)-[001](110) are wavier than [001](110) slip. Referring back



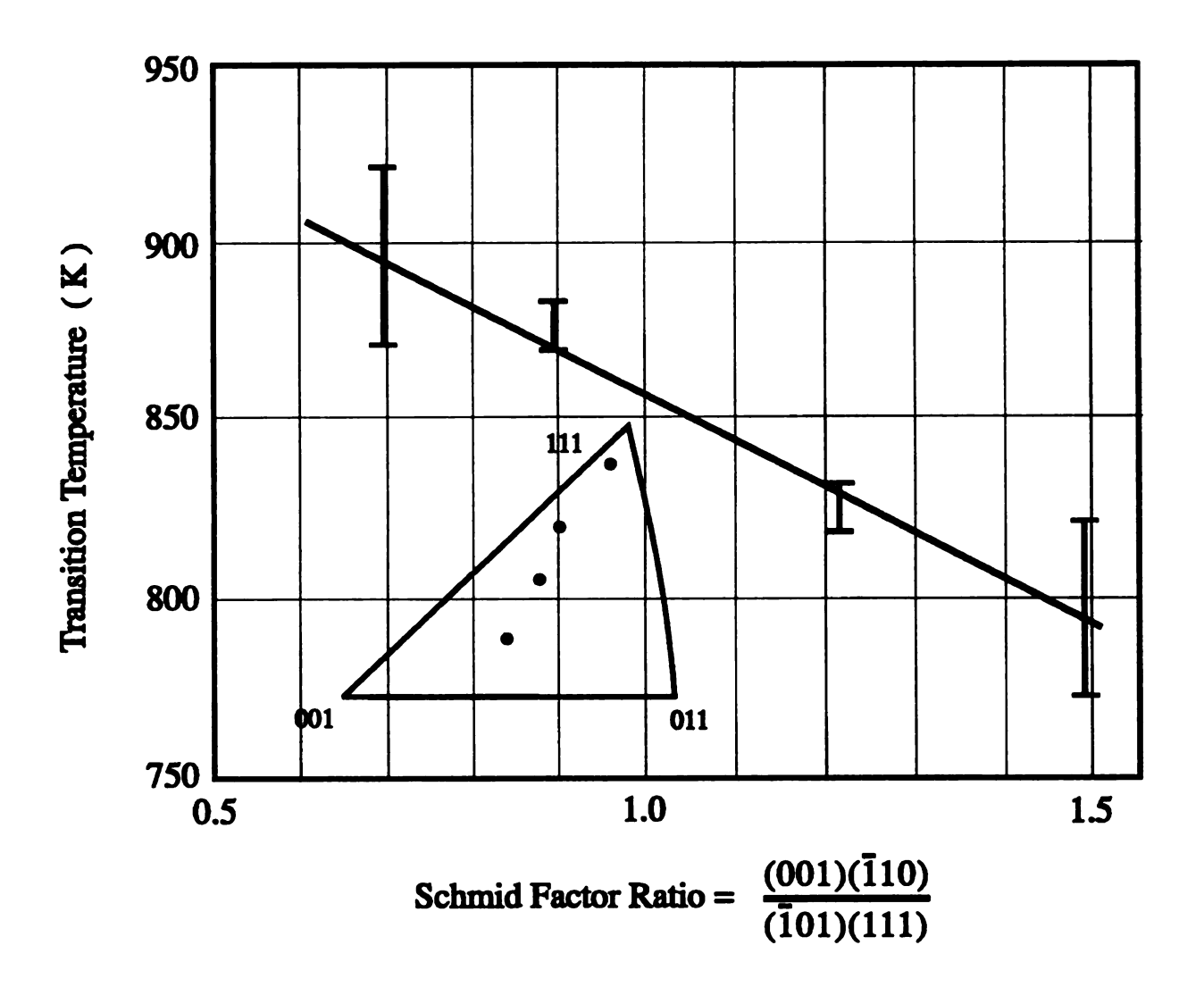


Figure 13

Slip transition temperature dependence on orientation for Fe-49.2Al Adapted from [29]

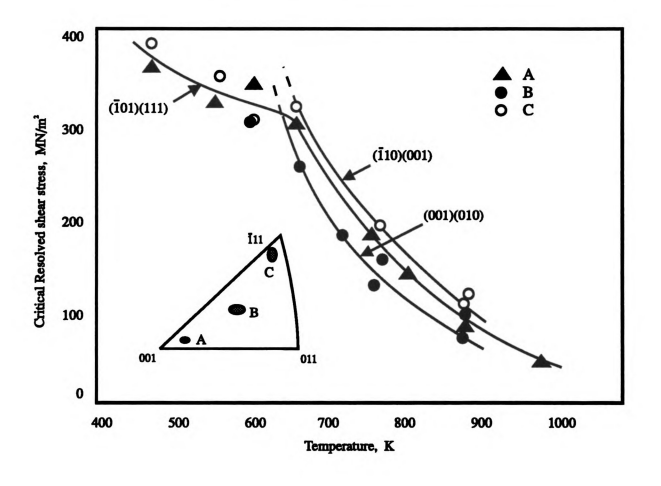


Figure 14

Slip transition orientation and temperature dependence for Fe-47.2Al.

Adapted from [28]

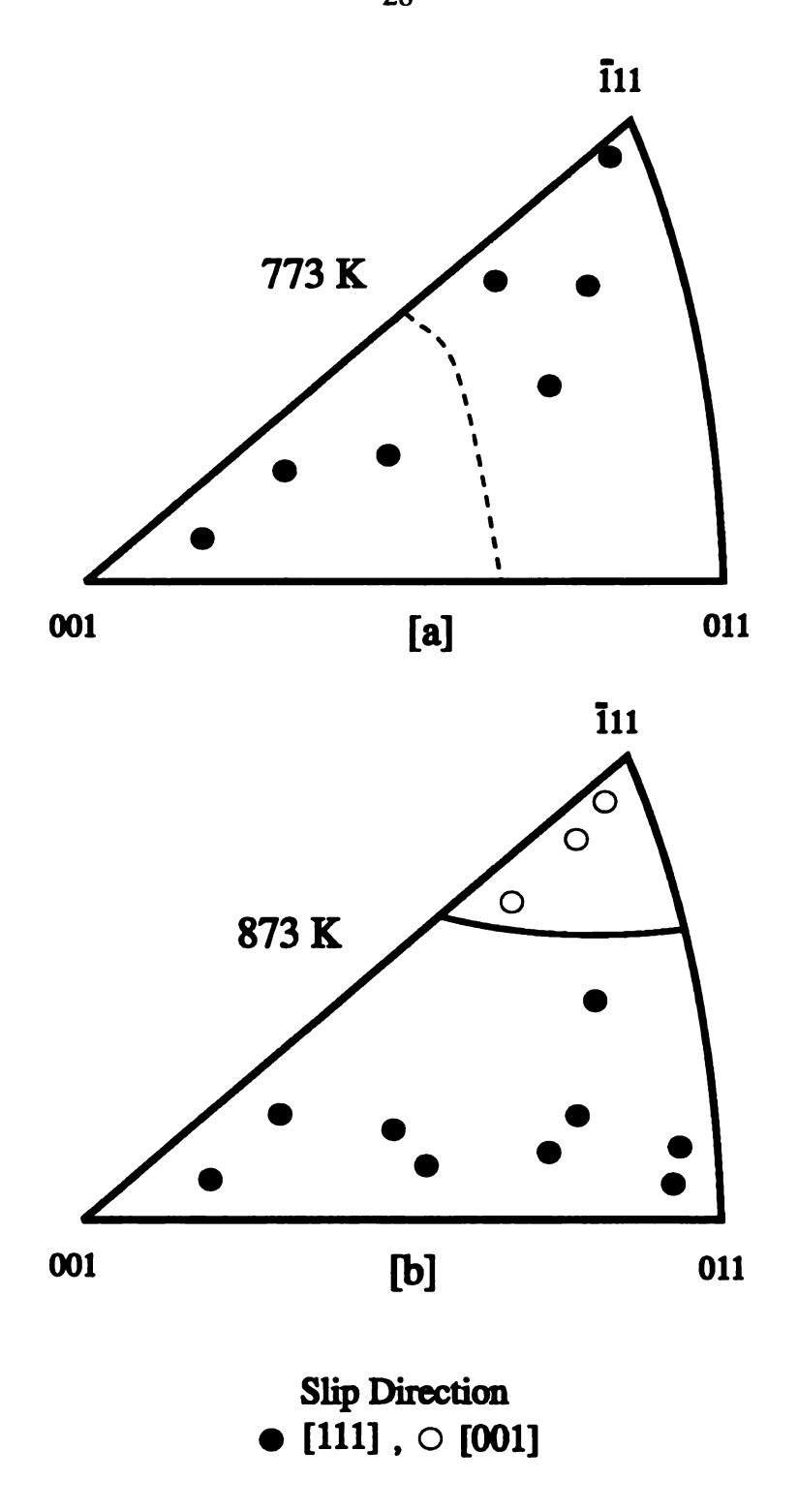


Figure 15

Indication that the <111> - <100> slip transition occurs somewhere around 773K - 873K for an Fe-49.2Al alloy. Adapted from [29]

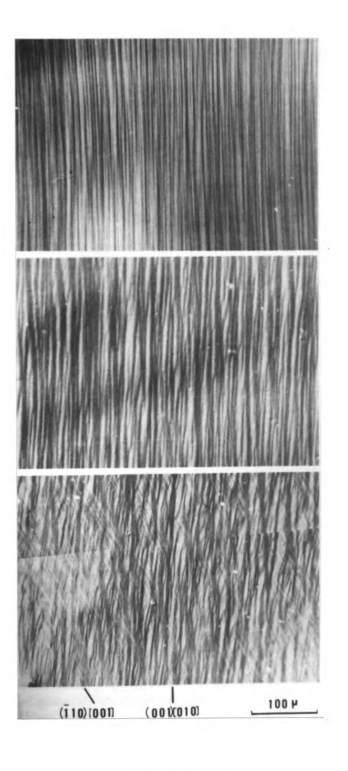


Figure 16

Slip lines corresponding to (a) [001](110) (b) [010](001) and (c) [010] (001) in combination with [001](110) slip. Adapted from [28]

to figure 10, one sees that <111> type slip is the finest and most homogenous of them all.

## 1.4 Properties of B2 FeAl

The properties of B2 FeAl have been shown to be dependent on a number of factors including: deformation temperature, testing environment, alloying additions, stoichiometry and thermal history (annealing and cooling rate). These effects will be reviewed in an attempt to gain as complete an understanding of the complex behavior of this material as possible.

## 1.4.1 Effects of Temperature, Test Environment and Alloying Additons

Tensile studies on polycrystalline Fe-40Al have shown increases in ductility from approximately 5% at room temperature to 81% at 1073K [48,49]. In addition, the yield strength has been found to remain constant up to 673K, reach a maximum value at 873K and then decrease rapidly [49]. Figure 17(a) illustrates yield strength versus temperature for directionally solidified Fe-40Al. Figure 17(b) shows percent elongation versus temperature for the same alloy.

With respect to testing environment, FeAl has been shown to be susceptible to water vapor induced embrittlement [50]. However, microalloying FeAl with boron and testing the material in an oxygen environment has been found to improve the ductility of the material [17,51,52,53]. It has been hypothesized that boron reduces water vapor embrittlement by strengthening grain boundaries [17,51,52]. Table 4 illustrates the observed effect of testing environment on the room temperature tensile properties of Fe-40Al with and without boron. Speculation as to why oxygen improves the ductility of FeAl are oxygen competes with water for reaction with the crack tip atoms, oxygen acts as a "getter" of atomic hydrogen (forms stable OH species) and/or oxygen physically shields the crack tips from water [53]. Figure 18 displays observed percent elongations versus water content for Fe-35Al in oxygen and Fe-33Al in argon. Figure 19 displays the results of an additional alloying

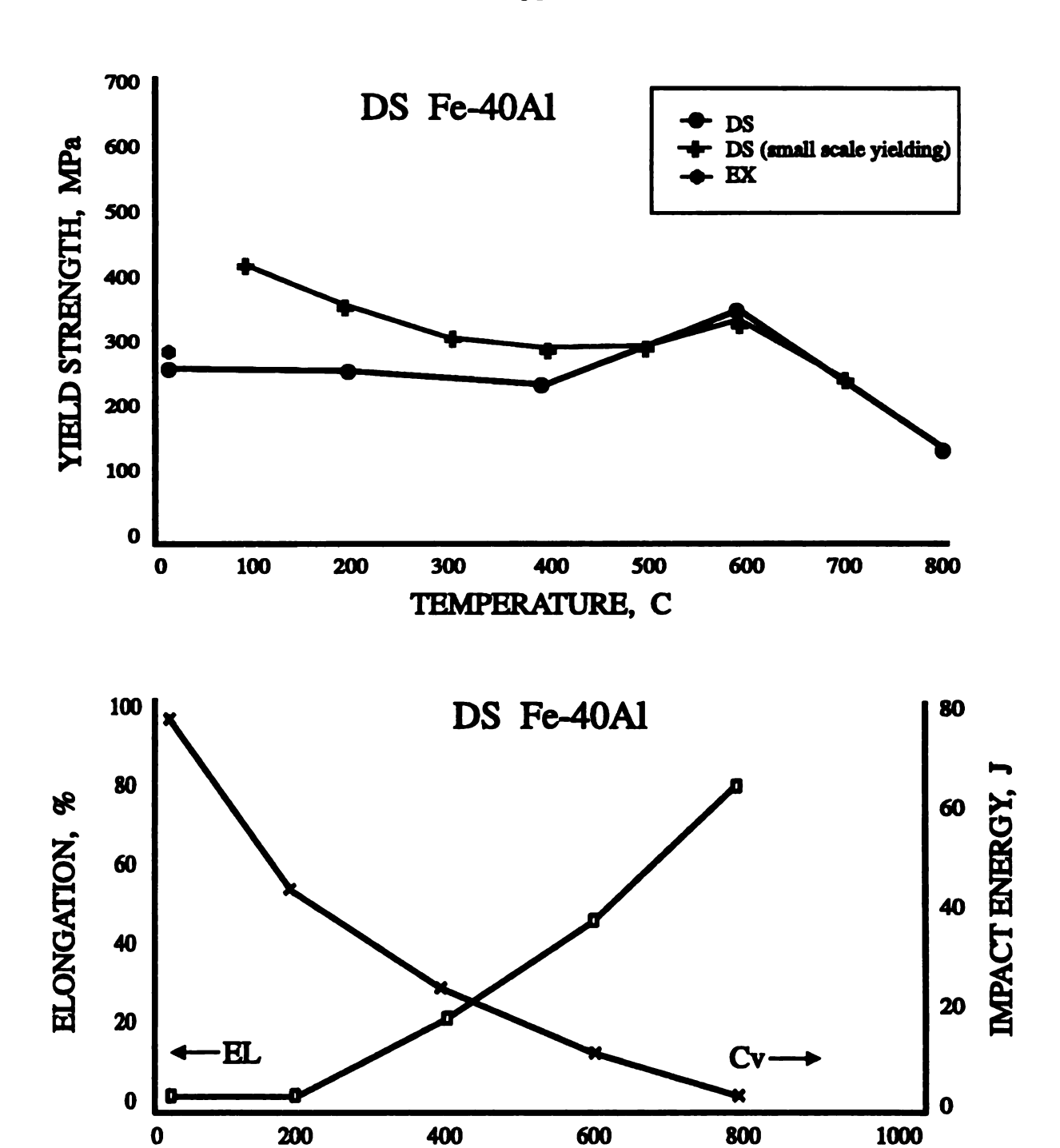


Figure 17

(a) Yield strength vs. temperature for directionally solidified Fe-40Al

TEMPERATURE, C

(b) Percent elongation vs. temperature for the same alloy. Adapted from [49]

<u>Table 4</u>
<u>Effect of Test Environment on Room Temperature Tensile Properties</u>
of FeAl (40 at. % Al), With and Without Boron [51].

Test Environment	Strength (MPa)		Ductility (%)	Fracture Modea
	Yield	Ultimate		
Air (no Boron)	390	405	1.2	GBF
O <sub>2</sub> (no Boron) <sup>b</sup>	402	537	3.2	GBF
Air (Boron)	391	577	4.3	TF
O2 (Boron) <sup>b</sup>	392	923	16.8	TF

<sup>a</sup>GBF = grain-boundary Fracture; TF = mainly transgranular fracture.

bO<sub>2</sub> Pressure: 6.7 x 10<sup>-4</sup> Pa.

33

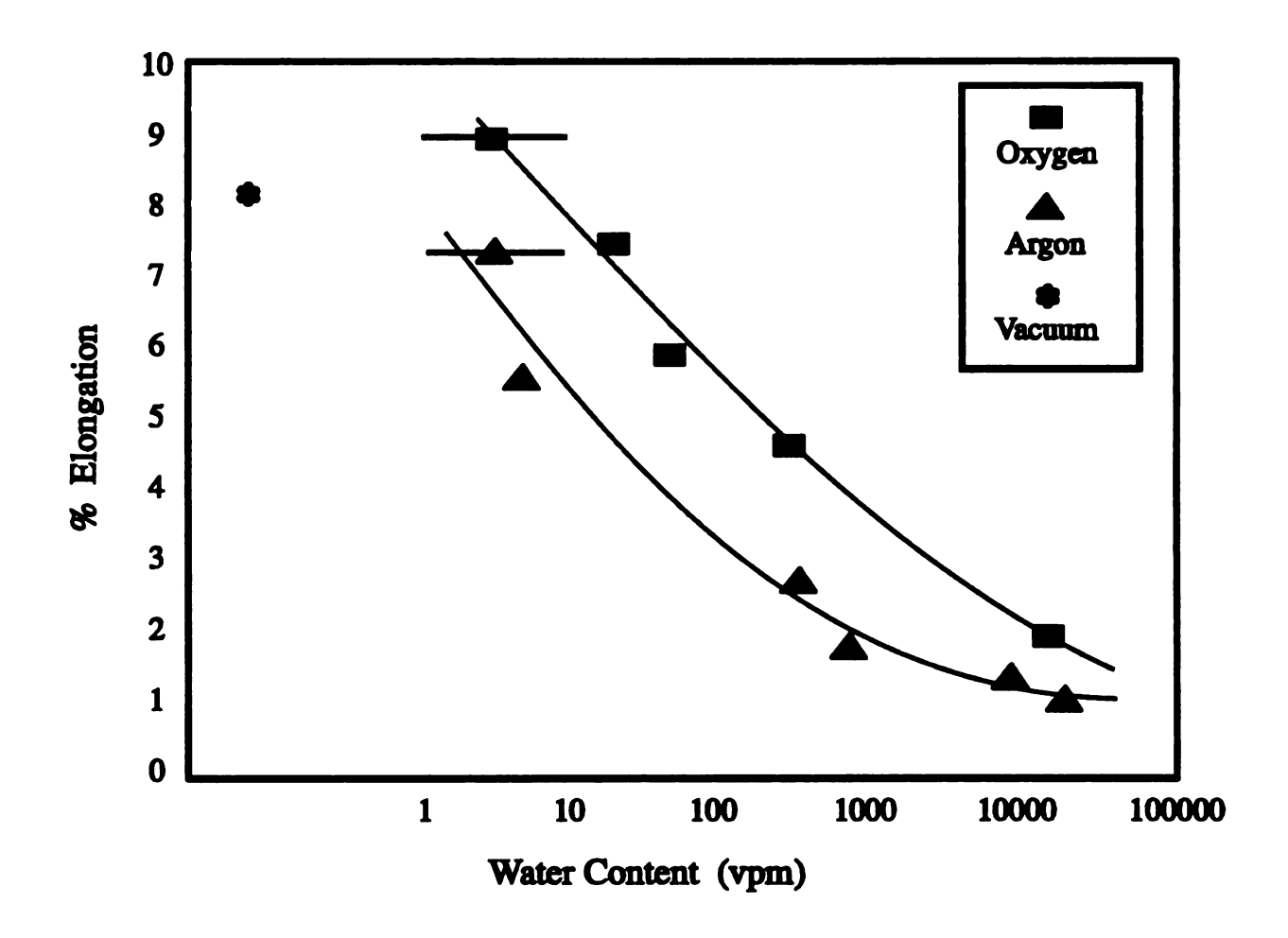


Figure 18

Percent elongation of Fe-35Al in oxygen and Fe-33Al in argon. Adapted from [53]

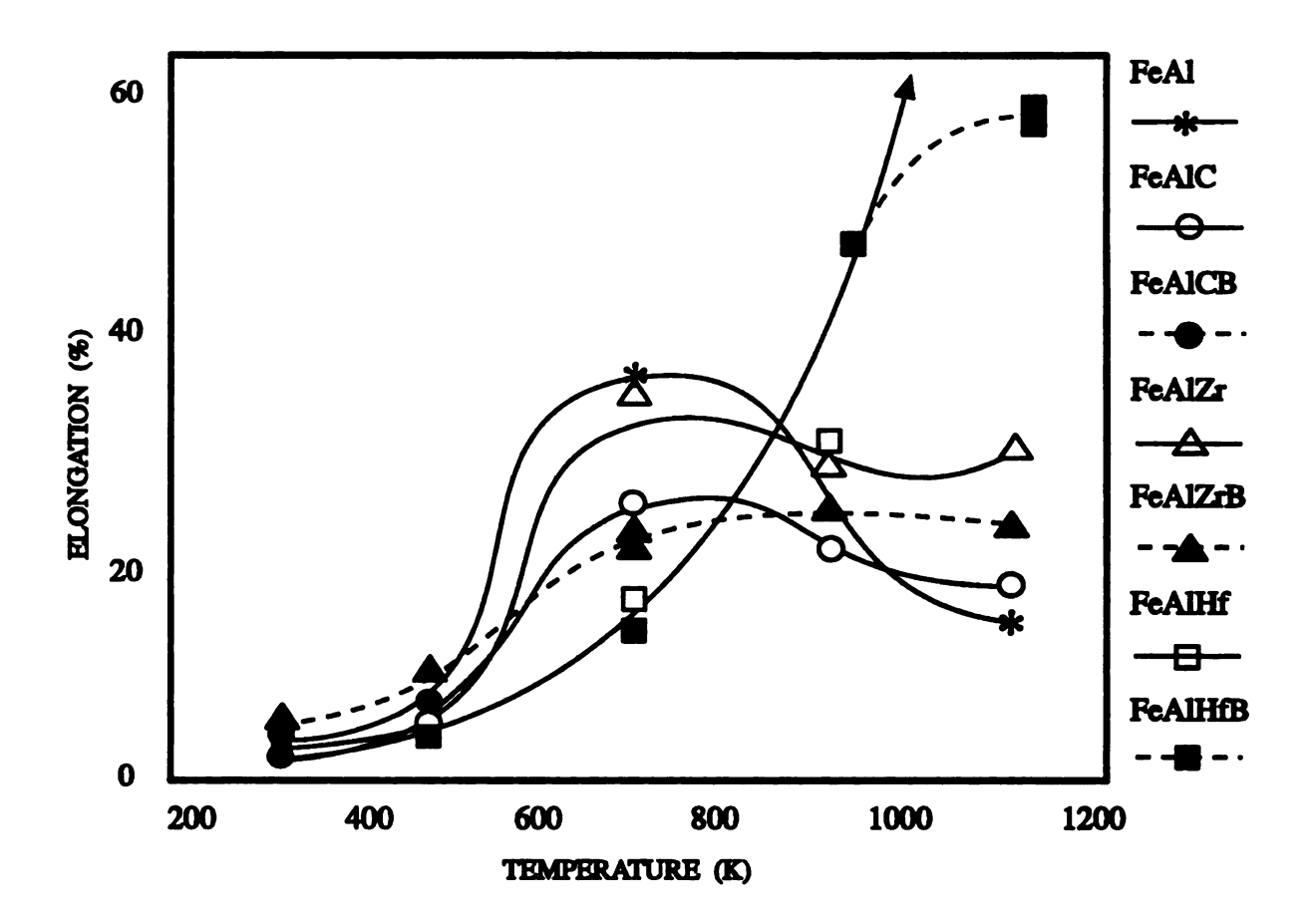


Figure 19
Percent elongation vs. temperature for FeAl and FeAl with ternary additions of C, Zr, Hf, and B. Adapted from [53]

investigation [52]. This investigation concentrated on elements traditionally known to strengthen grain boundaries (i.e. C, Zr and Hf added with and without boron). Additions of C and Zr were found to generally reduce ductility. However, the addition of boron to C and Zr alloys restored ductility to approximately 5%.

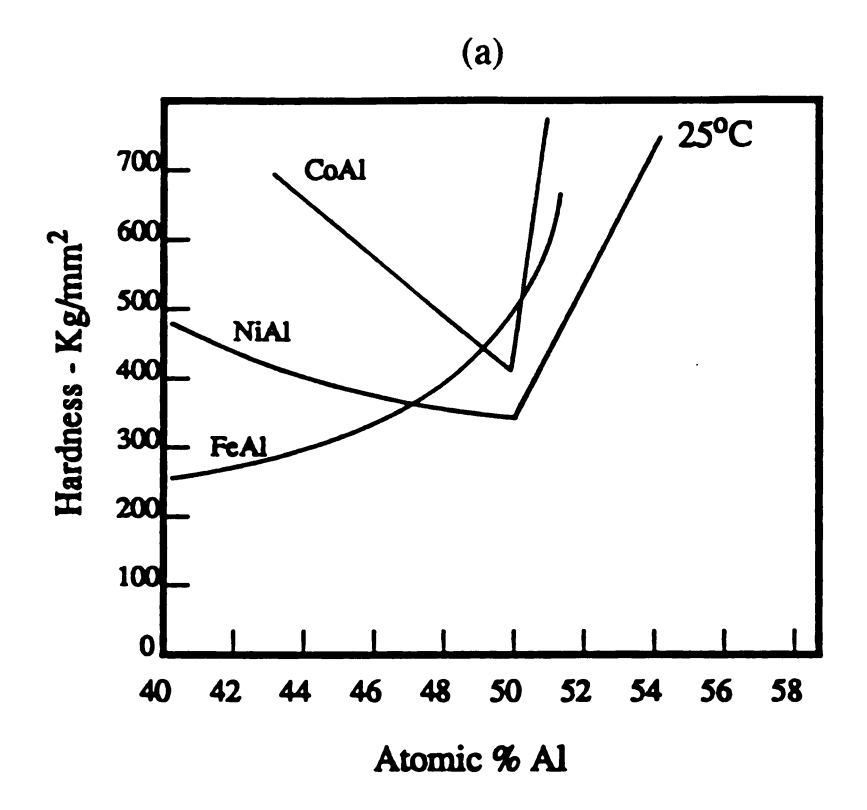
### 1.4.2 Mechanical Properties As a Function of Stiochiometry and Thermal History

Additional factors that appear to have a signifigant effect on the tensile behavior of FeAl are alloy stoichiometry and thermal history. With respect to the issue of stoichiometry, room temperature tensile studies [18, 19, 25] show that Fe-50Al always fails in a brittle manner, while Fe-40Al displays some ductility. Concurrently, FeAl has been shown to have the highest hardness near stoichiometry, followed by decreasing hardness with increasing iron rich deviations from stoichiometry [53]. Conversely, a study by Westbrook [53] found B2 NiAl and CoAl had their lowest hardnesses at stoichiometry and that both alloys increased in hardness above and below stoichiometry. Hardness behaviors of FeAl, NiAl and CoAl can be seen in figure 20(a) and 20(b) for 25°C and 500°C respectively.

Although all of these materials generally weaken with temperature, the hardness versus stoichiometry behaviors hold true from 25°C to 600°C for FeAl and to 800°C for NiAl and CoAl.

#### 1.4.3 Thermal History and Vacancy Concentration Effects

Recall that FeAl has been shown to have high quenched-in vacancy concentrations [10-13]. Corresponding increases in hardness with increasing cooling rate have been attributed to the number of retained vacancies [10, 16]. For example, studies on polycrystalline FeAl [10, 16-19, 25] have provided sufficient evidence to conclude that there is a strong relationship between increases in hardness, increases in yield strength and decreases in tensile elongation with increasing vacancy concentration. Figure 21 displays the effect of cooling rate [19] on the tensile stress-



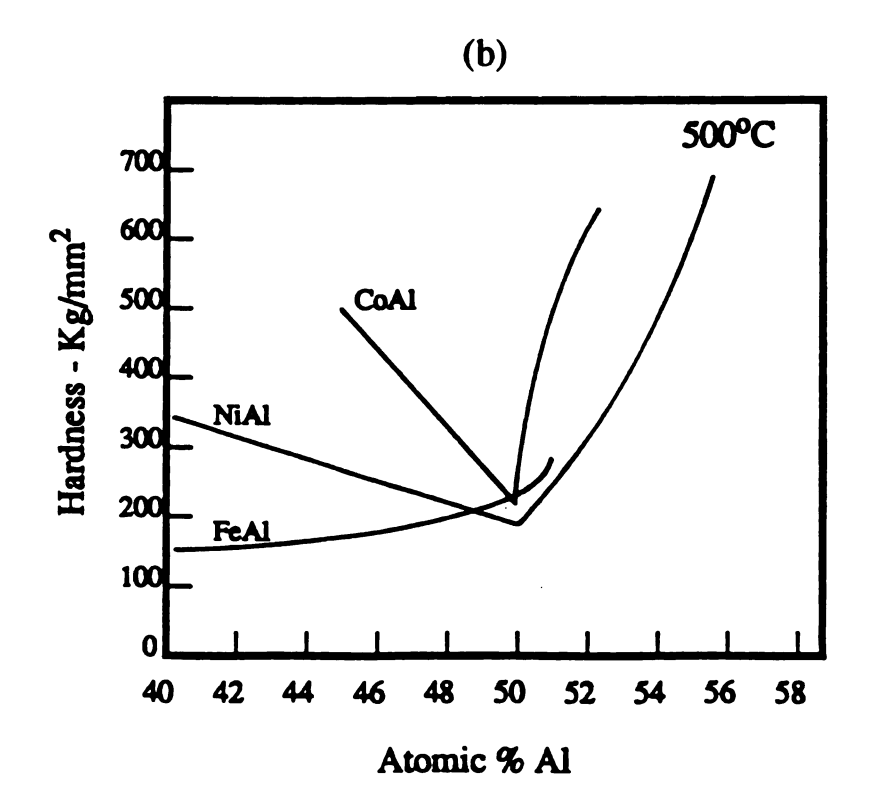


Figure 20
Hardness vs. at% Al isotherns for FeAl at (a) 25°C (b) 500°C.
Adapted from [52]

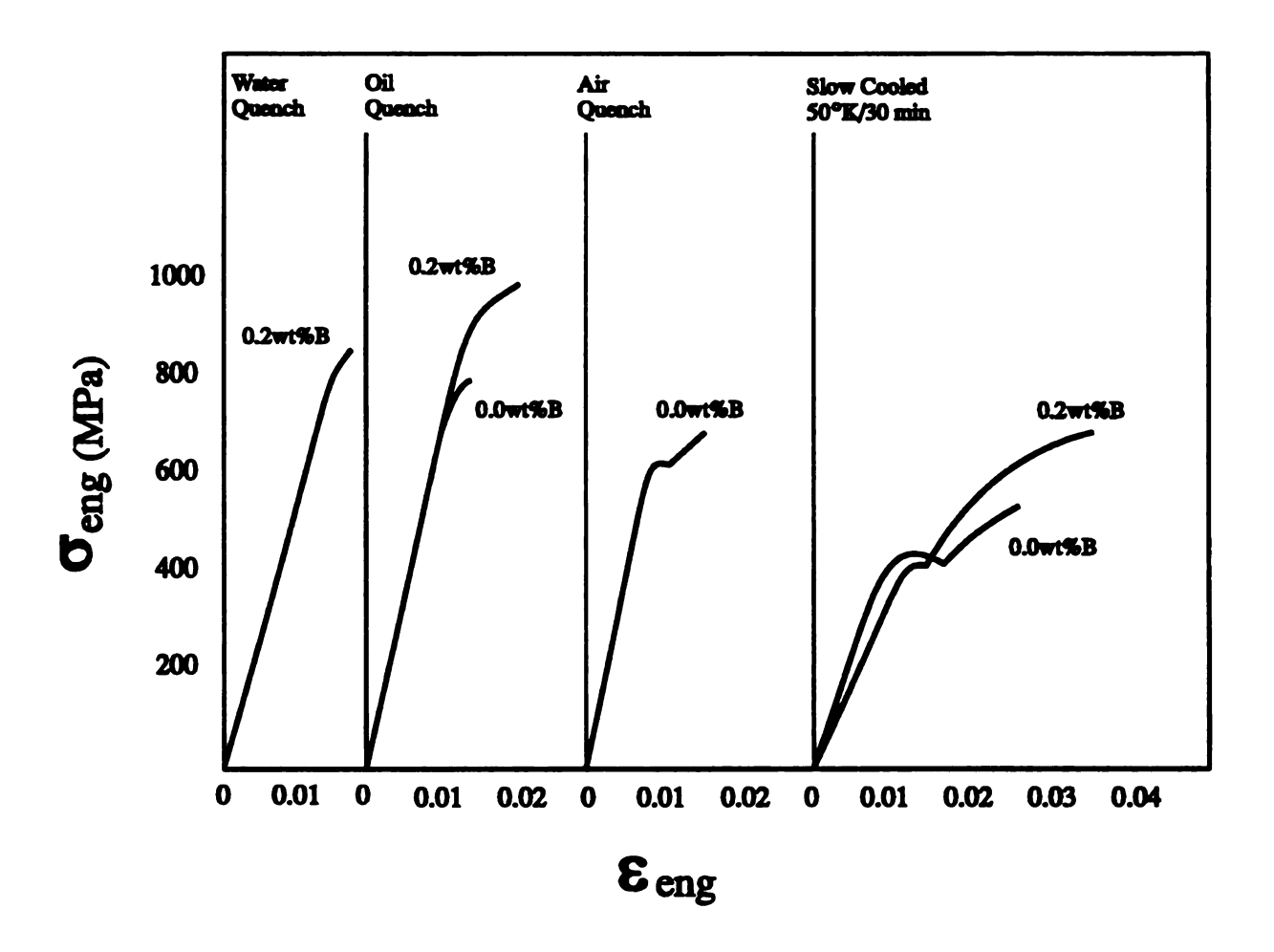


Figure 21

Engineering stress-strain curves for polycrystalline Fe-40Al subjected to different cooling rates, with and without the addition of 0.2 wt.% boron. Adapted from [18]

strain behavior of polycrystalline Fe-40Al (with and without the addition of 0.2 wt% boron). Similarly, compression tests of single crystal samples [17] have displayed similar increases in yield strength with increasing cooling rate, following homogenization.

Complementing these studies, Nagpal and Baker [54] studied the effect of cooling rate on the hardness of FeAl. They annealed microhardness discs (of 34, 40, 45, 50 and 51 at.% Al) and then air-cooled, furnace-cooled and water-quenched the disks. Their findings include: (1) A 673K anneal of samples slow cooled (50K/hr) from 1273K reduced their hardness even further. For example, the hardness of water cooled Fe-45Al was reduced 80% after annealing at 673K. (2) Air cooled samples of all compositions (except for Fe-51Al) had similar hardness values to water-quenched counterparts. (3) Alloys having increasing aluminum contents (up to 50 at.% Al) showed increasing differences in hardness between furnace-cooled and air-cooled counterparts. This is consistent with earlier work which found that vacancies increase with increasing aluminum content [13,25]. (4) Microhardness data shows that (in the annealed samples where non-equilibrium vacancies have presumably been removed) increasing aluminum content from 34% to 45 at.% Al produced little increase in strength.

## 1.4.4 Combined Effects of Thermal History and Testing Environment

Gaydosh et al. [55] studied the effects of combining different testing environments (air, oxygen, nitrogen and vacuum) with different quenching rates on Fe-40Al, Fe-40Al-0.5B and Fe-50Al samples. Gaydosh et al. [55] tensile tested the as extruded material (cooled from 1250K at a rate of 600K/hr) and a heat treated version which was annealed at 1100K for 2 hours and then slow cooled. They found that (1) the as-extruded material had higher strength and lower ductility than the annealed material; (2) slow cooling of the boron-doped alloy lowered its yield strength signifigantly but did not appreciably increase its ductility; and (3) the

brittleness of Fe-50Al in the inert environments indicated that other intrinsic factors were responsible for its lack of ductility.

Further studies focused on testing atmosphere and optimization of annealing temperatures and annealing times. Studies by Lynch et al. [56] examined polycrystalline Fe-36Al specimens which were heat treated at 1073K for 1 hour. It was believed that the cooling rate from the annealing temperature was fast enough to quench in most of the excess thermal vacancies. The specimens were then annealed at various temperatures and times. Testing took place in oxygen and air atmospheres at 298K. There was no mention of moisture content. Table 5 illustrates the results of their tests. Observing table 5, one sees that the best elongations were obtained by the 873K anneals. Figure 22 illustrates the corresponding precent elongation versus annealing temperature for oxygen and air environments. Corresponding tensile tests of yield strength and hardness (shown in figures 23 and 24 respectively) increased with increasing annealing temperature, while the strain hardening coefficient decreased (see figure 25).

Based on the aforementioned research, it is clear that the mechanical properties of B2 FeAl are strongly dependent on annealing temperature and vacancy concentration. Lynch and Heldt's study, [56] observed the yield strength and strain hardening coefficient to change by factors of two, depending on thermal treatment. Room temperature tensile ductility increased considerably in dry oxygen and air after annealing at low temperatures. Also, it should be noted that the ductility in both air and oxygen decreased with increasing annealing tempreature, [56] suggesting that excess vacancies affect the intrinsic ductility of FeAl rather than a susceptibility to environmental embrittlement.

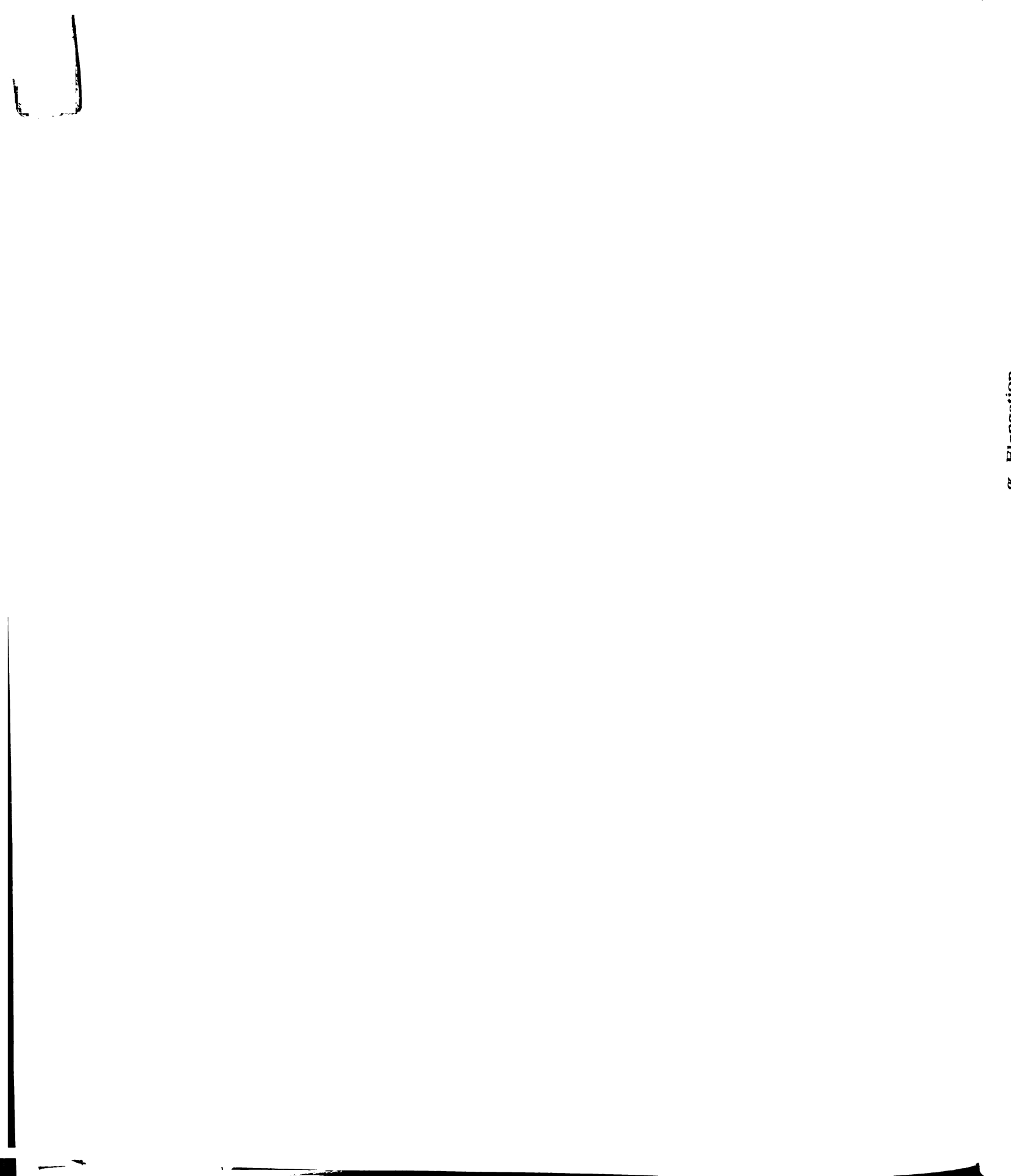
# 1.5 Vacancy Behavior in B2 FeAl

Although vacancies are known to be responsible for hardening and strengthening in B2 FeAl, the exact mechanisms by which they accomplish this

Table 5. Mechanical Properties of Fe-36Al after annealing at Various Temperatures [56].

Annealing* Treatment	Testing Environ	% Elongation	Yield Strength (MPa)	UTS (MPa)
673K-2hr	oxygen	12.1	390	796
673K-60hr	oxygen	13.0	257	700
673K-100hr 673K-100hr	oxygen air	13.2 3.1	243 243	701 369
873K-1hr 873K-1hr	oxygen air	14.8 3.0	282 279	742 401
873K-19hr	oxygen	14.5	290	751
973K-1hr 973K-1hr	oxygen air	12.0 1.3	345 378	740 427
1073K-1hr 1073K-1hr	oxygen air	9.5 0.86	436 481	765 519
1273K-1hr	oxygen	10.2	500	825

<sup>\*</sup> All specimens were heat treated at 1073K for 1 hour prior to annealing.



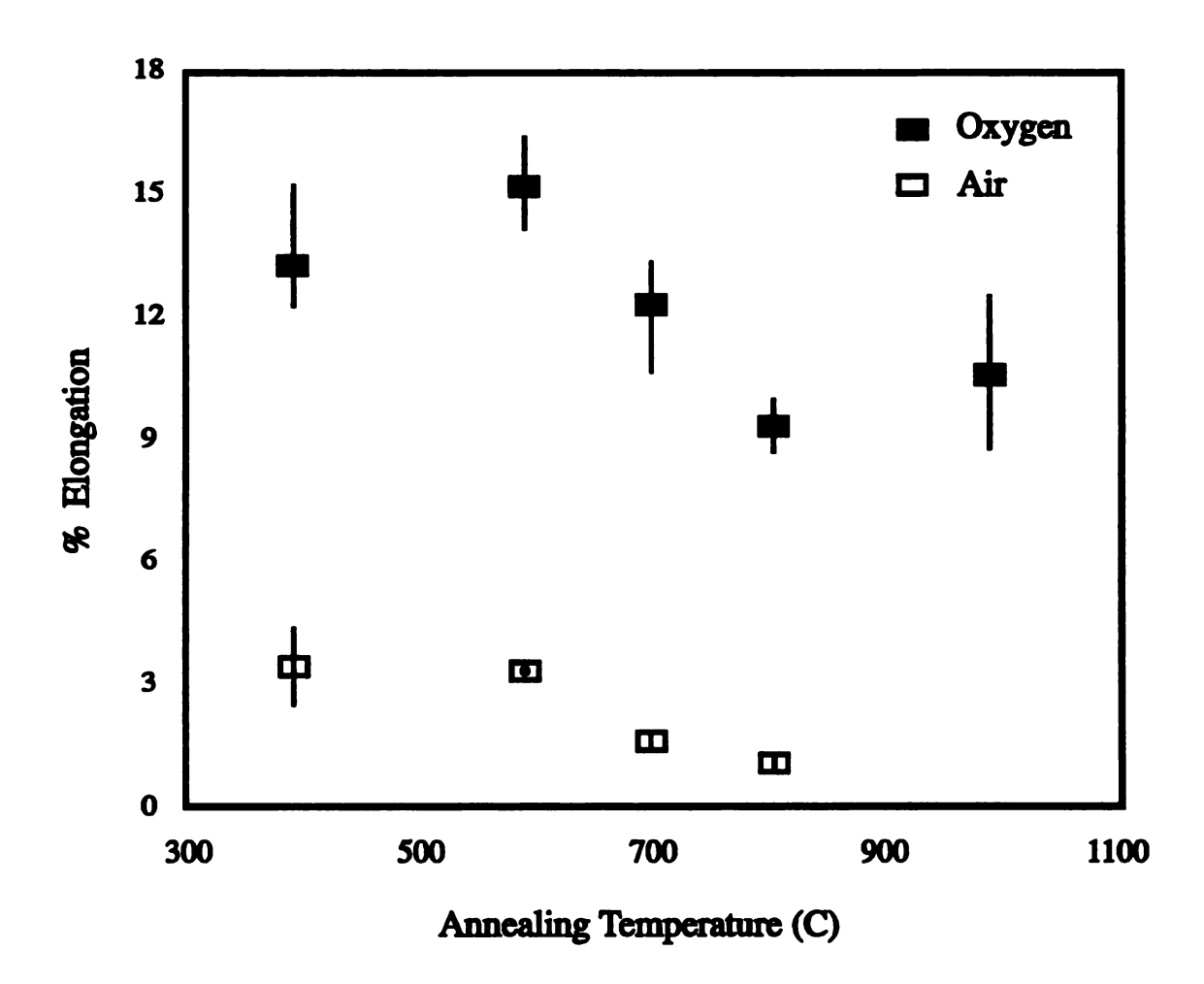


Figure 22

Percent elongation vs. annealing temperature for Fe-36Al samples heat treated at 1073K prior to annealing and then tested in oxygen and air. Adapted from [56]

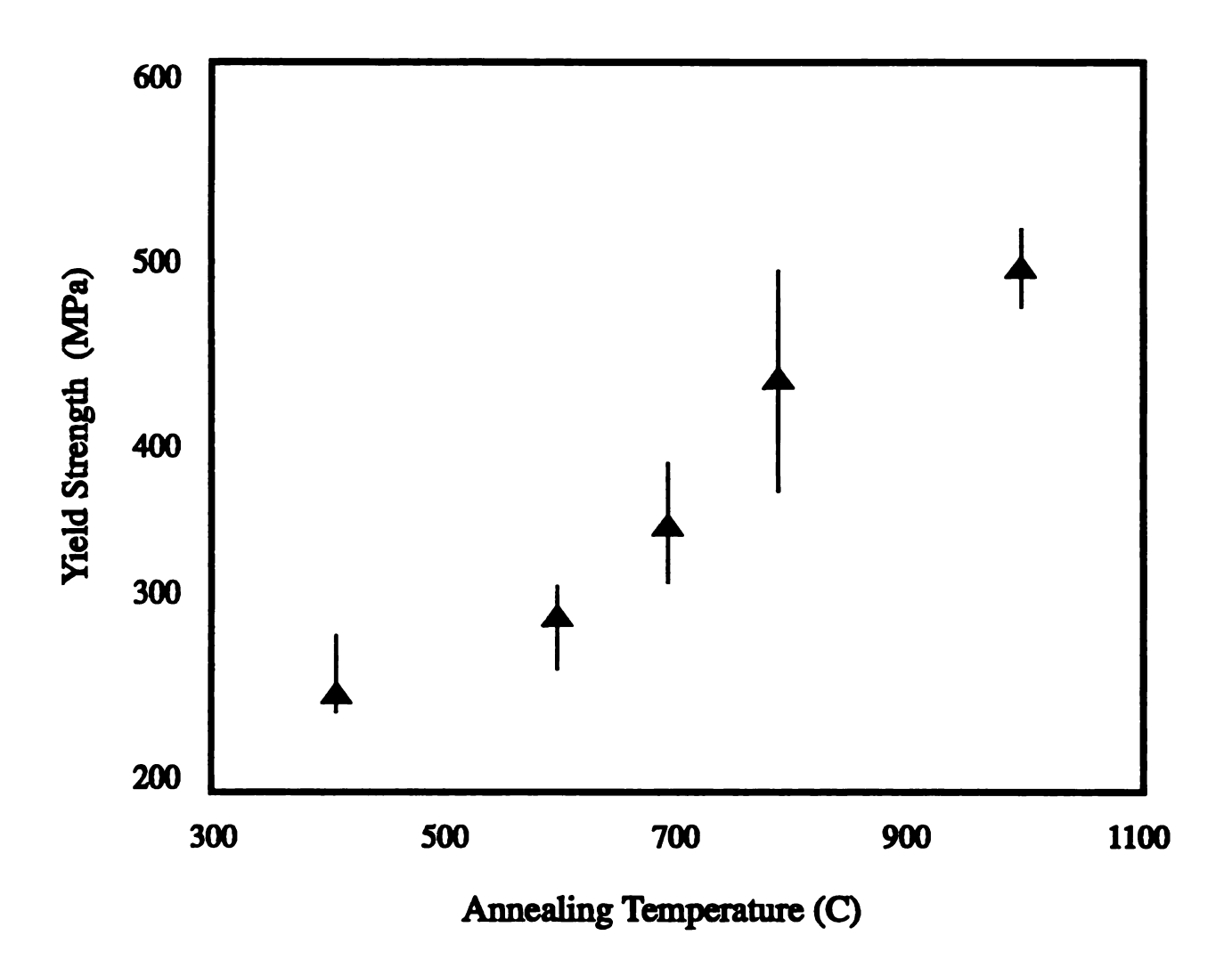


Figure 23
Yield strength vs. annealing temperature for polycrystalline Fe-36Al heat treated at 1073K prior to annealing. Adapted from [56]

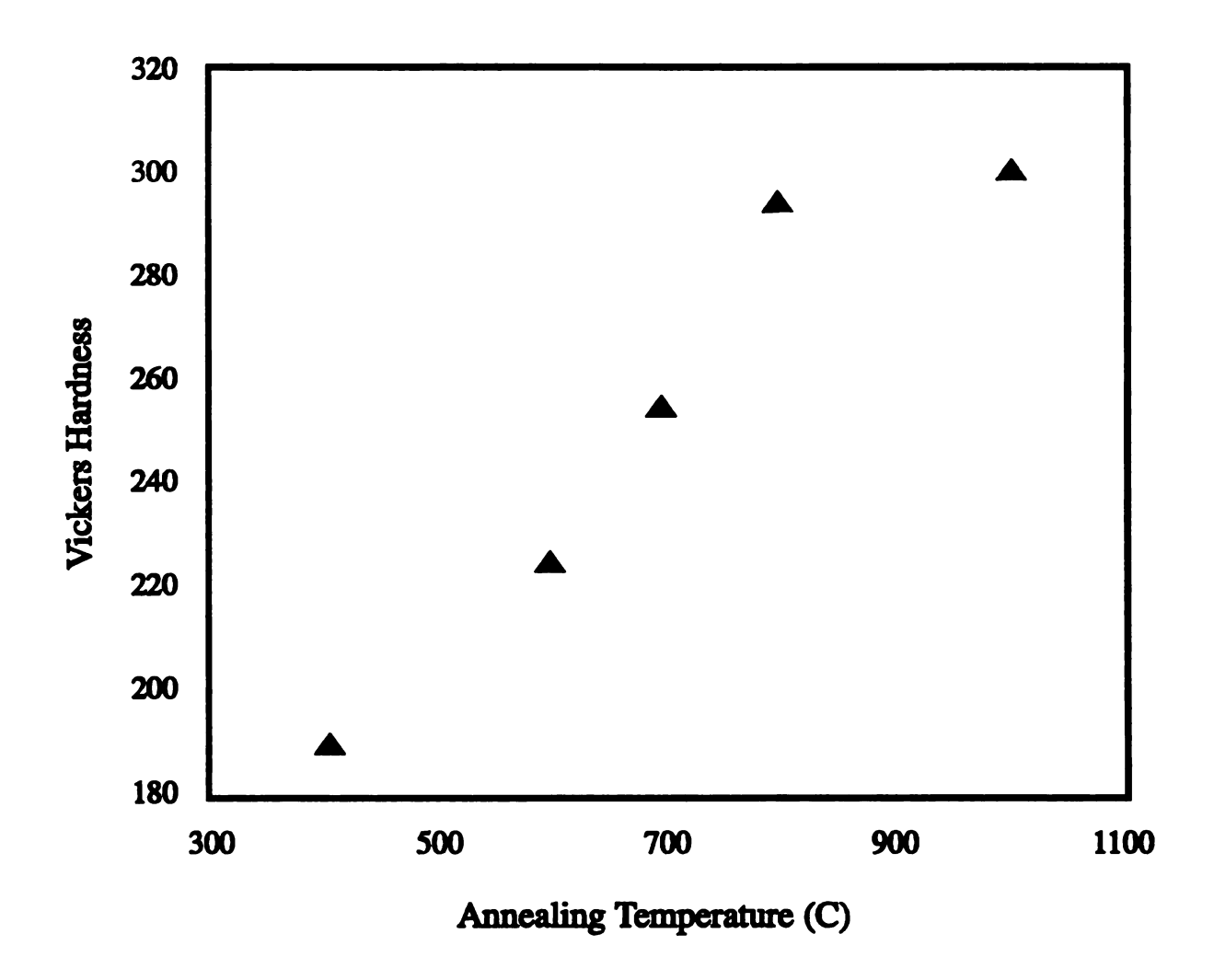


Figure 24

Hardness vs. annealing temperature for polycrystalline Fe-36Al heat treated at 1073K prior to annealing. Adapted from [56]

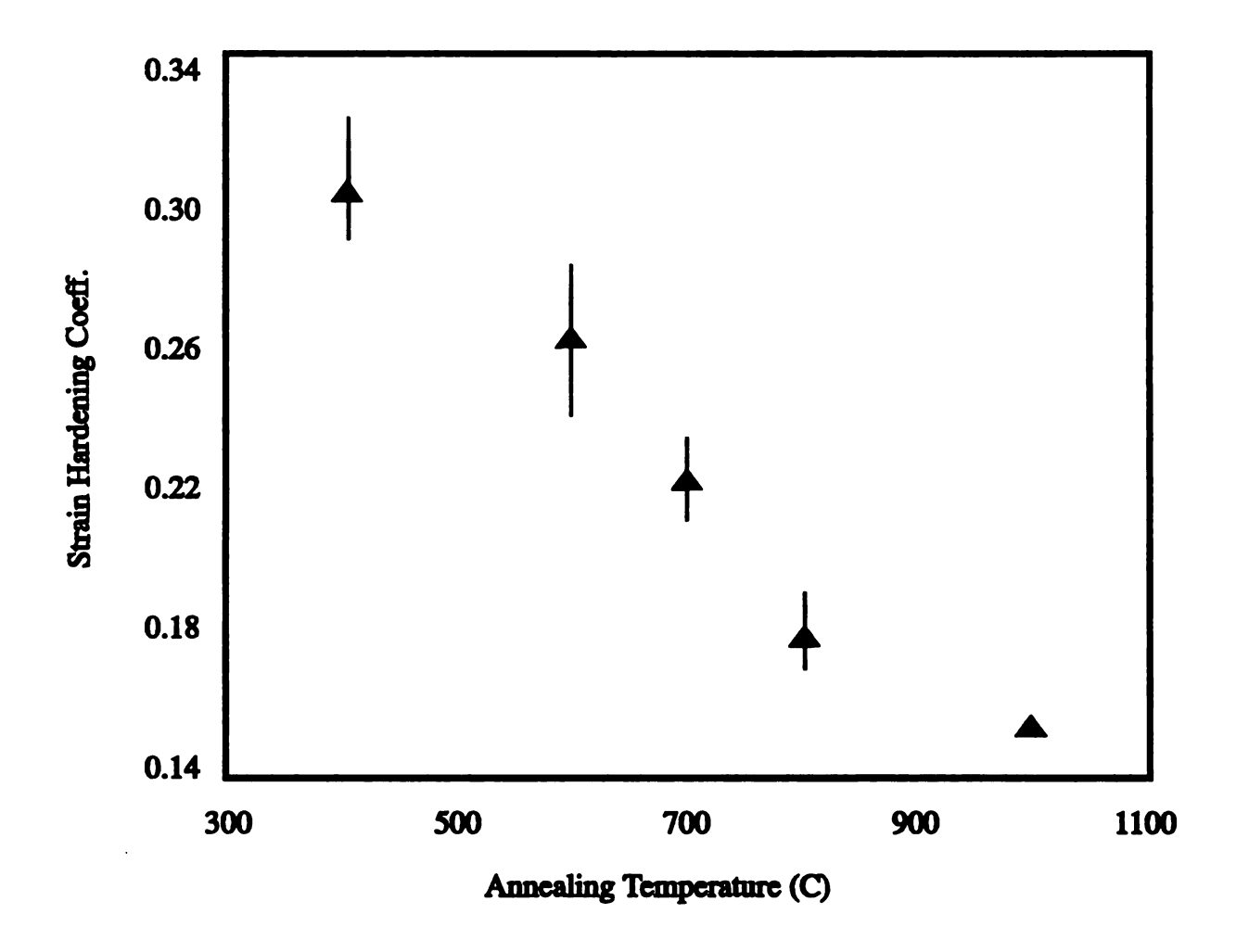


Figure 25
Strain hardening coefficient vs. annealing temperature for polycrystalline Fe-36Al heat treated at 1073K prior to annealing. Adapted from [56]

remain unclear. It has been hypothesized that vacancies may act as point defect strengtheners (pin dislocations), change the degree of long range order (APB energy) and/or coalesce to form material strengthening jogs on existing dislocations [57-59]. Chang et al. [57] correlated vacancy changes in FeAl with hardness changes in a manner similar to point-defect strengthening. Analogous with point defect strengthening models (i.e. solid-solution strengthening), it was found that hardness increased with the square root of the vacancy concentration. Stoloff et al. [58] found that vacancies changed the degree of long range order (APB energy) in intermetallic FeCo-V and Fe<sub>3</sub>Al alloys. They found that variations in the degree of long range order caused large changes in yield stress for the alloys tested. Kimura et al. [59] proposed that vacancies annihilate and/or form clusters on existing dislocations, which in turn result in material strengthening jogs.

In-situ annealing studies, using transmission electron microscopy, have shown that excess vacancies in B2 FeAl anneal out into dislocation loops, helices, super-structure dislocation loops and paired helices bounding APBs [60-62]. Fordeux et al. [61] concluded that these vacancy/dislocation products form because homogeneous vacancy coalescence into voids is difficult in materials which posess a strong tendency for ordering. TEM (g•b = 0) analyses determined that the vacancy formed dislocation configurations had Burgers vectors of <111> (scarce observation) or <100> [60,61]. Junqua et al. observed that the dislocation loops nucleated on "grown in" dislocation lines within 45 minutes at 673K [60]. Interestingly, it was observed that a [010] dislocation which was encumbered with a vacancy formed helix, dissociated into two 1/2<111> partials [61]. These vacancy products were observed to nucleate on inclusions and preexisting (grown in) dislocations. It is interesting to note that the previously discussed annealing studies [54-56] would seem to imply that there is a decrease in hardness and yield strength associated with the formation of these vacancy/dislocation defect structures.

46

### 1.6 Objective

All of the investigations involving heat treatment, quenching rate, adjustment of the testing atmosphere, deviations from stoichiometry and alloying additions have shown that the mechanical properties of FeAI may be affected signifigantly by these variables. However, regardless of these factors, the flow and fracture properties of B2 FeAI are inextricably tied to dislocation movement, which is in turn regulated by dislocation core structure. Therefore, it is imperative to try to gain a better understanding of the mechanical behavior of this material by examining observable dislocation cores. Unfortunately, technological constraints begin to play a role in which types of dislocation cores one can image.

The present study uses high resolution electron microscopy (HREM) to examine dislocation cores in two compositions of single crystal B2 FeAl. However, due to HREM imaging constraints (discussed in section 2.8), it is advantageous to study <100> dislocations and a temperature was selected based Yamaguchi and Umakoshi's work [28,29] which was belived to be high enough to activate <100> dislocations during compressive deformation. An advantage of choosing <100> dislocations is that it allows comparison with the <100> core structures observed in NiAl and CoAl. Hopefully, these comparisons may lead to a better understanding of the active slip systems and mechanical response of B2 aluminides as a whole.

Since it is not possible to cover all avenues of investigation, analyses will be restricted to rationalizing the differences in mechanical properties, between the two FeAl alloys along with NiAl and CoAl. This analysis will be based on the observed differences between the dislocation core structures. It is hoped that increased knowledge, gained by analyzing these dislocation cores, will provide better insight into the previously mentioned B2 aluminides. In addition, an attempt to explain the effect that vacancy/dislocation interactions have on the mechanical properties of B2 FeAl will be presented. This will be rationalized based on the observed dislocation

configurations and core configurations. Until technological improvements can be made in the atomic analysis of materials, it is hoped that the study of resolveable cores will enable one to gain better insight into FeAl's weaknesses. Hopefully, this information will enable the improvement of B2 alloys in general, allowing one to take full advantage of attractive properties that this class of materials posess.

#### 2. Experimental Procedure

#### 2.1 Material

The single crystal materials used in this study were obtained from two different sources. First, a material with the nominal composition of Fe-50Al was available from a previous study [25]. It came in the form of a rectangular casting approximately 25mm x 5mm x 10mm. The casting was directionally solidified and contained approximately thirty grains. The grains ranged in diameter from 2.5mm to 5mm (along the length of the casting). Most grains were large enough to section single crystal specimens from them. Fe-40Al single crystal specimens were obtained from the NASA Lewis Research Center, Brookpark Ohio. The crystals were grown by the Bridgeman method. The Fe-40Al crystals arrived in the form of centerless ground tensile specimens approximately 10mm long and having 1.3mm diameter grip sections. The specimens were cut from the grip sections. Table 6 lists the chemical makeup of each composition.

## 2.2 Compression Sample Preparation

A high speed Struers Accutom saw with a Buehler iso-cut diamond wafering blade was used to fashion rectangular compression samples. The sample dimensions were kept near 9mm x 3mm x 3mm. A 3:1 height to width ratio was used in order to promote homogenous deformation of the specimens. It should be noted that material constraints limited the orientation of the specimens to a certain extent. Once each sample was fashioned, a record was kept of each samples dimensions. This helped to identify each sample after deformation and helped with verification of plastic strain following compression. After the Fe-50Al specimens were cut to the proper dimensions, they were etched in order to verify that they were made up of a single crystal. This was done by hand grinding the specimens with 600 grit SiC emmery cloth, polishing with 1µm diamond paste and etching in a 100 parts H<sub>2</sub>O, 20 parts HNO<sub>3</sub>, 3 parts Hf and 2 parts HCl solution for six seconds. Following sample

<u>Table 6</u> <u>Chemical compositions of Fe- 50Al and Fe-40Al</u>

Fe-50Al	Al (wt%)	O (wt%)	P (wt%)		Fe (wt%)
	31.6(48.8at%)	0.008	0.004		balance
Fe-40Al	Al (wt%)	O (wt%)	C (wt%)	S (wt%)	Fe (wt%)
	23.8(39.6at%)	0.0031	0.0046	0.0015	balance

fashioning and single crystal verification, one corner of each specimen was notched as illustrated in figure 26. Notching allows one to preserve the exact crystallographic orientation of the specimen, assisting with crystallographic analyses following deformation. The notch was always oriented to the upper right hand corner, when constructing stereographic projections.

#### 2.3 Heat Treatment

All samples received a 24 hour heat treatment under vacuum at 1273K. The samples were slow cooled from this temperature at a rate of 100K/hr down to 500K. Then the samples were furnace cooled from 500K down to room temperature. This was done in order to minimize vacancy concentrations and instill identical thermal histories in both materials.

# 2.4 Crystallographic Orientation

Orientation determination, by the Back Reflection Laue technique, indicated that the compression axes of all the samples were within 15° of [100]. Figures 27(a) and (b) show standard stereographic unit triangles with typical compression axis orientations for Fe-40Al and Fe-50Al respectively. Unfortunately, it was not possible to obtain orientations further away from [100] due to the aforementioned material constraints. Back Reflection Laue was performed using an accelerating voltage of 23Kv, a 32mA current, a V foil filter, a Cu X-ray tube and an exposure time of 7 min on type 52 polaroid film. The notched end had to be polished with 1µm diamond paste in order to get a good exposure. Using the back reflection photos, stereographic projections were produced. These projections were used to determine activated slip planes following compression.

#### 2.5 Sample Compression

Once crystallographic orientations were determined, samples underwent compression to approximately 5% plastic deformation at 873K (.67  $T_m$ ) under vacuum. Plastic strain was set at 5% in order to keep the number of dislocations low

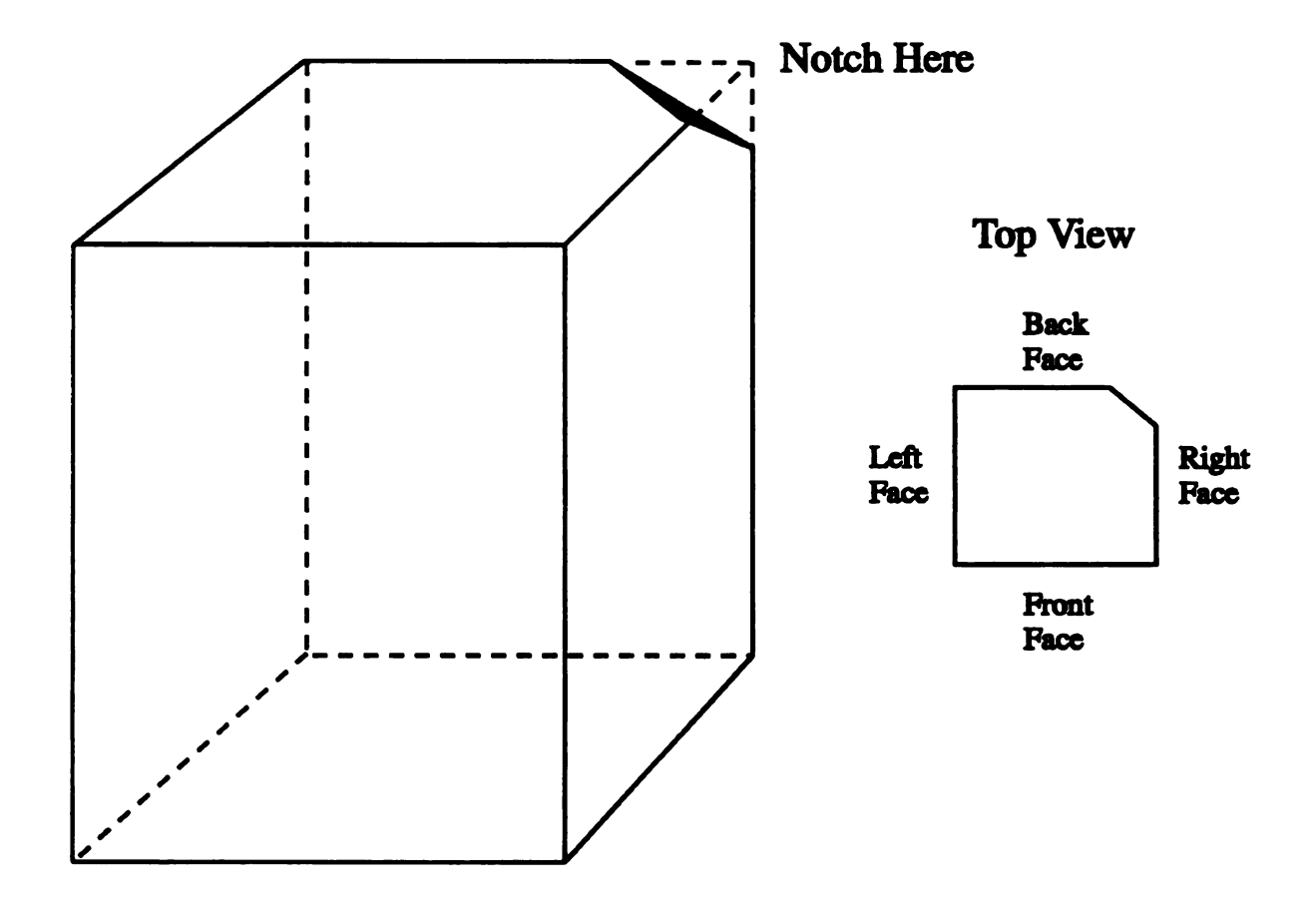


Figure 26

Rectangular compression specimen showing the orientation convention used throughout the analysis.

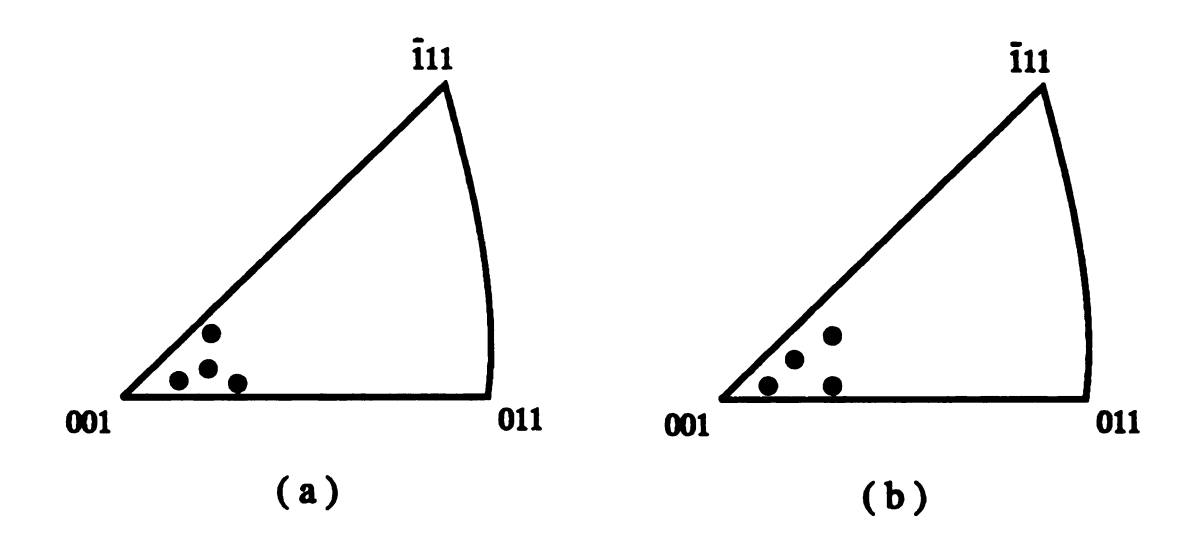


Figure 27
Typical compression axes orientations for (a) Fe-40Al and (b) Fe-50Al.

enough to prevent them from being involved in too many reactions with each other.

Compression was performed using an MTS<sup>TM</sup> 810 axial-loading test apparatus equipped with a Centor<sup>TM</sup> vacuum furnace. A nominal strain rate of 2.4 x 10<sup>-4</sup> s<sup>-1</sup> was used for all specimens. All specimens (both alloys) were furnace cooled following release of the deformation load. This cooling took approximately 2 hours.

### **2.6 Slip Trace Analysis**

Following compression, slip lines were optically recorded on type 55 Polaroid film, using a Leco Neophot 21<sup>TM</sup> polarized-light microscope. The clear polarization filter was used along with a 5 second exposure time. The angles of the slip lines on two non-parallel crystal faces were measured and used to determine the active slip plane via a standard two-face analysis.

### 2.7 Thin Foil Preparation

Compressed samples were sectioned parallel to either the observed slip plane {110}, or parallel to {001} planes lying perpendicular to the [100] pole (the approximate deformation axis). This was accomplished by re-mounting the compressed specimens on a goiniometer and using the Back Reflection x-Ray technique to zero in on the desired pole. Once reorienting a sample was accomplished, the goiniometer-sample assembly was installed (duplicating the same orientation) in an EDM (electro discharge machine) and thin sections were sliced for TEM/HREM study.

Sections 0.5mm thick were cut using a Materials Science Spark Erosion Unit. Set R, Set V, Set C and Auto Drive were all set at position two. Faster cutting speeds or increases in the other settings resulted in wire breakage. Following sectioning, standard 3mm disks were cut from the slices using the Spark Erosion Unit equipped with a 3mm inside diameter brass tube. During disk preparation, all settings could be placed on position four.

54

While mounting sections for disking, it was very important to make sure that there was good electrical contact between the sample section and the metal mount. This was best accomplished by applying a small drop of Super Glue to the metal mount, placing the FeAl section on the drop and while applying pressure, swabbing away the excess glue with a cotton swab impregnated with acetone.

Once the disks were cut, they were mechanically thinned using a specially designed jig. The jig was made up of a section of 1in dia. steel bar stock threaded with a 3mm dia. fine thread screw (see figure 28). This allowed the disk's thickness to be held constant during thinning. Using the jig, disks were thinned (using 320 grit and then 600 grit SiC emmery cloth) down to approximately 0.10mm.

Final disk thinning, (creating transmission and high resolution electron microscopy foils) was performed using a Struers Tenupol<sup>TM</sup> twin jet electropolishing cell equipped with a Polypower<sup>TM</sup> power supply. The disks were thinnned into foils using an electrolyte composed of 30% HNO<sub>3</sub> in methanol. The solution was chilled to 253K by adding liquid nitrogen to the solution. The voltage was set at 12V and the thinning speed was set at position four.

#### 2.8 Transmission and High Resolution Electron Microscopy

Conventional transmission electron microscopy (TEM) was used to characterize dislocations using the  $\mathbf{g} \cdot \mathbf{b} = 0$  and  $\mathbf{g} \cdot \mathbf{b} \times \mathbf{u} = 0$  criteria. The analyses were performed using brightfield imaging in a Hitachi H-800 TEM equipped with a double-tilt specimen holder and opperated at 200kV.

High Resolution Electron Microscopy (HREM) was used to perform phase contrast imaging of dislocation cores with line directions lying partially or completely orthogonal to [100] or [010] planes. HREM was performed at the University of Michigan, using a JOEL 4000EX opperated at 350kV. The HREM images were digitally scanned and compressed to aid in viewing core features. HREM simulations of the Fe-50Al dislocation core was based on a theoretical core

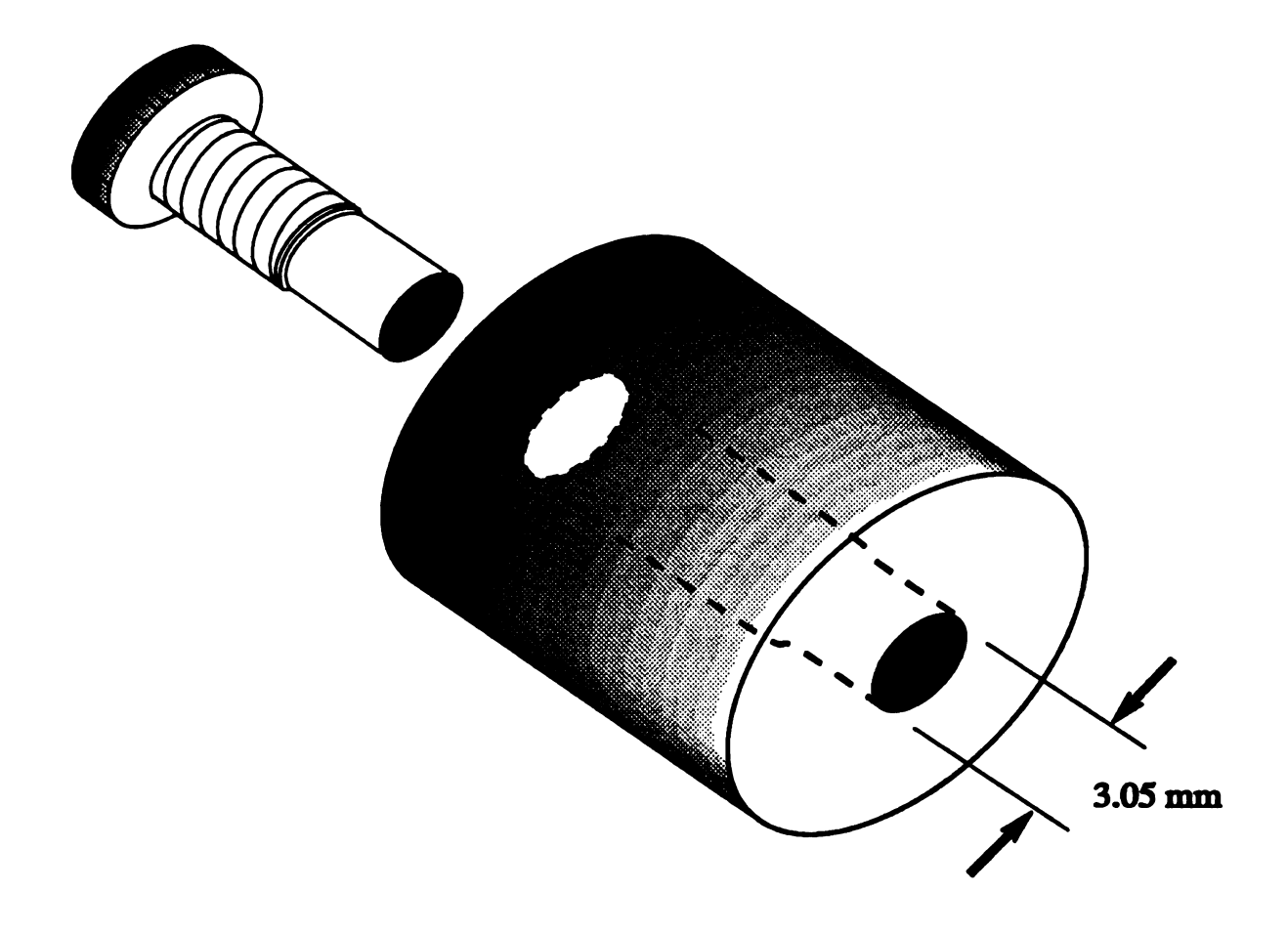


Figure 28

Disk thinning jig used to prepare TEM and HREM foils.

56

structure determined by Vailhe and Farkas, [63]. This was accomplished using the embedded atom method. The simulated images were created using the EMS software package [64].

It should be noted that while the core structure of <111> screw dislocations are of keen interest, technological limitations in the High Resolution Microscopy technique make it impossible to completely image cores which do not have all atomic displacements lying in a plane orthogonal to the beam of the microscope. In order for atomic resolution of a dislocation core to take place, the core must be imaged end on. In other words, the dislocation line direction must be parallel with the beam of the microscope. In addition, the dislocation core needs to have planar distortions (atomic displacements) perpendicular to the microscope's beam. This means that pure edge dislocations have the only type of core which can be fully resolved. Since <111> screw dislocations have atomic displacements which lie parallel to their line directions, they can not be resolved. However, if the dislocation is mixed, having both edge and screw character, the edge components can be resolved. Finally, the resolution limit of the microscope is approximately 1.7Å [5]. Therefore, in order to assure point to point resolution of the atoms, it is important to image dislocation cores with line directions perpendicular to low index planes (i.e. {100}).

### 3. Experimental Results

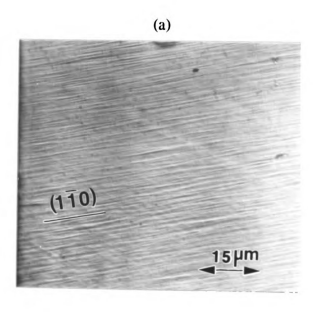
# 3.1 Slip Characterization

The deformed Fe-40Al and Fe-50Al single crystal compression samples (8 of each) typically displayed well defined slip lines. Figure 29(a) and (b) are optical micrographs which display the slip bands on two adjacent faces of an Fe-40Al specimen. The slip lines appear to be a little wavy, indicating some cross-slip may have taken place. In one case, an Fe-50Al specimen displayed two sets of lines, indicative of duplex-slip. The specimen with two sets of slip lines (figures 30(a) and (b)) was oriented close to the [100]-[110] border of the unit triangle. This finding is in agreement observations made by Crimp [25]. Two specimens oriented close to [100] and lying on [100]-[110] and [100]-[111] unit triangle borders, displayed no slip lines following compression. This was expected since orientations close to [100] may have as many as 4 different slip systems activated, causing the slip lines to be obliterated [25].

Slip planes were determined by measuring the angles of the slip lines on two non-parallel crystal faces. The compliments of the measured angles are plotted as great circle traces on their stereographic projections. The intersection of the traces reveals the activated slip plane or planes. An illustration of a standard two-face slip plane determination can be seen in figure 31.

A single Fe-50Al sample was observed to exhibit two sets of slip lines, indicating two active {011} type slip planes. All other analyses, for both Fe-50Al and Fe-40Al, revealed a single active slip plane of the {110} type.

Surprisingly, TEM analysis (using the **b** x  $\mathbf{u}$  = slip plane criterion) revealed the slip planes to be {100} types. This observation might indicate that there is not a <111> to <100> slip transition in FeAl, as reported by others [28-30]. Instead, it might be possible that the material cooled slowly enough to allow the dislocations to



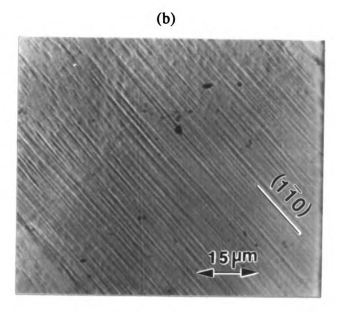
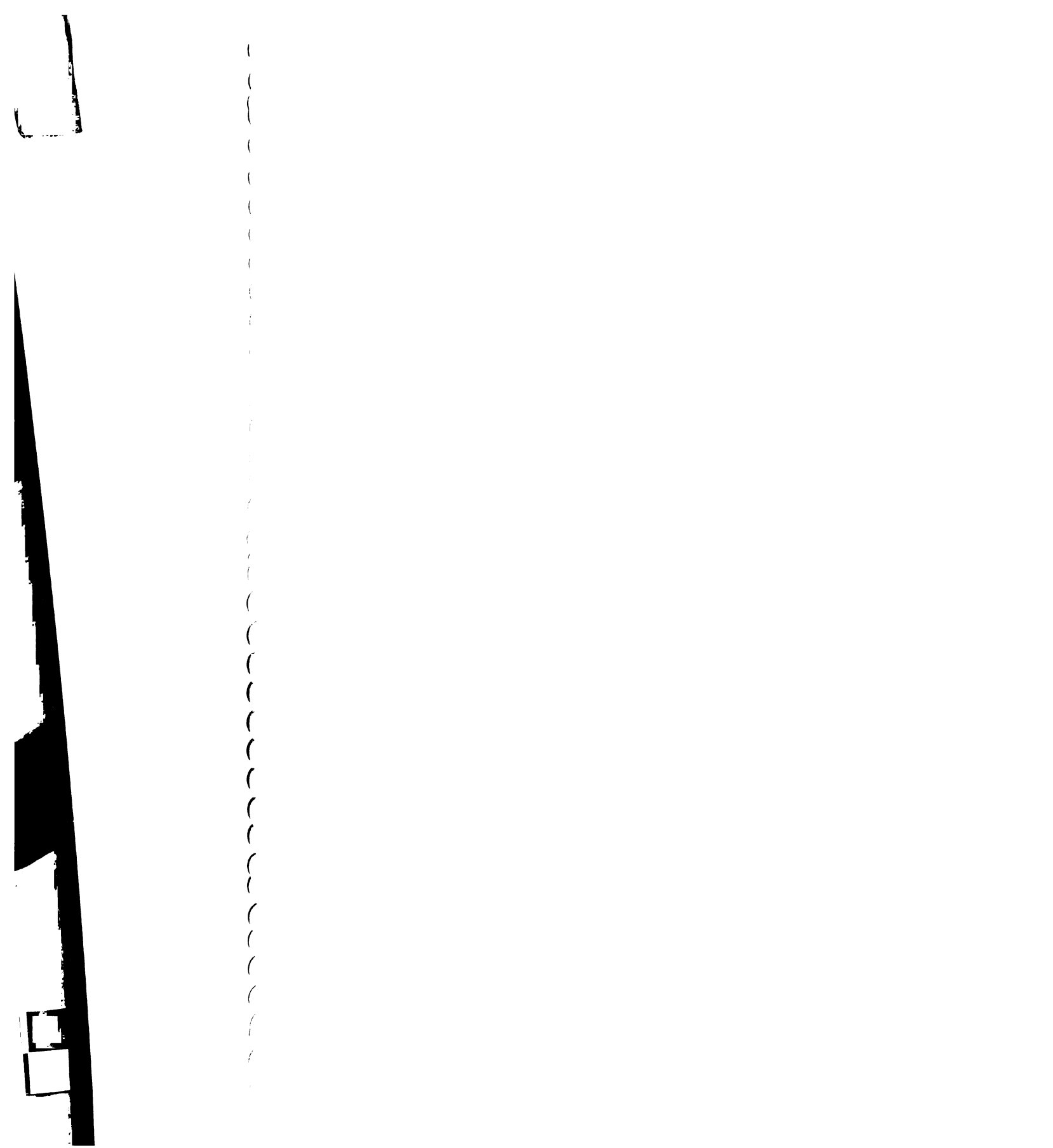


Figure 29

Optical micrographs showing {110} slip plane traces on two faces of an Fe-40Al single crystal deformed at 873K

- (a) Slip lines on the front face of the specimen.
- (b) Slip lines on the right face of the same specimen



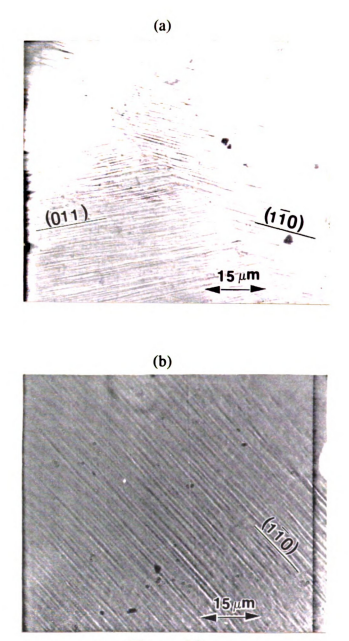
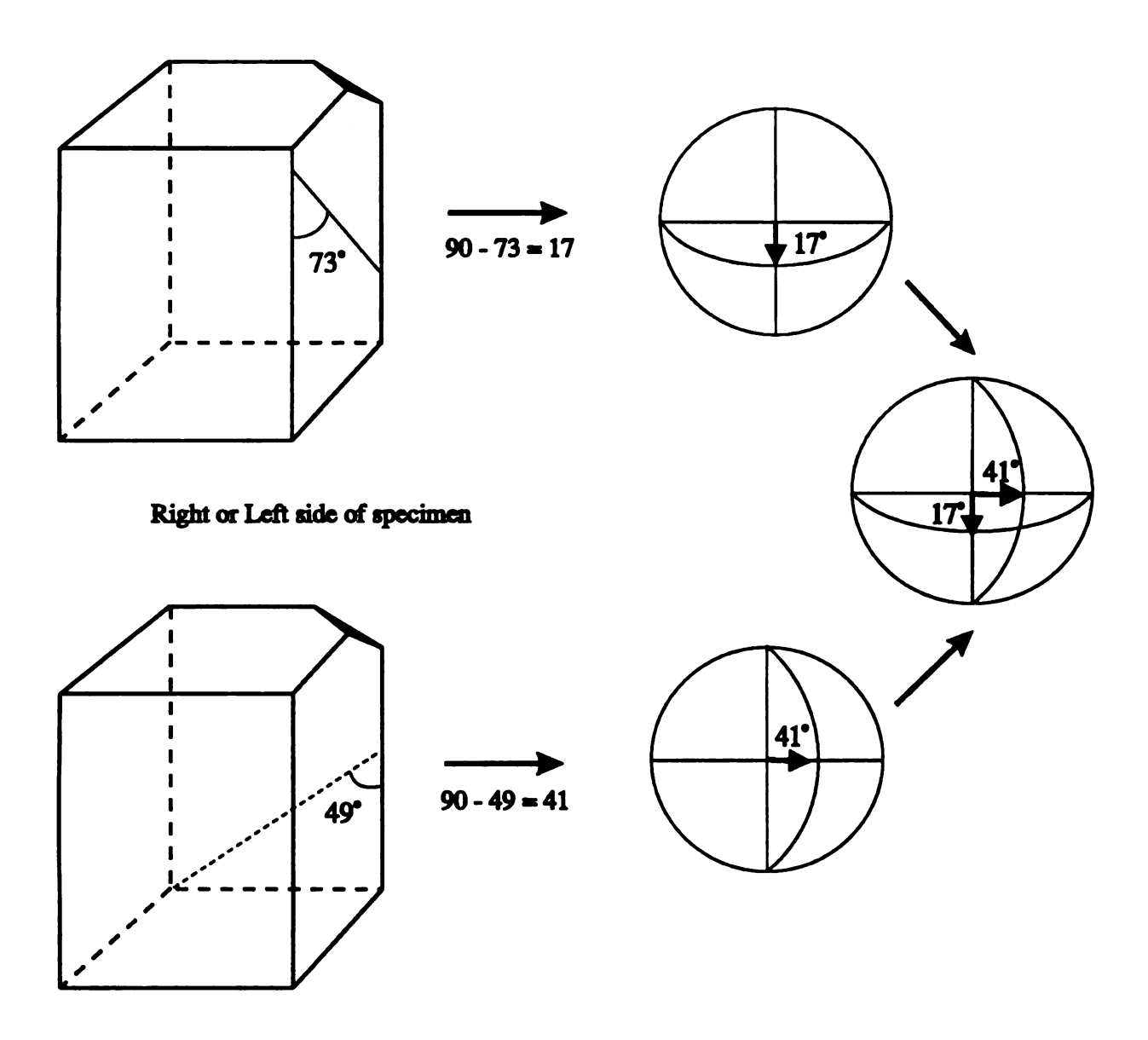


Figure 30

Optical micrographs showing duplex {110} slip plane traces on two faces of an Fe-50Al single crystal deformed at 873K. (a) Duplex slip lines on the left face of an Fe-50Al compression specimen. (b) Slip lines on the front face of the same specimen



Front or Back side of specimen

Figure 31
Illustration of a standard two face slip trace analysis.

observation, considering that previous studies [28-30] give no report of thermal history (following elevated temperature deformation) and that their findings do not show the same slip transition temperature dependence with respect to stoichiometry.

# 3.2 Burgers Vector Determination

Burgers vector determinations were carried out with TEM, using conventional diffraction contrast imaging. Both the  $\mathbf{g} \cdot \mathbf{b} = 0$  and  $\mathbf{g} \cdot \mathbf{b} \times \mathbf{u} = 0$  criteria were employed. Foils used for the analysis were sectioned parallel to the active {110} planes or parallel to {001} planes lying parallel to the [100] deformation axis ((001) and (010)).

In order to perform a proper analysis, only low index, regular lattice spots were used for two-beam imaging of dislocations. Superlattice spots are not used due to large extinction distances, which result in diffuse images with weak contrast. Images were always taken in  $\{100\}$ ,  $\{110\}$  and  $\{111\}$  zones which could be tilted to. Figure 32 shows a map of the low index zones and **g**-vectors used for the  $\mathbf{g} \cdot \mathbf{b} = 0$  analysis of an Fe-40Al sample. Usually **g**-vectors used in two-beam imaging were not used twice if contained in two different low-index zones used for analysis.

Observation of a foil cut parallel to a  $\{011\}$  slip plane shows that the dislocations are generally straight, have sharp jogs and lie roughly 90 degrees to one another. A set of TEM images used in the burgers vector determination for this alloy can be seen in figures 33(a)-(e). Trace analysis revealed the primary line directions to be  $\mathbf{u} = [100]$  and  $\mathbf{u} = [010]$ .

Due to the high elastic anisotropy of B2 FeAl, Burgers vector analysis can be difficult to perform [65]. In this case, the elastic anisotropy causes  $\mathbf{g} \cdot \mathbf{b} = 0$  to rarely lead to complete invisibility of dislocations for more than one two-beam condition. However, using the  $\mathbf{g} \cdot \mathbf{b} \times \mathbf{u} = 0$  criteria in conjunction with the  $\mathbf{g} \cdot \mathbf{b} = 0$  criteria [65]

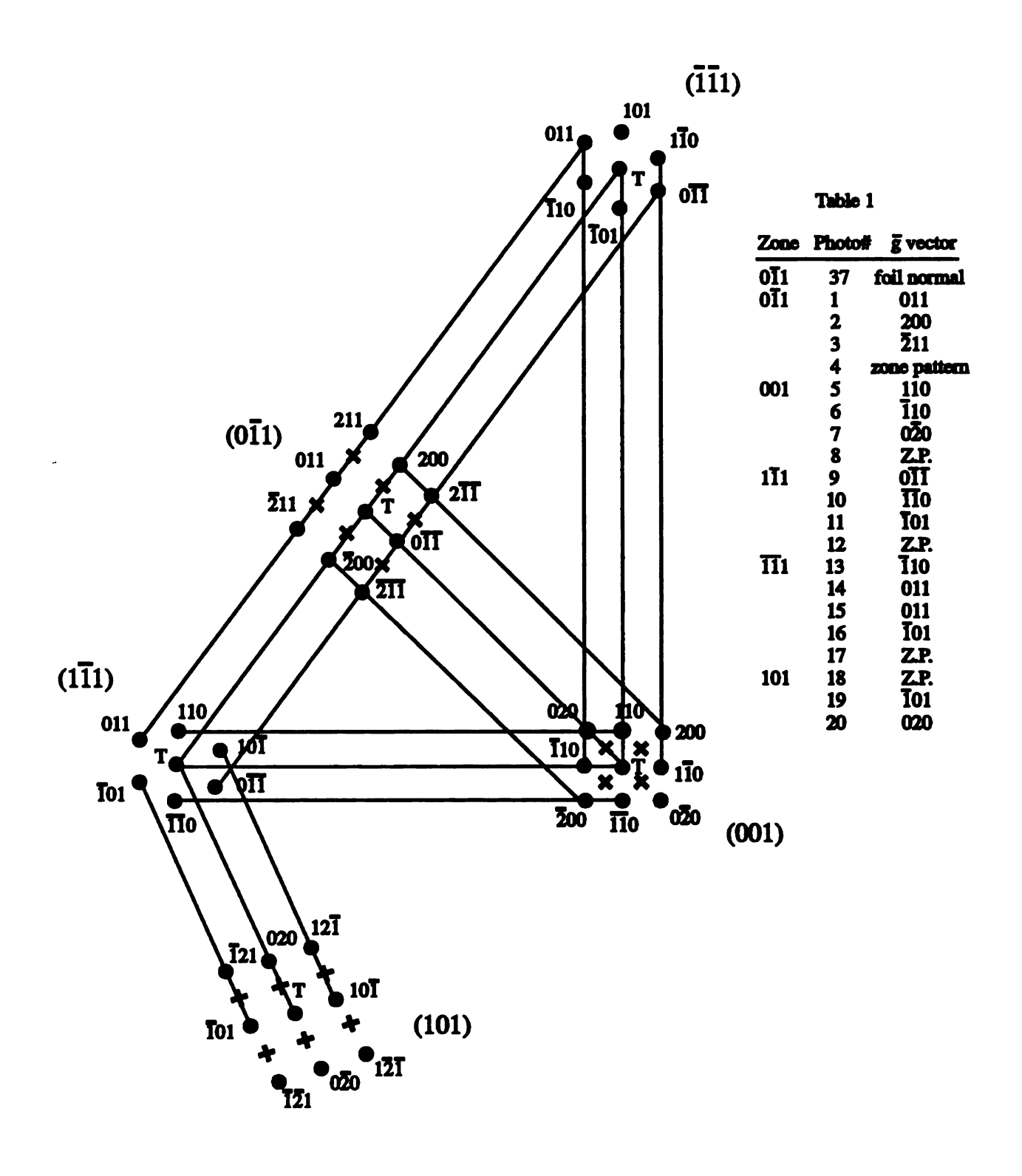


Figure 32 Zone map illustrating the g-vectors used in the  $\mathbf{g} \cdot \mathbf{b} = 0$  analysis of an Fe-40Al compression sample.

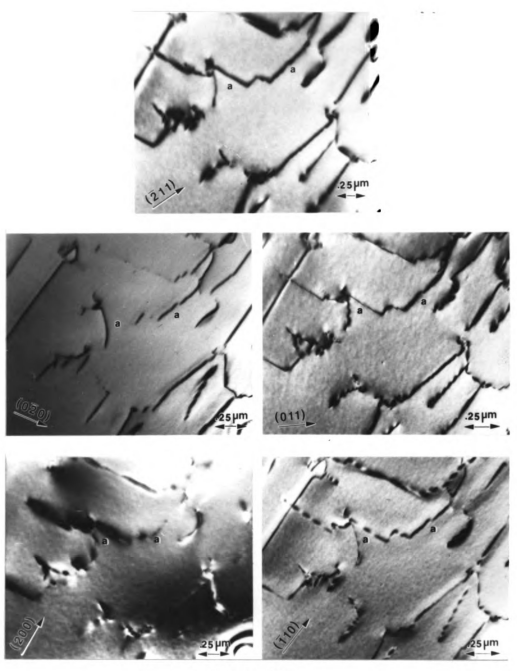


Figure 33

Conventional diffraction contrast images illustrating a Burgers vector analysis in deformed Fe-40Al. The dislocation labeled (a) has b=[001] and line directions of [100] and [010]. Thereby, indicating a prismatic configuration for the dislocation. Figures (a), (c) and (d) were taken near the (011) zone, while (b) and (e) were taken near (001).

a thorough analysis can generally be performed. For example, consider figures 33(a)-(e). The dislocation labeled (a) represents the most commonly observed dislocation in this material. The dislocation has line segments lying in both  $\mathbf{u}_1 = [100]$  and  $\mathbf{u}_2 = [010]$  directions. The  $\mathbf{u}_1 = [100]$  segments are out of contrast for  $\mathbf{g} = (200)$  while the  $\mathbf{u}_2 = [010]$  segments show residual contrast. Additionally, the  $\mathbf{u}_2 = [010]$  segments are out of contrast for  $\mathbf{g} = (020)$ , while the  $\mathbf{u}_1 = [100]$  segments remain in contrast. Applying the  $\mathbf{g} \cdot \mathbf{b} = \mathbf{0}$  and  $\mathbf{g} \cdot \mathbf{b} \times \mathbf{u} = \mathbf{0}$  criteria leads to the conclusion that the Burgers vector of dislocation labeled (a) is  $\mathbf{b} = [001]$ . Similarly, all analyses show that the Burgers vectors of the majority of dislocations in both Fe-40Al and Fe-50Al are  $\mathbf{b} = <001>$  with  $\mathbf{u} = <001>$ .

It should be noted that slip plane determination by the  $\mathbf{b} \times \mathbf{u} = \mathbf{N}$  (where  $\mathbf{N}$  is the slip plane normal) criterion, indicated that  $\{001\}$  were the active slip planes while optical slip trace analysis indicated that  $\{011\}$  were the active slip planes. Since the Burgers vectors of the dislocations are normal to the plane of the dislocations, (defined by the two line directions  $\mathbf{u}_1 \times \mathbf{u}_2$ ) it is clear that the dislocations are not in a glide configuration and a likely conclusion is that the dislocations underwent some form of rearrangement during the cooling process, resulting in the observed dislocation configurations. In fact, this finding would be independent of the slip trace analysis. In addition, several studies [25,61,62] have observed  $\mathbf{b} = <100>$  prismatic dislocations and loops in FeAl as well.

A typical study of an Fe-50Al sample (with  $(0\bar{1}1)$  slip traces indicating the active slip plane) was observed to contain a few long straight  $\mathbf{b} = [111]$  dislocations. Figures 34(a)-(d) are conventional TEM images showing a long straight <111> dislocation surrounded by <100> dislocations. It should be noted that, although evidence of the dislocation can be seen in figure 34(d), the <111> dislocation is actually showing residual contrast.

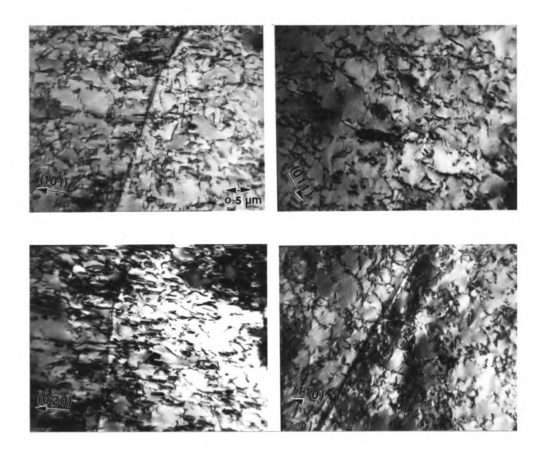


Figure 34

Conventional TEM images of the deformation structure of Fe-50Al deformed at 873K. The substructure is dominated by <100> dislocations. The long straight dislocation is a <111> dislocation. Fig. (a) was taken near the (010) zone, figs. (b) and (c) were taken near (111) and fig. (d) was taken near (001)

## 3.3 High Resolution Electron Microscopy

Due to the high resolution imaging constraints mentioned in section 2.8, foils for HREM were sectioned parallel to (010) and (001). This was done in order to observe the cores of [010] and [001] edge dislocations or dislocations which had atomic displacements lying in the (010) and (001) planes. In other words, crystals were imaged with beam directions down [010] and [001] in order to see the edge component of mixed dislocation cores (Burgers vectors denoted as **b**<sub>e</sub>) or the displacements of prismatic edge dislocation cores (Burgers vectors denoted as **b**).

#### 3.3.1 Fe-40Al

As expected, HREM examination of Fe-40Al revealed  $\mathbf{b} = <001>$  dislocation cores. Figure 35 shows a "white atom" HREM image of a  $\mathbf{b} = [001](100)$  edge dislocation core (36(a)) along with digitally scanned and compressed images (b)-(e). For a "white atom" image, the bright spots represent the approximate atom positions. Digitally scanned images are included in order to aid in viewing planar distortions (both parallel and perpendicular to the "slip plane") and half plane terminations (as seen along the (b) [202], (c) [200], (d) [202] and (e) [002] directions). For the purpose of discussion, we will define the "slip plane" as the plane which contains the Burgers vector and line direction of the dislocation ( $\mathbf{b} \times \mathbf{u} = \mathbf{N}$ ). However, one can not be sure whether this dislocation moves by glide, climb or a combination of the two.

Upon inspection, it can be seen that the core is composed of two distinct {220} half planes terminating approximately one interatomic spacing apart from each other in the [200] direction. Additionally, the half planes are separated by approximately one and a half interatomic positions along the [002] direction. Arrows in the upper left and right corners of figure 35(a) and compressed images (b) and (d)

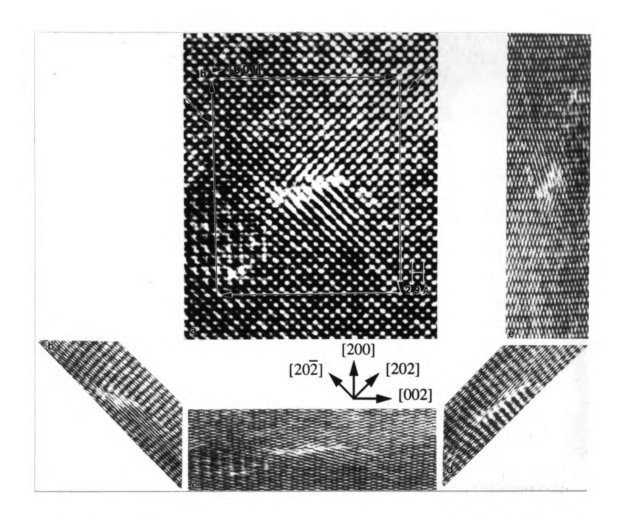


Figure 35

(a) Experimental HREM image of a  $\mathbf{b} = [001](100)$  edge dislocation core found in Fe-40Al. (b-e) Digitally scanned and compressed images of (a) representing views down the (b) [202] (c) [200] (d) [20 $\bar{2}$ ] and (e) [002] directions.

help in the visual identification of the half plane terminations. The core is characterized as being compact with little spreading in the (100) slip plane (see figure 35(c)) and no signifigant planar distortions in the direction perpendicular to the slip plane (see figure 35(e)). The compact arrangement of this core is very similar to cores seen in studies of Ni-50Al and Ni-48Al [5,66].

Unexpectedly, a  $b_e = <110>$  dislocation core was observed in the material as well. This core displays an edge-component Burgers vector, denoted as  $\mathbf{b_e} = [101]$ . The core is displayed as initially imaged and after a few minutes exposure to the microscope's electron beam (figures 36(a) and 36(b) respectively). Inspection of figure 36(a), reveals that the core is composed of two adjacently arranged half planes (each with  $b_e$  = 1/2[101]) with their terminating atoms separated in the [202] direction by six interatomic positions. This configuration appears to be the result of climb dissociation and can be seen in figure 36(a). This type of dislocation is of interest, considering that no b = [101],  $\mathbf{u} = <100>$  dislocations were observed in any of the TEM analyses. Consequently, one can not conclude that the dislocation was formed during high temperature deformation of the crystal. Therefore, given the observed [101] Burgers vector, it is not entirely clear what the dislocation is or how it relates to the deformation structure. Using the Peach-Koehler approach for elastically isotropic materials and assuming that the partial dislocations were at their equilibrium spacing in figure 36(a), the APB energy was approximated for the {110} plane. The APB energy was found to be 140 mJ/m<sup>2</sup> for partials with parallel Burgers vectors and 190 mJ/m<sup>2</sup> for partial dislocations with antiparallel Burgers vectors. The details of these calculations can be found in the appendix. Experimentally determined APB energies for 1/2<111> dislocations (using weak beam electron microscopy) found values to be near 150 mJ/m<sup>2</sup> [67]. The difference in the energies is negligible and in fact, the APB energy for parallel Burgers vectors is less than the experimentally observed 1/2<111> APB. The difference in energy may be the result of vacancy interactions and/or anisotropic atomic relaxations.

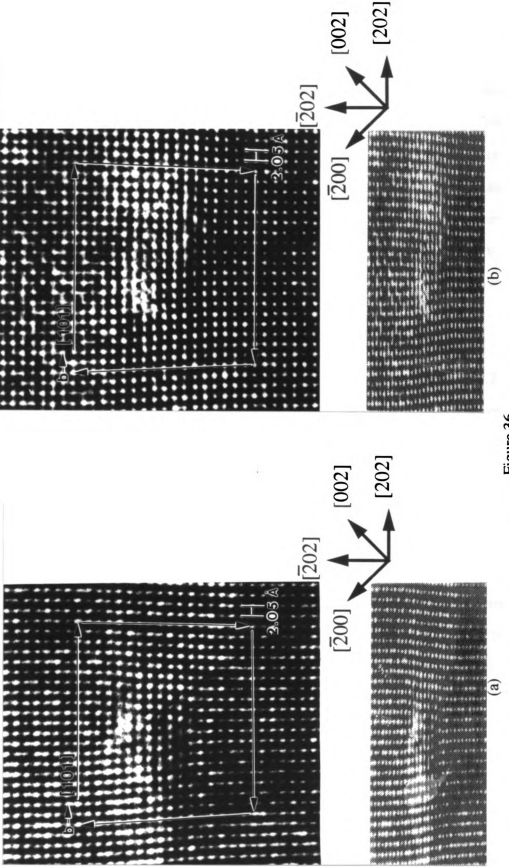


Figure 36

Experimental HREM images of a climb dissociated dislocation core in Fe-40Al with a **be** = [101] edge component. (a) The core as initially imaged (b). The same core following bean induced glide dissociation of the partials.

#### 3.3.2 Fe-50Al

HREM studies of Fe-50Al found several dislocation cores with  $\mathbf{b_e} = <100>$ . Dislocation cores with other Burgers vectors were not observed in this material. Interestingly, each of the  $\mathbf{b_e} = <100>$  cores displayed a different partial-dislocation arrangement. Figure 37 shows an experimental image of the first type of  $\mathbf{b} = [100]$  core. This core is compact, like the Fe-40Al core, but subtly different. The Fe-40Al core has half-planes separated in the [002] direction by about two interatomic positions and by one interatomic position in the [200] direction, whereas the Fe-50Al core is composed of two half planes separated in the [002] and [200] directions by approximately two interatomic positions. Therefore, the Fe-50Al core displays a slightly larger climb component, suggesting a less glissile core.

Another  $b_e = [100]$  core found in Fe-50Al is displayed in figure 38. It can be seen that the half plane terminations of this core are separated by 10-12 atom positions relative to the [002] direction and about 2 interatomic positions relative to the [200] direction. The width of the spread between the partial dislocations indicates a complete dissociation of the perfect dislocation into two distinct partials. Figure 38 displays the two 1/2<110> burgers circuts around the partial cores. The Burgers vectors help to illustrate that the partials are arranged in a v-shaped configuration.

Figure 39 displays two <100> dislocation cores in an apparent dipole configuration. The two cores have opposite Burgers vectors, are compact and are separated by about 10 interatomic positions in the [200] direction. In addition, the two dislocation cores appear to lie along a line orthogonal to the Burgers vector, but due to resolution limits, one can not be certain.

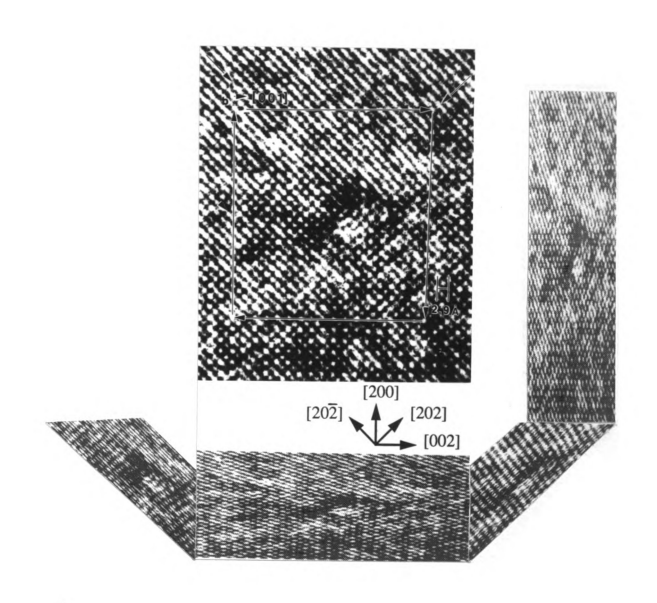


Figure 37

HREM image of a compact [001](100) dislocation core in Fe-50Al. Close examination of the {220} extra half planes reveals that they are climb dissociated perpendicular to the plane containing the burgers vector.

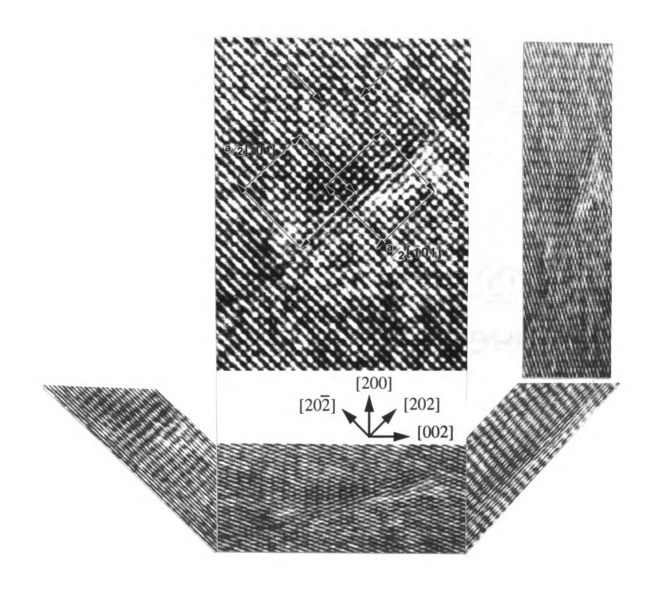
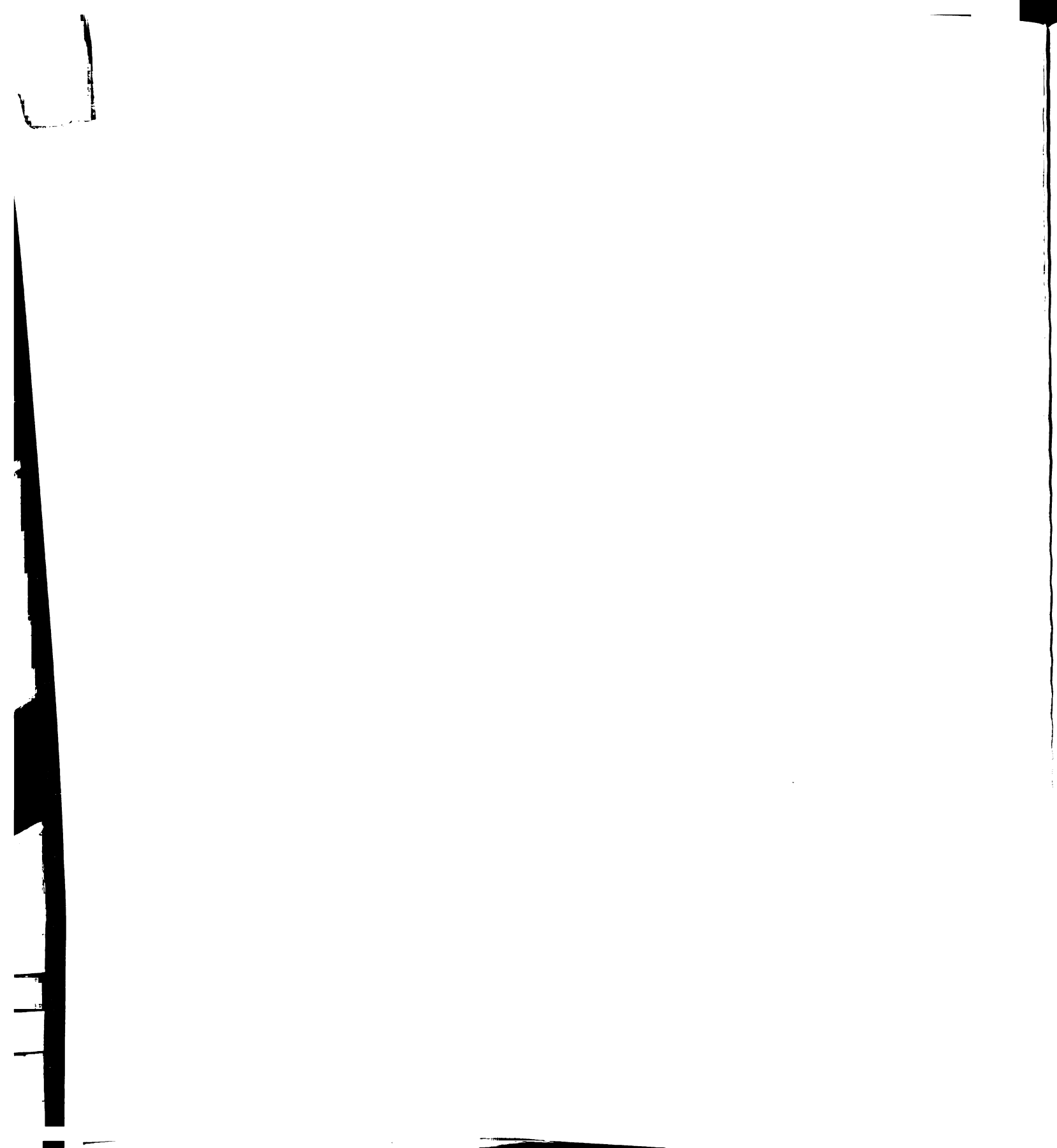


Figure 38

HREM image of a dissociated [001](100) dislocation core in Fe-50Al. The burgers circuits around the partials, implying that positive climb might have been involved.



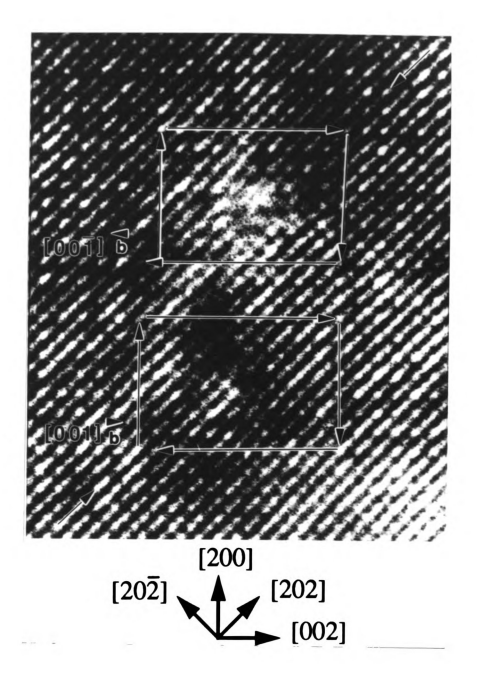


Figure 39

HREM image of two <001> edge dislocations in an apparent dipole configuration in Fe-50Al. The two dislocations lie approximately 10 atomic positions apart in the [200] direction.

#### 4. Discussion

Now that the dislocation cores have been characterized, the exact nature of these cores, how they formed and how they relate to the high temperature deformation structure will be determined. In addition, the core structures will be used to explain the observed differences in the mechanical behaviors of the two FeAl alloys, NiAl and CoAl. Finally, the implications these core sturctures have for dislocations involved in low temperature deformation will be discussed.

# 4.1 Rationalization of Slip Trace and Diffraction Contrast Analyses

A finding of primary importance in this study is the fact that optical slip-trace analyses and TEM analyses consistently yielded different slip plane determinations ({110} versus {100} respectively). Since TEM studies revealed that the majority of dislocations were of the prismatic <100>{001} type, one may conclude that vacancies interacted with the dislocations during and/or following elevated temperature deformation. In addition, this raises the question: Do vacancies diffuse to the dislocation lines, get picked up by gliding dislocations or form their own dislocations through vacancy coalescence? Additionally, questions are rasied as to whether vacancy assisted processes (such as dislocation climb) comprise a major portion of the deformation process in FeAl at elevated temperatures or none at all. This finding strongly suggests that there actually is no <111> - <100> slip transition in this material.

#### 4.2 <110> Core Observed in Fe-40Al

It is important to reiterate that HREM only resolves atomic displacements which are perpendicular to the electron beam of the microscope. In other words, when considering the  $\mathbf{b_e} = [101]$  in figure 36, HREM only views the edge displacements of the dislocation core. In fact, the <110> direction in the B2 lattice is not a closest-packed direction and therefore, not a direction in which dislocations

would theoretically prefer to travel [22]. For bcc and B2 metals, the close-packed direction is <111>. Additionally, 1/2<110> is not an atom to atom translation in the B2 structure (see figure 1 for the <110> vector). Consequently, it is most likely that we are observing the edge component of a different type of dislocation. Since it is known that <111> dislocations make up the primary deformation mechanism of bcc metals and B2 FeAl at lower temperatures, [22-24, 26-30] it is probable that figure 36 displays the edge components of two 1/2<111> partial dislocations coupled by an APB. However, since we have no proof, all types of dislocation scenarios should be considered. The following dislocation scenarios constitute the most probable reactions. (1) If the perfect dislocation is **b** = [101], then the dislocation dissociation type could be:

$$[101] \stackrel{\text{climb}}{=} > 1/2[111] + \gamma_{APB(001)} + 1/2[111]$$

(2) If the perfect dislocation is b = [111], then the dislocation dissociation type could be:  $[111] \stackrel{\text{climb}}{=} > 1/2[111] + \gamma_{\text{APB}(001)} + 1/2[111]$ 

Unfortunately, it becomes difficult to evaluate the energies of these dissociations due to the high degree of elastic anisotropy and high vacancy concentration in this material. Although Frank's Rule is designed to evaluate the energies of dislocation dissociations in elastically isotropic materials, it still provides a starting point with which one may begin to analyze the energies of the above reactions. Using Frank's rule, both reactions (1) and (2) are considered to be energetically favorable ((2 > 1.5 + APB) and (3 > 1.5 + APB) respectively). Although Frank's rule indicates that both dissociations are energetically favorable, dissociation (2) would appear to be preferred. Another consideration, which may help to determine which dissociation is more energetically favorable, deals with linear elasticity energy considerations of the arrangement of two edge dislocactions. Linear elasticity predicts that two edge dislocactions are in their most energetically stable configuration when they are

positioned directly above one another (figure 36(a)) and this is not taken into account by Frank's rule. No matter which dissociation proves to to have the lowest energy, it could be possible that these climb dissociations are an energetically favorable form of vacancy annihilation in this material. In other words, the overall dislocation line energy may increase, due to these interactions, but the total system energy may decrease as excess thermal vacancies are eliminated. Recall that vacancies tend to form dislocation products in FeAl rather than voids [10-13] and that the post-deformation cooling rate of this material was slow enough to allow for these formations. In addition, the discrepancy between observed slip plane ({110} versus {100} using optical slip-trace analysis and TEM study) leads to the conclusion that there may actually be post-deformation rearrangement of vacancies and dislocations in the material. Therefore, it is possible that the  $\mathbf{b_e} = <110>$  core observed was part of a dislocation involved in the deformation of the material which later became immobile through vacancy interaction.

Figure 36(b) illustrates that prolonged exposure to the beam has caused the partials to glide apart (in the direction of the Burgers vector) by about four interatomic positions. This motion creates an additional antiphase boundary in the direction of the Burgers vector. Interestingly, the creation of this additional APB does not help to eliminate vacancies. In addition, it imposes additional drag which should further restrict motion of the partial dislocations and create a higher energy system. Again, linear elasticity theory would seem to indicate that the glide dissociation is energetically unfavorable. Since it is possible that the high thermal vacancy concentrations in this material alters these considerations, it might imply that local stresses caused by beam induced vacancy movement near the <110> core resulted in the post-deformation glide of the partials, thereby providing a way to reestablish local equilibrium. Thus, while one comes to the conclusion that this glide dissociation of the half planes does not appear to be an energetically favorable

reaction, the exact driving mechanisms and energies involved in this reaction remain to be determined.

#### 4.3 Dissociated Core Observed in Fe-50Al

With respect to the dissociated core in Fe-50Al (figure 38), the dissociation reaction of the edge components would be:

$$[100]_e = 1/2[10I]_e + [101]_e$$

However, as outlined in the previous section, 1/2<110> is not a reasonable partial dislocation. This implies that a <111> dissociation, which takes into account the unresolvable screw displacements parallel with the beam of the microscope, should also be considered. A possible reaction would be:

$$[100] = 1/2[1\overline{1}] + APB + 1/2[111]$$

Although this reaction is most likely, it requires that the partials do more than just glide in the slip plane "N" (as defined by  $\mathbf{b}_{[001]} \times \mathbf{u}_{[010]}$ ). For instance, the overall Burgers vector and line direction (as determined by TEM analysis in figure 38) defines N as (200). In B2 FeAl, <111> dislocations cannot glide in {200} planes. Instead, mixed <111> dislocations with line directions  $\mathbf{u} = <001>$  must lie on {110} planes, [23] (i.e. corresponding with the optical slip-trace analyses).

If the observed partials came from a single perfect dislocation, two possible dissociation reactions which could create the observed dissociation configuration are illustrated in figure 40. The first type of reaction requires that both 1/2<111> partials break out of the perfect dislocation configuration and glide apart on perpendicular {220} planes. This would result in the v-shaped configuration of the partials seen in figure 38. The second type of dissociation reaction would involve negative climb (addition of extra atoms to the half planes) of the partials into the v-shaped configuration. However, it should be noted that positive climb (removal of atoms) does not result in the observed configuration. It should also be noted that

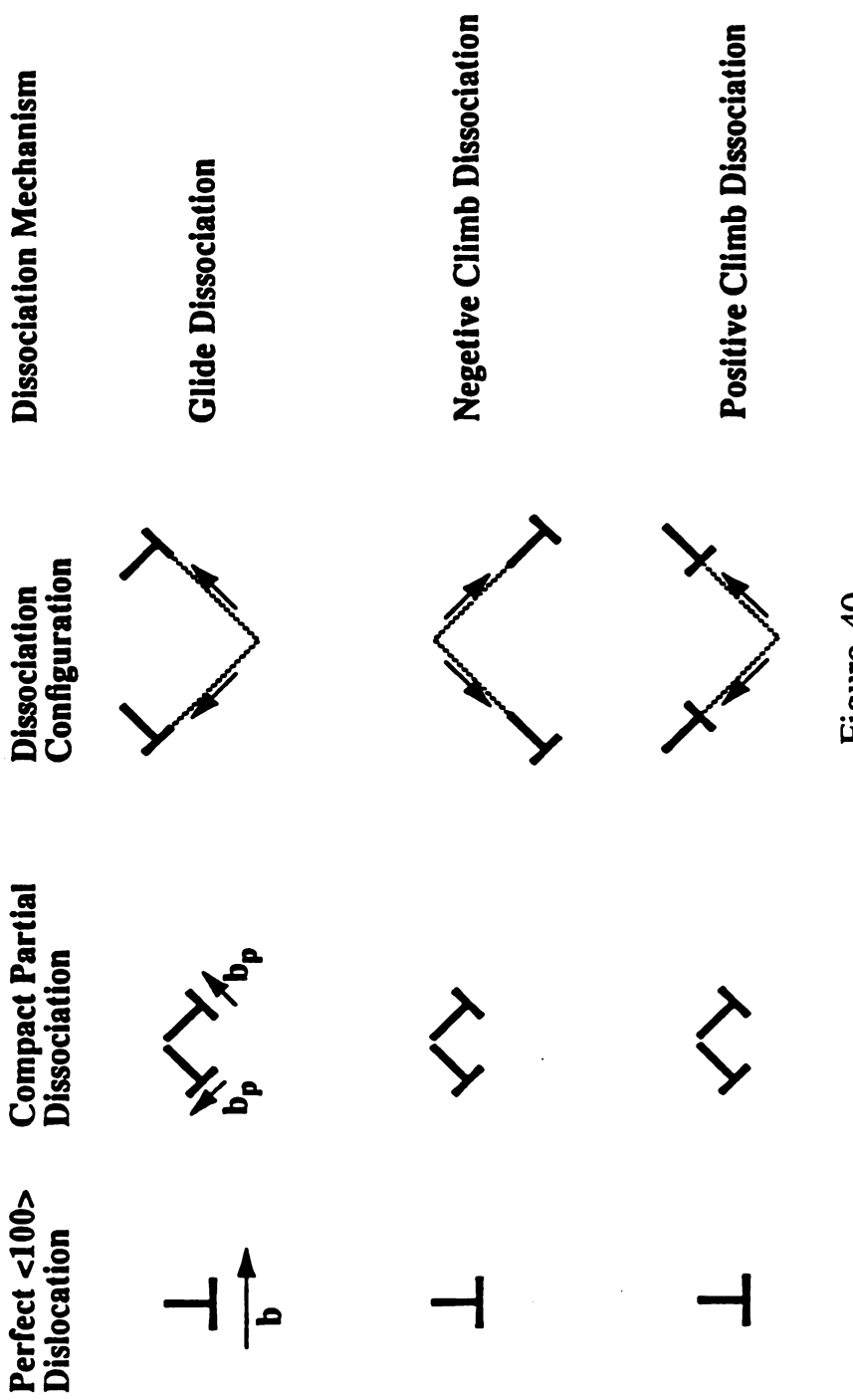


Figure 40

arrows denote the direction of the dislocation's motion. Note, only the glide dissociation or negative climb dissociation could result which could result in 1/2<111> partials being separated along a {100} plane. The dashed lines represent an APB ribbon and the Schematic representations of possible glide and climb mechanisms in a configuration consistent with figure 38. dissociation of a perfect <100> dislocation into two 1/2<111> partials is not considered energetically favorable with respect to linear elasticity theory. However, contrary to linear elasticity, Fordeaux et al. [61] have observed this type of dislocation dissociation to be a form of vacancy annihilation in Fe-42Al.

# 4.4 An Apparent Dipole Observed in Fe-50Al

With respect to the apparent dipole arrangement of the cores observed in figure 39, linear elasticity predicts that an edge dislocation dipole (which forms by slip) should be configured with the dislocations lying 45° to one another. However, in the observed arrangement, the dislocations lie along the same line and thus are in a higher energy configuration. This type of configuration most closely corresponds to viewing a cross section of a prismatic loop formed by vacancy coalescense. Figure 41(a) illustrates a cross section of a vacancy-formed prismatic loop and figure 41(b) illustrates a cross section of an interstitial dipole. Comparison of figures 39 and 41(a) shows that the observed configuration corresponds to the vacancy-formed prismatic loop and not an interstitial dipole. This structure may also be a product of the large number of thermal vacancies produced in this material during high temperature deformation. In fact, recall that many high temperature deformation studies of FeAl have discovered <100> dipole loops in the material [25,61,62]. Therefore, it is possible that the image in figure 39 is a cross section of a prismatic loop nucleus.

### 4.5 Comparison of A Model Core With Observed Cores

Imaging down <100> directions has revealed several dislocation core structures in B2 FeAl deformed at 873K. In order to facilitate comparison of experimentally observed dislocation core structures with theoretical structures, a theoretical <100> edge dislocation core of Fe-50Al was provided by Vailhe and Farkas [63] (see figure 42). The upper left figure illustrates a plot of the atomic positions determined by the embedded atom method (EAM), while the other figures are a series of simulated HREM core images based on the theoretical structure. It

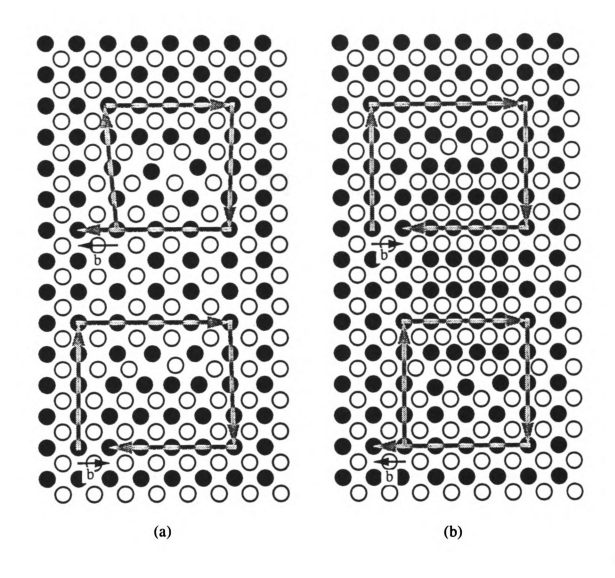
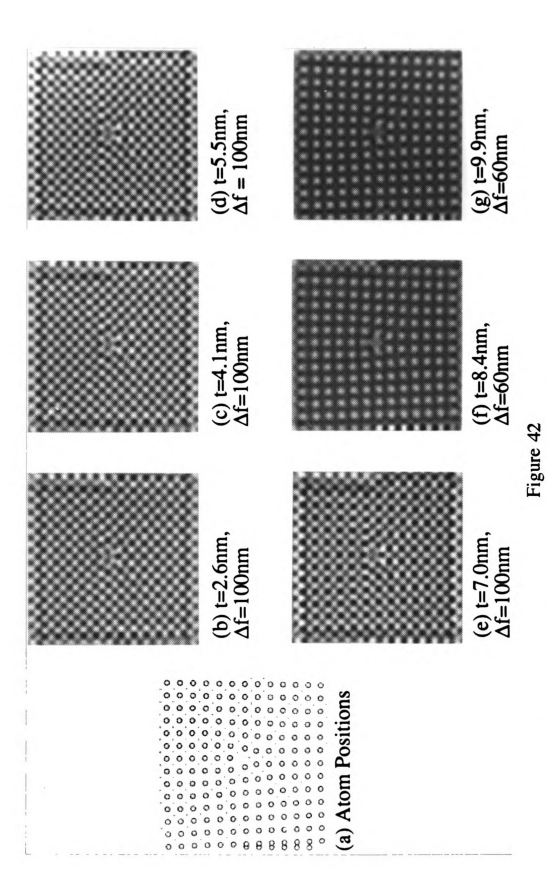


Figure 41

- (a) Schematic cross section of a vacancy-formed prismatic dipole.
- (b) Schematic cross section of an interstitial dipole.

Note the sense of the burgers vector of the vacancy formed dipole is consistent with the image observed in figure 39.



(a) Atom positions for a <001>{100} edge dislocation as determined by EAM. (b)-(g) Simulated HREM images based on the atom positions shown in (a).

should be noted that the EAM does not account for climb, unless it is purposely included with the input parameters. That is, EAM is not capable of modeling diffusion during the relaxation process and the core provided by Farkas et al. [63] (figure 40) does not account for climb. The theoretical image displays a compact core with little spreading or distortions in either the planes containing the Burgers vector or planes normal to the Burgers vector. In other words, the {200} half planes making up the superdislocation can both be seen to terminate on N and are separated by one atomic position in the direction of the Burgers vector (indicating that both {200} half planes are composed of the same atomic species). This theoretical structure is considerably different from the experimentally observed sturctures. All experimentally observed structures displayed varying degrees of spreading and/or climb. In addition, half planes in the experimental images were found to be arranged differently. The half planes were either arranged side by side ({200} half planes consisted of two different atomic species) or were separated by several atomic positions in the direction of the Burgers vector. The reasons for these differences are not entirely clear. The differences are most likely the result of vacancydislocation interactions. For instance, Jungua et al. [60] observed vacancy formed superpartial loops, which had climbed 10 to 20 times further apart than their theoretically calculated equilibrium distance (0.1-0.3 µm vs. 150Å). They attributed this phenomenon to the depletion of the local vacancy supply as it assisted the climb of the first partial loop and left the other loop behind. In addition, Junqua et al. observed complex reactions between <100> type dislocations and vacancy loops, which resulted in helices with <111> Burgers vectors. They proposed that two perfect edge dislocations with [100] and [010] burgers vectors combined at a node to form a screw dislocation with a [110] burgers vector (energetically identical). Then, a quench loop formed by vacancy cluster collapse and having a Burgers vector of



1/2[111] interacts with the [110] dislocation, forming a helix turn. Figure 43 illustrates their proposed mechanism for the formation of a helix pair. Close examination of the half plane terminations in the **b** = [001] Fe-40Al core, (figure 35) reveals that the vertical separation of the half planes does not appear to be a full <100> lattice translation.

Instead, it appears to be half the distance. A similar configuration appears to be displayed in a [001] dislocation core found in Fe-50Al (figure 37). Although unrelated structurally, the observation of the prismatic loop (a sessile configuration) in figure 40 would tend to support the theory that the observed dislocation cores are not glissile. In fact, it intuitively makes sense that a dislocation core composed of partials which terminate on different slip planes would be difficult to move by slip.

# 4.5.1 Dislocation Observations and Cooling Rate Effects

It has been observed that the dislocation cores seen in this study are in non-planer configurations. This should make dislocation glide difficult and it raises the question: Is there a signifigant contribution to the deformation of the material by climb? This may be a possibility, given the deformation temperature and strain rate used to test the material (.67T<sub>m</sub> and 2.4 x 10<sup>-4</sup> s<sup>-1</sup>). In fact, this hypothesis may be supported by the dislocation configurations observed in the TEM analyses (figures 33 and 34). However, since the slip lines on the faces of the samples indicated deformation by dislocations gliding on {110}, it is difficult to conclude whether the dislocation cores observed represent in-situ deformation conditions or post-deformation conditions. If the cores are representative of the in-situ deformation condition, it is possible that dislocation core structures became altered as they picked up vacancies lying along their glide paths. As temperature increases, vacancies increase in number. Consequently, a dislocation gliding (involved in the plastic deformation of the material at elevated temperatures) is bound to encounter many vacancies, which would most likely diffuse to the dislocation's core. Vacancy

$$[110] + \frac{1}{2}[\bar{1}\bar{1}\bar{1}] \longrightarrow \frac{1}{2}[11\bar{1}]$$
$$2 + \frac{3}{4} \longrightarrow \frac{3}{4}$$

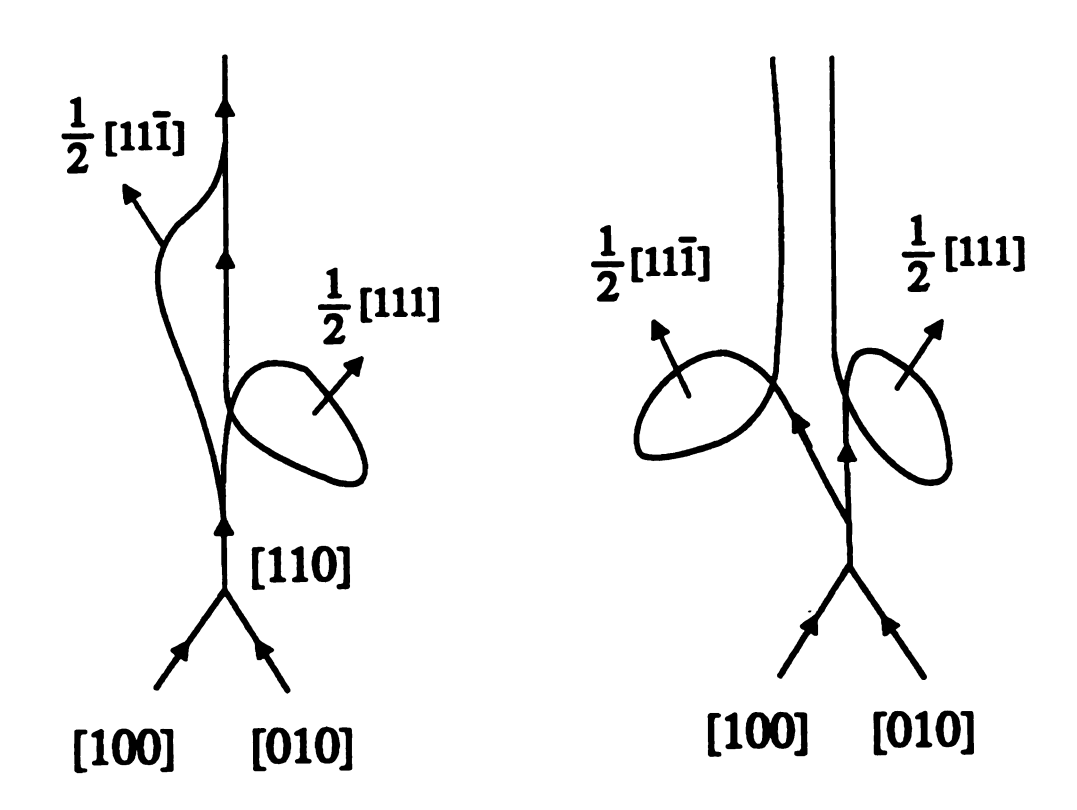


Figure 43

Schematic representation of a possible helice formation mechanism. Adapted from [60]

diffusion to dislocation cores may occur because the vacancies are no longer in a state of equilibrium when a deformation load is applied.

If the cores are representative of a post-deformation condition, it is possible that dislocations are acting as sinks for non-equilibrium vacancies during cooling (following release of the deformation load). Rationalization of strong post-deformation dislocationvacancy interactions is also given by the fact that the optical slip trace analyses of the deformed specimens revealed a completely different slip plane than did the TEM analyses ({110} versus {100}, see section 3.1). If this is the case, what implications does this behavior have for specimens deformed at room temperature? Clearly, the observations of the present study suggest that vacancies will interact strongly with dislocations. In a material with high numbers of quenched in vacancies, room temperature deformation may be more difficult, due to vacancy related changes in dislocation core structure. In contrast, a material with low vacancy concentrations (due to slow cooling or annealing) may not experience core altering interactions and may not display the same increase in strength. It should be noted that the vacancy-dislocation interaction may occur through somewhat different mechanisms during room temperature deformation. For instance, the vacancies could be capable of entering dislocation cores via short range diffusion, or they may enter dislocation cores as the dislocations move by slip.

A possible explanation for the unusual dislocation core configurations observed may have to do with the elastically anisotropic nature of FeAl. This implies that the dislocation cores in FeAl are not as symmetric as in elastically isotropic materials. Intuitively, it makes sense that vacancies diffusing to a dislocation core in an elastically anisotropic material would probably alter the core structure of the dislocation even further. This would occur due to the asymmetric relaxations in the dislocation cores being enhanced by the presence of the vacancies. In summary, it is highly likely that the cooling rate (following deformation of the samples) allowed for

signifigant post-deformation vacancy-dislocation reactions (including the alteration of dislocation core structures).

# **4.5.2 Other Factors Which May Affect Core Structure**

Although it seems most likely that vacancies appear to be the major factor influencing the dislocation core structures in the material tested, other factors which might influence the structures of the cores observed should also be discussed. For instance, it could be possible that thin foil geometries allow for unusual atomic relaxations with respect to the bulk crystal. This might enable the short dislocation segments in the thin areas of the foil to dissociate or cross slip in unusual directions, (i.e. <111>) rendering the dislocation immobile. With respect to beam effects and post-deformation dislocation motion, this study has observed dislocations "jumping" out of TEM foils (after a few minutes of beam exposure at 200Kv) and HREM was observed to cause an energetically unfavorable partial dissociation at 350Kv. Thefore, it might be possible that the energy of the beam allowed excess vacancies to become mobile and interact with the dislocation cores, causing the unexpected core structures observed as well.

Another possibility might be that the computer modeling parameters are not specific enough to accurately emulate the behavior of this material. For instance, improper choice of the elastic center or inaccurate pair potentials may need to be corrected or modified. Observation of the difference in the species making up the half planes (experimental versus theoretical cores) is worth considering here.

In any case, most of the dislocation cores appear to involve reactions which are not simple cases of glide. Instead, they appear to involve at least glide and climb.

Therefore, one would not necessarily expect to see overwhelming similarities between these types of dislocation cores and the perfect glide-type dislocation core calculated by EAM.

# 4.6 Comparison Between Fe-40Al and Fe-50Al Cores

Although only a half-dozen cores were observed between both compositions, it is still useful to compare the strucures of these cores. Certainly, it is possible that the unique cores found in one composition could be found in the other composition (given unlimited time and funding). However, since lattice distortions are a symptom of an intrinsic material property, it is still scientifically valid to compare the degree of the lattice distortions around these cores in order to rationalize the observed differences in the mechanical properties of the two compositions and other aluminides.

Comparison of the [001] cores in Fe-40Al and Fe-50Al reveals several differences in morphology. The [001] dislocation core observed in Fe-40Al (figure 35) and the [001] Fe-50Al dislocation cores (found in figures 37 and 39) display structural differences, which may help to rationalize the differences in hardness and strength of the two alloys. For instance, the Fe-40Al core displays a wider separation between the partial dislocations in the direction of the burgers vector. This is indicative of a lower APB energy and a correspondingly lower CRSS for Fe-40Al. Experimental studies of hardness and strength [7,19] concur with this observation. Closer analysis of the cores in figures 35, 37 and 39 show that there are greater planar distortions parallel and perpendicular to the burgers vector for the Fe-50Al cores as well. Again, implying that a greater force is required for dislocation motion in Fe-50Al. Although the planar distortions are greater in the Fe-50Al alloy, they are signifigantly less than those observed in the <001> cores of the stronger B2 alloys NiAl and CoAl (figures 44 and 45). Even though observation of the planar distortions around the dislocation cores would seem to confirm macroscopic observations of hardness and strength, the author does not believe that the observed cores are necessairly representative of glide-type dislocations involved in the deformation process. However, it is also

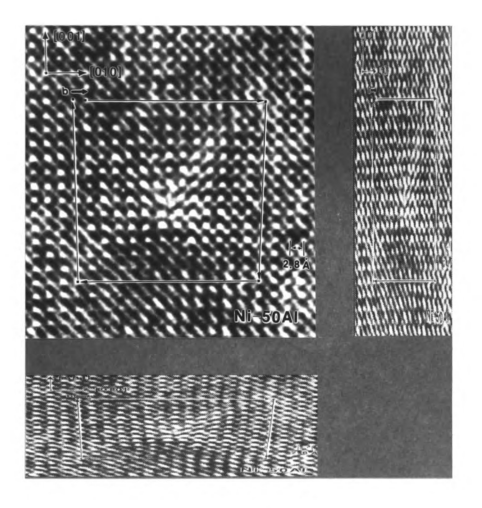


Figure 44

Experimental HREM image of a b = [010] edge dislocation core found in Ni-50Al. Note the greater planar distortions parallel and perpendicular to the burgers vector. Adapted from [5]

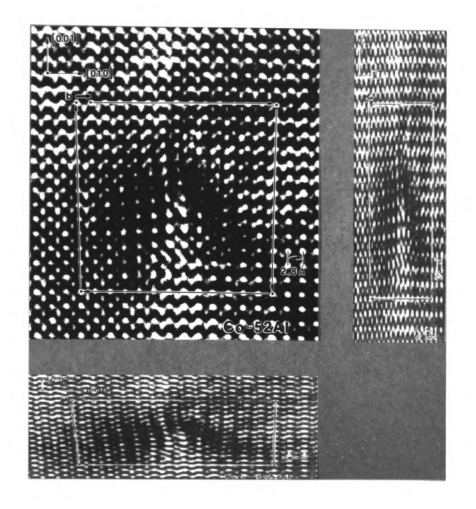


Figure 45

Experimental HREM image of a b = [010] edge dislocation core found in Co-52Al. Again, note the greater planar distortions around the core, compared to Fe-50Al. Adapted from [46]

believed that the high vacancy concentrations in this material are bound to interact with and alter the core structures of gliding dislocations at any temperature. Additionally, it is believed that technological improvements are needed before dislocation core study can lead to information reliable enough to build upon.

In order to get closer to accurately studying the morphology of the cores involved in the deformation process, it might be helpful to catch them on film. Possibly, a stage capable of deforming a HREM foil in a controlled manner could be used in conjuction with computer aided focusing of the area under study. Then, filming the motion of dislocation cores (using a high speed VCR or other device) might be possible. Hopefully, this would allow one to get a more precise idea of how the cores are moving.

### 5. Conclusions

Slip trace analysis of Fe-40Al and Fe-50Al single crystals, compressed near <001> at 873K, has revealed {110} to be the active slip plane, while TEM and HREM studies discovered substructures dominated by <100>{001} prismatic edge dislocations (N = {100} = glide plane). Since vacancy supersaturations exist in this material and since these vacancies have been observed to quickly anneal out into <100>{001} prismatic loops and dislocations at temperatures around 673K, [61] it is believed that the samples were not cooled quickly enough to capture the glide-type dislocations involved in the deformation process. Instead, it might be possible that dislocations interacted with excess thermal vacancies during the deformation process and furnace cooling. It is also possible that there may not actually be a <111> to <100> slip transition for crystals oriented near <100>, but rather a temperature above which vacancies gain enough energy to coalesce on preexisting dislocations and/or form non-glissile <100> prismatic-type dislocations during and or following deformation.

In conclusion, atomic imaging of the core structure of dislocations in B2 Fe-Al revealed compact, relatively distortion free <100> $\{001\}$  cores in a variety of configurations. The configurations include a prismatic loop nuclei, a compact core and dissociated cores. Unexpectedly, a  $\mathbf{b}_{\mathbf{e}} = <110>$  core was observed. All experimentally observed cores showed elements of dissociation and/or climb, which is beyond current computer modeling capabilities.

It is very important to reiterate that while the dislocation cores observed are probably unrelated to dislocations involved in the high temperature deformation of FeAl, the high number of vacancies in the material make it likely that core structures of dislocations involved in low temperature deformation of this material will be signifigantly affected by the vacancies they encounter. Finally, the author feels that signifigant technological advances are necessary before this avenue of

investigation will provide more concrete data on the deformation mechanisms and core structures. of mobile dislocations in B2 FeAl, NiAl and CoAl.

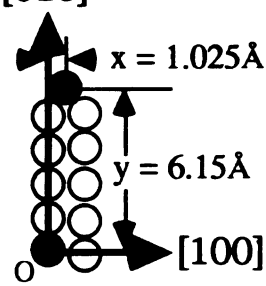
# Appendix

# **Appendix**

# Peach Koehler Approximation

The following is a schematic illustration of the partial dislocation configuration seen in figure 36(a). The dark circles represent the termination atoms. The arrows represent the orientation convention used throughout the analysis. The Burgers vector is assumed to be along the [100] direction for the sake of simplicity.

Choosing the bottom atom as the origin, the coordinates for the second "dislocation core" are:



[010]

Assuming  $a_0 = 2.898$ Å and breaking each partial dislocation's Burgers vector into edge and screw components, gives:

$$b_{[100]} = b_{edge} = \sqrt{2/2}a_0 = 2.05\text{\AA}$$
  
 $b_{[001]} = b_{screw} = 1/2a_0 = 1.45\text{\AA}$ 

Assume: 
$$E = 244 \text{ GPa}$$
 and  $v = .33$   $G = E/2(1+v) = 91.7 \text{ GPa}$ 

Calculating the stress components:

#### Edge:

$$\begin{aligned} & \underline{D} = Gb / 2\pi (1-v) = 4.5 \text{ Pa-m} \\ & \sigma_{xx} = -Dy(3x^2 + y^2) / (x^2 + y^2)^2 = -7.51 \text{GPa} \\ & \sigma_{yy} = Dy(x^2 - y^2) / (x^2 + y^2)^2 = -6.74 \text{GPa} \\ & \sigma_{xy} = \sigma_{yx} = Dx(x^2 - y^2) / (x^2 + y^2)^2 = -1.123 \text{GPa} \\ & \sigma_{zz} = v(\sigma_{xx} + \sigma_{yy}) = -4.703 \text{GPa} \end{aligned}$$

## Screw:

$$\sigma_{xz} = \sigma_{zx} = -Gby / 2\pi(x^2 + y^2) = -4.34GPa$$

$$\sigma_{yz} = \sigma_{zy} = Gbx / 2\pi(x^2 + y^2) = 3.16GPa$$

Calcui disloc

First, comp

[01

[00]

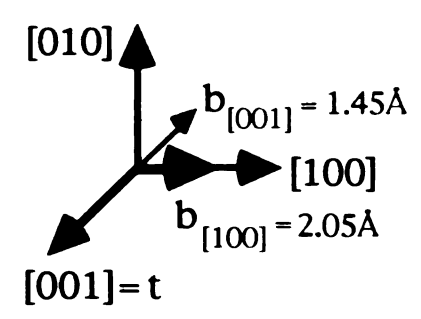
Th

Ed

Ņ

Calculating the force of the edge and screw components of dislocation I (at origin) on dislocation II occurs as follows:

First, the the Burgers vector of the 1/2[110] partial must be broken into x and y components, according to our coordinate system.



Then the force components can be calculated.

<u>Edge</u>:  $b_{[100]} = 2.05$ Å

$$G = \sigma_{ij(I)} = b_{(II)} =$$

$$\sigma_{YZ} \quad \sigma_{YY} \quad 0 \quad \bullet \quad 0$$

$$0 \quad 0 \quad \sigma_{ZZ} \quad 0$$

Now: 
$$(b_{[100]}\sigma_{xx})$$
  $(b_{[100]}\sigma_{yz})$  0  
 $F_{I-II} = Gxt = 0$  0 1

$$F_{I-II} = [ .648 1.54 0 ] N/m$$

<u>Screw</u>: (both parallel and antiparallel:  $b_{[001]}$  and  $b_{[001]} = b_{screw} = 1/2a_0 = 1.45\text{Å}$ )

$$G = \sigma_{ij(1)} = b_{(II)} = 0 \qquad 0 \qquad \sigma_{XZ} \qquad 0$$

$$0 \qquad 0 \qquad \sigma_{YZ} \quad \bullet \qquad 0$$

$$\sigma_{ZX} \quad \sigma_{ZY} \quad 0 \qquad b_{[001]}$$

Screw ctd.

Since stacking fault energy is equivalent to the forces between two dislocations, one can use the above information to approximate the APB energy of this fault.

F/unit length = N/m and stacking fault energy =  $\gamma$  = energy/ unit area = F/unit length

Combining Edge and Screw forces using the principle of superposition, yields the following results:

Parallel Burgers vectors:

$$F_{I-II} = [.398, 1.357, 0] \text{ N/m}$$

Antiparallel Burgers vectors:

$$F_{I-II} = [.898, 1.723, 0] \text{ N/m}$$

Adding the values vectorally (in order to equate to APB energy) yields:

Parallel Burgers vectors:  $\gamma = 141 \text{mJ/m}^2$ 

Antiparallel Burgers vectors:  $\gamma = 194 \text{mJ/m}^2$ 

#### REFERENCES

- 1. J.D. Whittenberger, "Intermetallics as Alternative Materials", NASA TM 83006, NASA-Lewis Research Center, Cleveland, OH, 1982, p.163
- 2. Kubaschewski, Ortrud, <u>Iron-Binary Phase Diagrams</u>, Germany: Springer Verlag Berlin/Heidelberg., 1982.
- 3. M.A. Meyers and K.K. Chawla, <u>Mechanical Metallurgy</u>, New Jersey: Prentice Hall, Inc., 1984.
- 4. R.Darolina, "NiAl Alloys For High-Temperature Structural Applications", JOM, Vol. 43 No. 3 (1991).
- 5. S.C. Tonn, Master's Thesis, Michigan State University, (1993).
- 6. C.L. Fu and M.H. Yoo, Mat. Res. Symp. Proc., Vol. 213 (1991) 667-673.
- 7. M.R. Harmouche and A. Wolfenden, Modulus Measurements in Ordered Co-Al, Fe-Al and Ni-Al Alloys, Journal of Testing and Evaluation. 13 (1985) 424-428.
- 8. T. Godecke and W. Koster, Z. Metallkude., 77 (#162) (1986) 408.
- 9. J.L. Everhart, Engineering Properties of Nickel and Nickel Alloys, New York: Plenum Press 1983.
- 10. J. Rieu and C. Goux, Mem. Sci. Rev. Met., 66 (1969) 869.
- 11. J.P. Riviere and J. Grilhe, Acta Met., **20** (1972) 1275.
- 12. D. Paris, P. Lesbats and J. Levy, Scripta Met., 9 (1975) 1373.
- 13. D. Paris and P. Lesbats, J. Nucl. Mater., 69 (1978) 628-632.
- 14. K.M. Ralls, T.M. Courtney and J. Wulff, "Introduction to Materials Science and Engineering", J. Wiley and Sons, New York (1976) 189.
- 15. K. Ho and R.A. Dodd, Scripta Met., 12 (1978) 1055.
- 16. D. Weber, M. Muertin, D. Paris, A. Fordeux and P. Lesbats, J. Phys. C7,37 (1977) 332.
- 17. M.A. Crimp, K. Vedula and D.J. Gaydosh, Proc. MRS, 81 (1987) 499.
- 18. M.A. Crimp and K.M. Vedula, Mat. Sci. and Eng., A165 (1993) 29.
- 19. M.A. Crimp and K. Vedula, Phil. Mag. A, **63** (1991) 559.

- 20. W.D. Nix, NASA N83 11302 D20, NASA-Lewis Research Center, (1982) 183.
- 21. J.D. Whittenberger and R.V. Krishnan, J. Mat. Sci., 19 (1984) 509-517.
- 22. M. Yamaguchi, Mechanical Properties of bcc Metals, M. Meshil ed., AIME, 1981, pp. 31-40.
- 23. V. Vitek, Proc. Roy. Soc. A352 (1976) 109.
- 24. S. Takeuchi, Phil. Mag. A, 41 (1980) 541-553.
- 25. M.A. Crimp, Ph.D. Dissertation, Case Western Reserve Univ., (1987).
- 26. T. Yamagata and H. Yoshida, Mat. Sci. and Eng., 12 (1973) 95.
- 27. T. Yamagata, Trans. Japan Inst. Metals, 18 (1977) 715.
- 28. Y. Umakoshi and M. Yamaguchi, Phil. Mag. A, 41 (1980) 573-588.
- 29. Y. Umakoshi and M. Yamaguchi, Phil. Mag. A, 44 (1981) 711-715.
- 30. M.G. Mendiratta, H.M. Kim, and H.A. Lipsitt, Met Trans. A., 15A (1984) 395.
- 31. A. Ball and R.E. Smallman, Acta Met., 14 (1966) 1517.
- 32. C.H. Lloyd and M.H. Loretto, Phys. Stat. Sol., 39 (1970) 163.
- 33. R.J. Wasilewski, S.R. Butler and J.E. Hanlon, Trans. AIME 239 (1967) 1357.
- 34. J. Bevk, R.A. Dodd and P.R. Strutt, Met Trans., 4 (1973) 159.
- 35. H.L. Fraser, R.E. Smallman and M.H. Loretto, Phil. Mag., 28 (1973) 651.
- 36. J.T. Kim and R. Gibala, MRS Proceedings vol. 213, L.A. Johnson, D.P.Pope and J.O. Steigler eds. 231 (1991) 261.
- 37. M.H. Loretto and R.J. Wasilewski, Phil Mag., 23 (1971) 1311.
- 38. R.G. Campany, M.H. Loretto and R.E. Smallman, J. Microscopy, 98 (1967) 174.
- 39. P. Veyssiere and R. Noebe, Phil. Mag. A., 65 (1992) 1.
- 40. R.D. Field, D.F. Lahrman and R. Darolia, Acta Met. et. Mat, 39 (1991) 2951.
- 41. Y.Q. Sun and G. Taylor, Proc. 3rd Japan Int. SAMPE Sym. on Intermetallic Compounds for high temperature Sturctural Applications, M. Yamaguchi and Fuckutomi eds., (1993) 1230.

- 42. C.C. Law and M.J. Blackburn, Final Technical Report AFWAL-TR-87-4102 (1987).
- D.B. Miracle, S. Russell and C.C. Law, MRS Proceedings vol. 288, I. Baker R. Darolia, J.D. Whittenberger and M.H. Yoo eds., 288 (1993) 1197.
- 44. D.L. Yaney and W.D. Nix, J. Mat. Sci., 21 (1986) 2083.
- 45. D.L. Yaney and W.D. Nix, J. Mat. Sci., 23 (1988) 3088.
- 46. Y. Zhang and M.A. Crimp, Unpublished Research.
- 47. D.S. Sharrott, Senoir Thesis, Michigan State University, (1992).
- 48. G, Sainfort. P. Mouturat, Mme. P. Pepin, J. Petit, G. Cabane and M. Salesse, Mem. Sc. Rev. Met., 40 (1963) 125.
- 49. K.M. Chang, Met. Trans. A., 21A (1990) 3027.
- 50. C.T. Liu, E.H. Lee, and C.G. McKamey, Scripta Met., 23, (1989) 875.
- 51. C.T. Liu and E.P. George, Scripta. Met., 24 (1990) 1285-1290.
- 52. D.J. Gaydosh, S.L. Draper and M.V. Nathal, Met. Trans. A., 20A (1988) 1701.
- 53. J.H. Westbrook, J. Electrochem. Soc., 103 (1956) 54.
- 54. P. Nagpal and I. Baker, Met. Trans. A., 21A (1990) 2281.
- 55. D.J. Gaydosh, M.V. Nathal, Scripta. Met., 24 (1990) 1281.
- 56. R.J. Lynch and L.A. Heldt, TMS proceedings, Processing, properties and Applications of Iron Aluminides., (1994).
- 57. Y.A. Chang, L.M. Pike, C.T. Liu A.R. Bilbrey and D.S. Stone, Intermetallics, 1, (1993) 107.
- 58. N.S. Stollof and R.G. Davies, Acta Met., 12 (1964) 473.
- H. Kimura and R. Maddin, <u>Ouench Hardening in Metals</u>, North Holland Publishing Co., Amsterdam, (1971) p.47.
- 60. N. Jungua, J.C. Desover and P. Moine, Phys. Stat. Sol. (a), 18 (1973) 387.
- 61. A. Forduex and P. Lesbats, Phil. Mag. A, 45 (1982) 395.
- 62. N. Jungua, J.C. Desoyer and J. Grilhe, Acta Met., 30 (1982) 395.
- 63. C. Vailhe and D. Farkas, Private Communication.

- 64. P. Stadleman, Ultramicroscopy, 21 (1987) 131.
- A.K. Head, P. Humble, L.M. Clarebrough, A.J. Morton and C.T. Forwood, Defects in Crystalline Solids vol. 7, S. Amelinckx, R. Gevers and J. Nihoul eds., Norh-Holland (1973).
- 66. M.J. Mills and D.B. Miracle, Acta Met. Mater., 41 (1993) 85.
- 67. R.C. Crawford and I.L.F. Ray, Phil. Mag., 35 (1977) 559.

